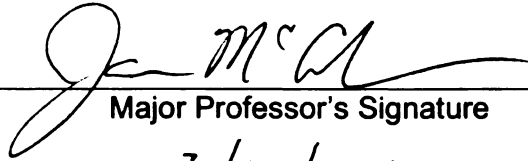This is to certify that the
dissertation entitled

ULTRAFAST DYNAMICS ASSOCIATED WITH TRANSITION
METAL BASED SENSITIZERS FOR TITANIUM DIOXIDE
BASED SOLAR CELLS

presented by

Amanda Lea Smeigh

has been accepted towards fulfillment
of the requirements for the

__Doctoral__   degree in   _____Chemistry_____

_____
Major Professor's Signature

3/13/2007
_____
Date

PLACE IN RETURN BOX to remove this checkout from your record.
TO AVOID FINES return on or before date due.
MAY BE RECALLED with earlier due date if requested.

DATE DUE	DATE DUE	DATE DUE

6/07 p:/CIRC/DateDue.indd-p.1

ULTRAFAST DYANMICS ASSOCIATED WITH TRANSITION METAL-BASED
SENSITIZERS FOR TITANIUM DIOXIDE BASED SOLAR CELLS

By

Amanda Lea Smeigh

A DISSERTATION

Submitted to
Michigan State University
in partial fulfillment of the requirements
for the degree of

DOCTOR OF PHILOSOPHY

Department of Chemistry

2007

ABSTRACT

ULTRAFAST DYANMICS ASSOCIATED WITH TRANSITION METAL-BASED SENSITIZERS FOR TITANIUM DIOXIED BASED SOLAR CELLS

By

Amanda Lea Smeigh

The importance of alternative energy sources in today's energy economy is undeniable. Currently, few consumers utilize alternative fuels in their everyday lives due to the large initial cost associated with installing the needed equipment. The research presented in this dissertation concerns a novel TiO_2-based solar cell, which has the potential to replace the expensive Si-based material currently used in commercially available solar cells. While the research presented here does not present a solution to the high cost of solar cell technology it does cover some important areas of research that are essential to furthering the technology needed to make these TiO_2-based solar cells commercially viable.

Details concerning the basic mechanism of the cell and the limitations of the current configuration are presented. A brief discussion on the electrolyte dependent injection rate of N3 bound to TiO_2 is presented, where we find that injection rates for N3 bound to TiO_2 is highly dependent on the concentration and identity of small ions in the supporting electrolyte. We show that it is essential to use salts that contain a redox active species to best model the functional cell during optical measurements. Subsequent discussions focus on fundamental studies of the intrinsic excited state dynamics of a series of iron(II) complexes.

The ultrafast evolution of the excited state manifold in iron(II) polypyridyl

complexes consists of deactivation of the charge transfer manifold in less then 100 fs and complete thermalizaiton of the long-lived, metal centered, ligand field excited state in under 50 ps. Generalization of these ultrafast excited state lifetimes observed in a series of iron(II) complexes provides a foundation for beginning to understand the dynamics associated with the intramolecular relaxation pathways of iron(II) complexes. Due to the inherently short lived charge transfer state present in iron(II) polypyridyl complexes, few iron(II)-based sensitizer have been used in TiO_2-based solar cells; however, establishing a better understanding of the charge transfer excited state's relaxation pathway will enable the identification of the molecular characteristics needed to potentially engineer an iron(II) complex that has a longer lived charge transfer state. In addition, the work done here provides a spectroscopic protocol for the characterization of new iron(II) complexes.

Dedicated to Nora Vandergriff and Helen Massengale, two women ahead of their time.

ACKNOWLEDGEMENTS

who knew that ordering lamps and laser optics could be that much trouble or that much fun? Thank you all. And last but not least on my list of support-ers are Lisa, Brenda, and Janet. Lisa, thank you for letting me bend your ear. Miss Janet, I will miss our encounters in the elevators, who will help you with all the mischief you need to get up to before you retire? I am always an email away, and when I make it back into town I will make sure I find you. Brenda, what can I say? My graduate school experience would not have been the same if I hadn't been so prone to breaking office equipment. Who knew you needed to turn the copier on to use it? And if you ever need some potato chips let me know I am sure my mom can send some more. Thank you for being real and being honest, I will miss you.

I would also like to acknowledged the McCusker Group, there are so many of you now I don't have room to give you all your proper due, so here is a cover all, thank you for all the trips to the Pub, to Reno's and to one of you Spiral. You will be missed, and remember I am only an email away. A few people do deserve individual recognition; Allison Brown, Jeff Bodwin, Laura Picraux, Jeremy Monat and Eric Juban.

Two vital people that need to be acknowledged are Eric Juan and Allison Brown. Allison, you have learned so much in such a short time and I have total confidence that you will have a productive spectroscopic experience! Aside from being an angel and taking over this project you became a dear friend. There are few people I can spend hours with at work and actually want to see them when the day is done and you are one of them. I am only an email or a SKYPE away. Believe in yourself because I believe in you. Eric Juban, who graduated from the group in 2006, was my mentor and friend for the past 5 years. We made it through burned crystals, exploded lamps, 5 degree temperature swings, and 5 Michigan winters together. His unique skill in the laser lab and his incredible intellect are matched only by his compassion and joy of life (or at least LSU football). Eric taught me so much more than how to tweak, or rebuild for that matter, our laser system he taught me that there needs to be a balance between work and life, it was an odd method of teaching but I get the message.

Other strong McCusker group influences are Jeff Bodwin, Laura Picraux, and Niels Damrauer. Jeff Bodwin was a post-doc in the group when I joined and he has been a continual source of support and a release valve when things got stressful around the lab. I couldn't ask for a better post-doc. Laura Picraux was a "tough love" kind of student. She expected as much out of you as she did out of herself and for that I am grateful. Niels is the "founding father" of the McCusker ultrafast technique and I am lucky to have come to know him personally. He has always been willing to assist in anyway possible and it has been a pleasure getting to know him.

I need to acknowledge our collaborators; the research groups of Nate Lewis and Harry Gray at Cal Tech including Libby Mayo and Jordan Katz for the TiO_2 and associated research, Munira Khaili and Henry Chong at Lawrence Berkeley Livermore National Lab and the Advanced Light Source for their work on the X-ray absorption publication, the Mathies group at UC Berkeley for their efforts with ultrafast Raman specifically Sangwoon Yoon and Mark Creelman, the Miller research group at the University of Toronto for their efforts on ultrafast X-ray spectroscopy on one of my iron complexes.

Down to the essential acknowledgements. For all those people that helped me make it through, that hugged when I needed a hug, drove when I needed a designated driver and laughed when I needed a smile you have my eternal gratitude. Dr. Elizabeth (Carson) Golovich and her James, Dr. Emily McKimmy and Matt, Andrea Carson, Karen and David Taylor, Julia Cox, Liz Farina, Ela and the girls in the TTH Intermediate Ballet class at LCC, Jane and "Little Butchie" Williams, Virginia Stanley, Craig Krenzel, Kade Roberts, Allison Brown, Dan Dupuis, and Marc West. I am blessed to have all of you in my life you all deserve a medal for helping me through this. Thank you all, this would not have been the same with out you.

For this last group I can only say thank you because there are no word to express my gratitude for how much you have all made possible. I love you all. Dad, I literally wouldn't be here if it wasn't for you. Thank you for being there for me these past five

years. Nancy thank you for everything that you have done, you don't know the half of it. Mom thank you for giving me this opportunity, forcing me to go to college was one of the best things that happened to me. Toby-Seth you will always be my little brother no matter have much bigger than me you are. Thank you for listening when I really needed to talk. Brannigan you are/were/and always will be my man. Aberdeen, Abby, you have been a wonderful pain and the best friend a girl could have. Steven, thank you for giving me no other option, your support and encouragement is heaven sent.

.

TABLE OF CONTENTS

LIST OF FIGURES

Images in this thesis/dissertation are presented in color.

LIST OF TABLES

Chapter 1. Introduction to the Grätzel Cell: A TiO$_2$-based Dye Sensitized Solar Cell.

1.1 Introduction

Michael Grätzel's report of efficient generation of a photocurrent with a ruthenium dye bound to TiO$_2$ in 1985 infused interest in research which began focusing on the area of dye sensitized solar cells (DSSCs).[1,2] Since this seminal report the area of DSSC research has increased dramatically. More than 20 years later, researchers are still exploring the unique design of Grätzel's original dye sensitized solar cell.

A DSSC is composed of a wide-band-gap semiconductor material, a sensitizer, supporting electrolyte, and a redox active species. All of these components work in concert to enable to efficient production of electricity from sunlight. Grätzel's choice of semiconductor material is titanium dioxide (TiO$_2$)[3], specifically nanocrystalline anatase TiO$_2$. However, other wide band-gap materials such as ZnO, SnO$_2$, In$_2$O$_3$ and Nb$_2$O$_5$ have also been studied.[4-9] Benefits associated with using nanocrystalline TiO$_2$ films are well established.[3,10] Nanocrystalline films provide a significant enhancement of sensitizer concentration in comparison to single crystal TiO$_2$ films, due to the increase in surface area associated with the small particles. Additionally, the films are typically deposited on F-doped SnO$_2$ conductive glass electrodes to provide mechanical stability and maintain the optically transparent nature of the nanocrystalline TiO$_2$.[3] The transparent nature of these nanocrystalline films increases the likely hood the sensitizer will absorb a photon and thus be able to produce a photocurrent.

Another significant aspect of TiO$_2$-based solar cells is that the cost of TiO$_2$, in comparison to current solar cell materials, is low. Titanium dioxide is an abundant and benign material that is used in many commercial products such as bread, doughnuts, paint, and plastics. Comparatively, the cost of manufacturing TiO$_2$ is drastically less than that of silicon-based materials used in the current commercially available solar cells. Ultra

1

pure silicon is essential to the efficient conversion of sunlight to electricity in the current materials, this purity comes as a high cost due to the byproducts generated in the purification process. While other factors do influence the consumer seldom is price not an issue and the lower cost of material for TiO_2 based cells then that for silicon based cells might provide the financial push for some consumers to invest in solar electricity.

In the case of the TiO_2-based cells, the sensitizer acts as a mid-band-gap dopant with its ground state oriented energetically between the valence and conduction bands and one or more of its excited states above the conduction band edge as shown in Figure 1-1A. An ideal sensitizer should have optical transitions that extend from the visible region to the red and infrared regions of the electromagnetic spectrum. Absorptions that extend into these regions will provide the best overlap between the solar spectrum and the sensitizer, since the majority of the radiation that reaches earth consists of visible and near infrared radiation.[10] By matching the absorptions of the sensitizer to the solar spectrum a large percent of the solar energy that reached earth can be harnessed and converted to electricity. Additionally, the type of optical transition present in the absorption spectrum is significant. Due to the nature of the sensitized cell the sensitizer must have an orientation that enables it to inject and electron into the TiO_2. In an ideal case, absorption of a photon will cause the sensitizer to produce an excited complex that localizes an electron at a position on the sensitizer, which can facilitate electron injection into the conduction band of the TiO_2; one such example is the localization of an electron on the ligand of the sensitizer. In the case of the transition metal complexes addressed in the following studies, a metal-to-ligand charge transfer (MLCT) transition would result in this preferred ligand localized configuration.

Various types of sensitizers have been employed in attempts to fully optimize TiO_2-based DSSCs. Sensitizers ranging from organic[11-20] to inorganic[1-3, 5, 10, 21-43] complexes have been studied and the endeavor to identify of the best sensitizer encourages further synthesis and modification of potential sensitizers. A common approach used in designing an ideal sensitizer is through molecular engineering and transition metal complexes are well-suited

candidates for this molecular engineering approach. The benefits of engineering a sensitizer is that the scientific community is able to manipulate the absorption spectrum of a complex while maintaining the placement of the electron in the excited complex.

Energetics and excited-state behavior of the sensitizer play a significant role in the feasibility of the cell's operation.[10] If the excited state of the sensitizer does not lie above the conduction band edge of the TiO_2 then no electron injection can occur and thus no photocurrent is present. Moreover, is the excited state does not localized the electron at a positions that is favorable for electron injection the probability of the production of a photocurrent is significantly reduced. Provided that a sensitizer has an excited state that resides above the conduction band and that the configuration of that excited state is such that the electron in the excited sensitizer is positioned to inject an electron into the conduction band of TiO_2 there is still the concern of the electronic coupling of the sensitizer to the semiconductor. Electronic coupling is the mechanism of interaction of the sensitizer with the semiconductor, which is often manifest as a bond between the two components. The type of bond between the sensitizer and TiO_2 influences the rate of electron injection. A chemical bond (chemisorption) is more strongly coupled than a simple physical interaction (physisorption). Chemically linking the sensitizer to the semiconductor provides a pathway for electronic communication between the sensitizer and semiconductor and enhances electron injection from the sensitizer to the TiO_2. The chemical bond formed between the sensitizer and the semiconductor facilitates the transfer of an electron to the TiO_2, thus enabling efficient electron injection. Equally important is the distance between the sensitizers and the TiO_2. This distance directly impacts the electronic coupling between the two, where the longer the distance the slower the injection process from the sensitizer to the TiO_2.[44-46] In DSSCs, the sensitizer, most often a ruthenium polypyridyl complex, is bound to the semiconductor surface through linking groups, typically carboxylic acid or phosphonate moieties, which form chemical bonds with the TiO_2.[10, 27, 47, 48] In addition to the strong electronic coupling between the sensitizer and the TiO_2 via the chemical binding

3

of the sensitizer to the surface the nanocrystalline nature of the semiconductor increases the amount of sensitizer that can be bound to the TiO_2 film. The increased surface area of nanocrystalline materials provides more sites to anchor the sensitizer, thus increasing the concentration of sensitizers on the film and ultimately increasing the number of electrons present in the TiO_2. This increased electron density in the TiO_2 ultimately leads to a larger photocurrent attainable with the cells.

Completion of the cell is achieved by covering the sensitized film with a supporting electrolyte solution that contains a redox active couple. Covering the sensitized film with the electrolyte solution ensured that the sensitizer is in contact with both the TiO_2 and the electrolyte, allowing for a complete circuit. The composition of the electrolyte and the redox species both impact the conduction band edge of the semiconductor[49, 50] and the energetics of the sensitizer[51-53]. Electrolytes used in DSSCs are usually prepared with non-aqueous solvents and contain high concentrations of small cations. The majority of the studies on DSSCs use Li^+ based salts as electrolytes when measuring overall efficiencies and recombination rates, due to the ability of Li^+ and other small positive cations to shift the flat band potential of TiO_2 to more positive potentials.[49] Shifting the conduction band edge of TiO_2 to more positive potentials is beneficial in that as the conduction band edge shifts more positive the driving force for electron injection from the sensitizer increases. This increase in driving force for electron injection biases the system to increase the injection yield thus increasing the photocurrent obtained from the cell. Shifting the conduction band more positive also enables excited states of the sensitizer that have energy slightly below the standard band edge to now reside above the band edge and thus participate in electron injection.

Figure 1-1A shows a schematic of a typical dye sensitized solar cell and Figure 1B shows a cartoon of the interaction of the electrolyte with the sensitized TiO_2. Once the cell is exposed to light, the sensitizer absorbs a photon and is promoted to an excited state. From the excited state the sensitizer injects an electron into the conduction band
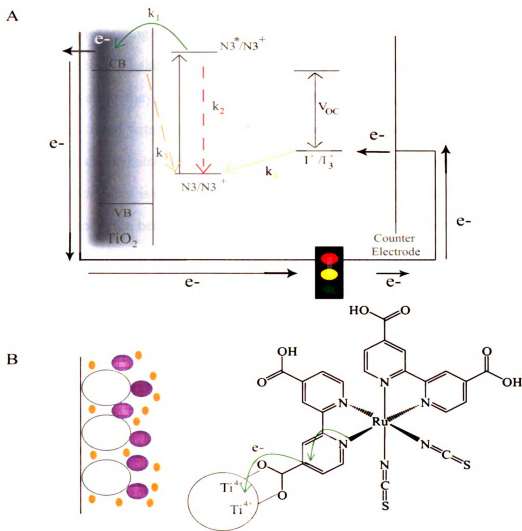
Figure 1-1. Schematic of a Dye Sensitized Solar Cell (DSSC)
A) A schematic of the basic configuration of a DSSC. Rates of interest are indicated by colored arrows and corresponding k_ns. After excitation (black arrow) the sensitizer injects an electron k_1 (green arrow). That electron does electrical work in a circuit and a small residual current activates the redox couple. The redox couple reduces the oxidized sensitizer k (arrow), enabling the sensitizer to be excited again and inject another electron. Rates k_2 and k_3 correspond to deactivation of the excited state prior to injection and back electron transfer of the injected electron to the oxidized dye respectively. In an ideal cell, rates k_2 and k_3 are sufficiently small, to bias the system to generate a large photocurrent. B) The left cartoon illustrates the interaction of the redox couple with the bound sensitizer. One binding mode for sensitizers is shown on the right with N3 binding to TiO_2 through the carboxylate moiety in a bidentate fashion.

of the TiO_2, where along with other electrons it can be harnessed to do electrical work; classifying these DSSCs as photoelectric cells. To complete the circuit a small residual current is used to activate the redox couple, typically I^-/I_3^-, in the electrolyte solution. The

activated redox couple reduces the oxidized sensitizer, enabling the sensitizer to return its initial oxidation state. Regeneration of the sensitizer enables the process to occur many times over, categorizing this type of cell as regenerative.[2]

The delicate balance between all the above components enables these DSSCs to function as well as they do and this balance is dependent on several key processes and the rates associated with each process. Of primary importance are the rates of electron injection and excited state deactivation; k_1 and k_2 respectively as shown in Figure 1-1A. The excited state that is energetically able to inject the electron into the conduction band of the semiconductor, being that it is high enough in energy to reside above the conduction band edge, must persist long enough to inject the electron. Intramolecular relaxation (k_2) of the initially formed excited state to a lower energy state that does not reside above the conduction band can reduce the overall electron injection yield from the sensitizers and thus reduce the photocurrent production. In the case of the most commonly used ruthenium(II)-based sensitizers, the low energy long-lived excited states are: 1) high enough in energy to exist above the conduction band and 2) retain an excited state configuration that permits the long-lived state to inject an electron without the complication of deactivation of the state on the injection timescale. It was initially thought that sensitizers must possess charge transfer long-lived excited states to be considered viable for incorporation into DSSCs. And due to the extensive characterization of the long-lived excited state of second and third row transition metal complexes, specifically ruthenium(II) and osmium(II),[54-60] the majority of sensitizers incorporated into TiO_2-based DSSCs have been ruthenium(II)-based sensitizers. A ruthenium(II) complex known as N3, where N3 is bis(2,2'-bipyridyl-4,4'-dicaboxylate)bis(thiocyanato)ruthenium(II) has become the standard complex to use when attempting to understand the dynamics associated with TiO_2-based DSSCs. Reports of the impact manipulating various aspect of the DSSC has on dynamics associated with the sensitizer is dominated by N3 sensitized films.[34] If an appropriate sensitizer is chosen, N3 for example, then intramolecular relaxation, k_2, is no longer a concern due to its long-lived excited state

that resides above the conduction band edge. In most second and third row transition metal complexes, as is the case in N3, the long-lived excited state has a relatively long lifetime providing ample opportunity for the long-lived excited state to inject an electron, which is the reason that the majority of inorganic sensitizers that have been found to be successful sensitizers are based on second and third row transition metals.

A second set of competing rates that readily impacts the efficiency of a DSSC are the rates of back electron transfer from the TiO_2 to the sensitizer and regeneration of the sensitizer, k_3 and k_4 respectively also shown in Figure 1-1A. If the injected electron recombines with the oxidized sensitizer, no net current can flow rendering the cell useless. Therefore, the redox active species must regenerate the sensitizer faster than the injected electron can recombine with the oxidized sensitizer to enable the production of a photocurrent. This means that k_4 must be larger than k_3. Changing the redox species or the sensitizer will change the rates of each of the respective processes by changing the driving force for the recombination and regeneration processes. It has been shown that moving the ground state of the sensitizer more negative increases the recombination rate, k_3, and decreases the regeneration rate, k_4.[3x] The way the change in energy of the ground state of the sensitizer affect the change in the rate implies that recombination occurs in the Marcus inverted region, where a smaller driving force increases the rate. And manipulation of the energy of the redox couple with respect to the ground state of the sensitizer results in the regeneration process occurring in the Marcus normal region, where a smaller driving force decreases the rate. Variation of both the ground state of the sensitizer and the identity of the redox species can impact the overall efficiency of the cell, by changing the efficiency of regeneration and rate of recombination. For example if the sensitizer is exchanged from N3 to another ruthenium(II) complex with a higher energy, more negative energetically, ground state the rate of recombination will increase and the rate of regeneration will decrease, which would lead to low photocurrents due to and increase in the rate of recombination of the electron in the conduction band with the oxidized sensitizer. A similar scenario can

be presented for exchanging the redox couple, where substituting a redox couple with a more positive potential will lead to slower regeneration and thus increase the probability of recombination reducing the photocurrent attained from the cell.

The best way to gauge the successful balancing of the injection, recombination and regeneration is with the overall efficiency of the cell's configuration. Overall efficiencies for DSSCs are calculated according to Equation 1.

$$\eta_{global} = (i_{ph} \, V_{oc} \, f) \, I_s \qquad\qquad (1)$$

The open circuit voltage (V_{oc}) and the integrated photocurrent density (i_{ph}) are obtained from a potentiometric measurement with optical excitation of the cell from a broadband radiation source that mimics the intensity and spectral distribution of sunlight impinging the earth, most often with a 1.5 "air mass" filter. The open circuit voltage in V (V_{oc}) is the maximum energy that can be achieved with the cell, which is directly dependent on the semiconductor and the redox couple and is best thought of as the photovoltage obtained with the complete cell. Shifting the conduction band edge more negative or the potential of the redox couple more positive will increase the output energy of the cell; however, the injection rate and regeneration rate are also affected by these shifts and thus shifting the conduction band edge or the energy of redox couple can limit the amount of photocurrent obtained from the cell. The integrated photocurrent density in A cm^{-2} (i_{ph}) is the maximum number of electrons that can be used in the circuit. The amplitude of the photocurrent is dependent on several factors. The first is the number of electrons injected into the TiO_2, which can be considered as the quantum yield for electron injection. A quantum yield for electron injection measures the efficiency of the excited state of the sensitizer in injecting and electron into the TiO_2. Depending on how many sensitizers absorb a photon and populate an appropriate excited state and how efficiently that excited state transfers an electron into the conduction band of the semiconductor, the quantum yield for injection, the photocurrent can vary significantly. If the quantum yield for injection is only 20%, the photocurrent is already limited as to how many electrons will be present in the TiO_2

8

and available for current flow. Secondly, assuming that all the excited sensitizers inject

an electron, the collection efficiency of the cell can further quench the photocurrent. If

an injected electron recombines with the oxidized dye or is lost to other processes, such

as a reaction with the redox couple, the possible photocurrent is subsequently reduced.

Plotting the current-voltage curve enables the determination of i_{ph} and V_{oc} which provides

a gauge of possible power output from the cell since the product of i_{ph} and V_{oc} yield the

output power. The power obtained from the product of the i_{ph} and V_{oc} must be scaled by

a fill factor to provide an accurate value of overall efficiency. This fill factor (ff), ranging

from 0 to 1, is the area that the measured trace fills compared to an ideal trace as shown

in Figure 1-2 with the black line representing an ideal case and the blue line representing
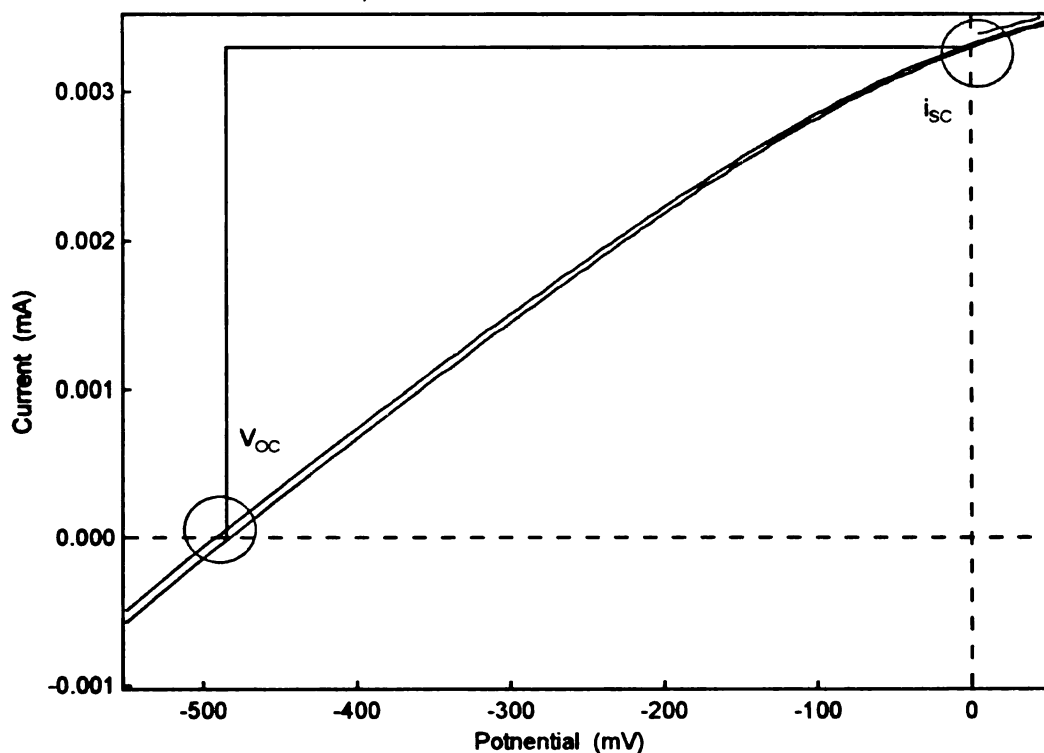
Figure 1-2. An Example of a Current-Voltage Plot used to Determine Overall Efficiency
A current-voltage curve for N3 bound to TiO_2 in the presence of 0.5 M LiI 50 mM CH_3CO_2H (blue trace). The black line represents an ideal situation for this configuration. By finding the ratio of areas of the experimental (blue) to the ideal (black) we can calculate the fill-factor (ff). Open circuit voltage (V_{oc}) is determined to be where the trace crosses 0 on the x-axis (-485 mV) and corresponds to the maximum energy of the electrons in the system. Short circuit currents (i_{sc}) are determined to be the current measured when no voltage is applied.

9

the real trace.[2, 10] The incident power (I_s) is dependent on the excitation source employed and is approximately 1000 W/cm² for most experiments, but does vary between research groups. Most often η_{global} is reported as a percent from 0 % to 100 % and at present the best efficiency reported is 11.04 %.[34] The accepted break even point for TiO_2-based DSSCs to be commercially competitive with the current Si-base technology, which is ~25 % efficient[1], is 15 %.[3]

Continued efforts are being made to further improve the overall efficiency of DSSCs; however, progress is slow. Achieving the appropriate energetics of the sensitizer and the redox species with respect to the conduction band of the semiconductor is difficult and slight offsets can result in poor efficiencies. The complication of direct reactions of electrons in the conduction band of TiO_2 with the redox couple and the possibility of back electron transfer detrimentally impacts the photocurrents obtained with the cells. The intrigue of the intricate balance between injection, recombination, and regeneration has been driving research in the DSSC field for these past twenty years since Grätzel's initial report.[1, 34] With the overall efficiency steady at ~11 % and the V_{OC} at ~0.8 eV, innovative ideas are needed to push these values to the ~15 % overall efficiency and maximize the V_{OC} in order to achieve a commercially competitive cell.

Characterization of the dynamics associated with the injection, recombination and regeneration of DSSCs has become an area of increased interest. Several spectroscopic techniques dominate the field of sensitizer characterization, mainly optically oriented techniques due to the optically transparent nature of the DSSC, which lends itself to a variety of optical measurements. Both visible[31, 38, 62-65] and infrared[7-9, 23, 66-68] ultrafast transient absorption studies have been able to provide insight into the injection process of the sensitizer with various semiconductors. The injection timescale has been reported to be as fast as 50 fs and extends to as long as 100 ps.[22, 23, 38, 63, 64, 66, 69] The majority of these studies have been done on samples exposed to air[6, 22-24, 38, 66] or immersed in an electrolyte composed of small cations.[6, 31] Seminal work by Willig and coworkers in 1997 report that

10

injection from the initially excited [1]MLCT state of a ruthenium(II)-based sensitizer does occur.[70] Prior to this report, it was speculated that the [1]MLCT state was also involved in the injection process; however, due to the charge transfer nature of the long-lived [3]MLCT state it was assumed that the majority of the injection came from the latter. Additionally, the lifetime of the [1]MLCT state is ultrafast[58, 71] and thus rapidly deactivates to the long-lived [3]MLCT state without substantial relaxation in the [1]MLCT state indicating that the injection from the [1]MLCT state is coming from a vibrationally "hot" state. Since this initial report the notion of "hot injection" from a non-thermalized excited state has become widely accepted. In 1998, Ferrere and Gregg reported the observation of a photocurrent with an iron(II) chromophore[28], since the long-lived excited state of low-spin iron(II) complexes had been established previously to be ligand-field in nature and formed in less than 700 fs[72], injection from the long-lived state is not probable, indicating that "hot injection" is the only available path for injection with iron(II)-based sensitizers; however, the specific mechanism for ruthenium(II)-based sensitizers was still uncertain. In 1999, several groups reported the arrival of the electron in the conduction band by direct detection of the electron in the conduction band provided strong evidence that injection was occurring almost instantaneously and most likely from the [1]MLCT state.[23, 32] Further substantiation by Lewis and coworkers in 2002 was presented in the literature in terms of selectively exciting into the [1]MLCT and [3]MLCT states. Excitation into the [1]MLCT state produced an ultrafast component to the injection dynamics that disappeared when the excitation was tuned the [3]MLCT state.[38].

As seen above, a significant amount of research has focused on the sensitizer; however, it is important to note that the impact of electrolyte composition has also been covered in the literature. Different electrolytes and redox species have been studied in the hopes to elucidate a combination that produces a more efficient TiO_2-based DSSC. The typical redox species is I^-/I_3^- couple; however, due to the optically dense nature of the I^- /I_3^- couple many reports have focused on substituting other redox active species into the

cell.[2, 51, 53] To successfully replace the I^-/I_3^- couple a redox species must rapidly (<1 μs) reduce the oxidized sensitizer thus preventing back electron transfer from occurring[10]. To date, there have been no outstanding replacements identified for the optically opaque I^-/I_3^- couple. This is most likely due to the fact that the reduction potential of I_3^- is positive enough to yield a relatively large V_{oc} and still maintain a driving force for regeneration that promotes efficient regeneration of the oxidized sensitizer. Most of the research concerning the electrolyte composition is reported in terms of overall efficiency and recombination/ regeneration rates[21, 32, 39, 42, 45, 50, 51, 68, 73-78] with few reports venturing to investigate the impact the electrolyte composition has on the injection dynamics of a sensitizers bound to TiO_2. Studies on the excited state of ruthenium based sensitizers both in solution[9] and bound to TiO_2[50] have examined the impact of the presence and concentrations of small cations in the electrolyte. In 1999, Meyer and coworkers reported that there was a significant difference in the observed excited state kinetics of ruthenium(II) polypyridyl complexes when the cation of the electrolyte was changed from Li^+ to tetrabutrylammonium (TBA^+).[76] Later reports by Meyer and coworkers found that the presence of I^- quenches the excited state of several ruthenium(II) complexes,[52, 79, 80] which, in the case of ruthenium(II)-based sensitizers, will most likely inhibit the ability of the sensitizer to undergo injection into TiO_2 and thus decrease the efficiency of a cell.

On going research efforts by many dedicated groups may eventually achieve the desired 15 % efficient cell but not without the essential characterization of the many fundamental processes occurring in the cell. Establishing an understanding of the intrinsic properties of the sensitizer, and understanding the electrolyte impact the electrolyte has on injection dynamics of the sensitizer is essential to establishing an understanding of how to achieve the 15 % efficient cell. Efforts to understand and characterize the intrinsic dynamics of sensitizers and their ability to undergo electron transfer to a semiconductor is the focus of this work and will be discussed as indicated below.

1.2 Contents of Dissertation

The focus of the research contained in this thesis can be separated into two sections; ruthenium(II)-based sensitizers and iron(II)-based sensitizers. Currently, ruthenium(II)-based sensitizers are the most efficient and most thoroughly characterized sensitizers making them ideal to study the impact other variables have on the overall efficiency and injection dynamics of the sensitizers. Iron(II)-based systems lack the intense focus of the sensitizer community, largely due to the long-lived ligand field state that does not inject into TiO_2. While the small photocurrents associated with iron(II)-based sensitizers[27-30] cause many researchers to look elsewhere, the fact that injection can only come from the initially excited drastically simplifies the picture of injection and should not preclude iron(II) complexes from being considered as potential sensitizers.[26, 33]

The first section, Chapter 2, examines the impact electrolyte composition has on the injection dynamics associated with N3 bound to TiO_2. As mentioned above, the optical density of the I^-/I_3^- couple makes optical measurements in the visible region of the spectrum difficult. Most researchers substitute optically transparent perchlorate $(-ClO_4^-)$ salts for the optically opaque iodide salts $(-I^-)$; however, there has yet to be a report asserting the validity of this substitution. Correlating the observed injection dynamics in the presence of perchlorate salts with the overall efficiencies, which are measured in the presence of the iodide salts, does not provide the most accurate correlation. As part of an ongoing collaboration with the Lewis group at Cal Tech an interesting question arose. What was the source of a five-fold decrease in the overall efficiency of an N3 sensitized TiO_2-based DSSC when the supporting electrolyte was changed from LiI/I_2 to $TBAI/I_2$?[81] The results of the study illustrates the difference in the injection dynamics between the TBA^+ and Li^+ electrolytes as both iodide and perchlorate salts. In conjunction with determining the impact the cations had on the injection dynamics both $-I^-$ and $-ClO_4^-$ anions were also compared to determine if using $-ClO_4^-$ salts provides an accurate model for monitoring injection process in TiO_2 based solar cells.

In view of the highest routinely attainable V_{OC} of ~0.8 eV in TiO_2-based cells with ruthenium(II)-based sensitizers and the I^-/I_3^- redox couple, an effort to use other sensitizers coupled with other redox couples could prove beneficial to overcoming the barrier to increasing the overall efficiency of DSSCs. Using an iron(II)-based sensitizer could increase the V_{OC} by enabling the incorporation of redox couples with more positive potentials, due to the intrinsically faster rate of reactivity in first-row transition metals. The initial reports of iron(II)-based sensitizers incorporated into DSSCs indicates low photocurrent production.[28-30, 33] To better understand the reasons for this low current we systematically studied a series of iron(II) polypyridyl complexes. Chapters 3-5, deal with the intrinsic excited state dynamics of iron(II) complexes after [1]MLCT excitation and the impact those dynamics have on the feasibility of iron(II)-based sensitizer of being incorporated into DSSCs. Since iron(II) has such a large density of ligand-filed states below its initially excited state, deactivation from the initially excited state occurs rapidly, < 700 fs,[72] making injection from a vibrationally "hot" state the only feasible option for the generation of a photocurrent.

Chapter 3 is a continuation of previous work in our group which has shown that a model iron(II) complex has a [1]MLCT lifetime less than 100 fs.[82] Identification of the formation of the long-lived excited state and the nature of this excited state with various techniques provides insight into the intrinsic dynamics of this iron(II) complex and suggest that these ultrafast dynamics might be an integral part of the relaxation of all iron(II) polypyridyl complexes. Complete characterization of this unique complex provides a format for beginning to study the excited state dynamics of other iron(II) complexes.

Chapter 4 uses a 1980 paper, published by Sutin and coworkers, as a base for examining the excited state dynamics of a series of iron(II) complexes.[57] The 1980 report was only limited to reporting on the ground state recovery dynamics of the iron(II) complexes due to temporal restriction of the apparatus. With the significant developments in time-resolved transient absorption spectroscopy, we were able to extend their work into the first

14

100 fs after excitation. In this ultrafast regime we are able to provide a generalized picture of iron(II) photophysics from $\Delta t = 0$ to 1 ns, which will provide a fundamental understanding of the excited state dynamics associated with iron(II) polypyridyl complexes. Establishing a foundation in iron(II) polypyridyl photophysics enables us to better understand the injection dynamics associated with iron(II) sensitized TiO_2 and provides a means to begin engineering iron(II) complexes.

Chapter 5 provides a summary of preliminary results on several iron(II) complexes that are suited for incorporation as sensitizers into TiO_2-based DSSCs. Characterization of the complexes in solution and bound to a semiconductor are presented in an attempt to provide an initial look into the dynamics associated with electron injection from iron(II)-based sensitizers.

Concluding comments and future directions are included as a sixth chapter. The implications the previous chapters have on the issues associated with DSSCs are discussed and potential directions for the research are presented.

1.3 References

1.   Desilvestro, J.; Grätzel, M.; Kavan, L.; Moser, J.; Augustynski, J. *J. Am. Chem. Soc.* **1985**, *107*, 2988-2990.

2.   Vlachopoulos, N.; Liska, P.; Augustynski, J.; Grätzel, M. *J. Am. Chem. Soc.* **1988**, *110*, 1216-1220.

3.   O'Regan, B.; Grätzel, M. *Nature* **1991**, *353*, 737.

4.   Asbury, J. B.; Wang, Y.; Lian, T. *J. Phys. Chem. B* **1999**, *103*, 6643-6647.

5.   Iwai, S.; Hara, K.; Murata, S.; Katoh, R.; Sugihara, H.; Arakawa, H. *J. Chem. Phys.* **2000**, *113*, 3366.

6.   Ai, X.; Anderson, N. A.; Guo, J.; Lian, T. *J. Phys. Chem. B* **2005**, *109*, 7088-7094.

7.   Ai, X.; Guo, J.; Anderson, N. A.; Lian, T. *J. Phys. Chem. B* **2004**, *108*, 12795-12803.

8.   Anderson, N. A.; Ai, X.; Lian, T. *J. Phys. Chem. B* **2003**, *107*, 14414-14421.

9.   Guo, J.; Stockwell, D.; Ai, X.; She, C.; Anderson, N. A.; Lian, T. *J. Phys. Chem. B* **2006**, *110*, 5238-5244.

10. Kalyanasundaram, K.; Grätzel, M. *Coord. Chem. Rev.* **1998**, *77*, 347-414.

11. Martini, I.; Hodak, J. H.; Hartland, G. V. *J. Phys. Chem. B* **1998**, *102*, 607.

12. Tachibana, Y.; Haque, S.; Mercer, I. P.; Durrant, J. R.; Klug, D. R. *J. Phys. Chem. B* **2000**, *104*, 1198.

13. Tammell, S. A.; Moss, J. A.; Yang, J. C.; Nakhle, B. M.; Slate, C. A.; Odobel, F.; Sykora, M.; Erickson, B. W.; Meyer, T. J. *Inorg. Chem.* **1999**, *38*, 3665.

14. Lui, D.; Kamat, P. V.; Thomas, K. G.; Thomas, K. J.; Das, S.; George, M. V. *J. Chem. Phys.* **1997**.

15. Barazzouk, S.; Lee, H.; Hotchandani, S.; Kamat, P. V. *J. Phys. Chem. B* **2000**, *104*, 3616.

16. Ghosh, H. N.; Asbury, J. B.; Lian, T. *J. Phys. Chem. B* **1998**, *102*, 6482.

17. Hilgendorff, M.; Sundstrom, V. *J. Phys. Chem. B* **1998**, *102*, 10505.

18. Martini, I.; Hartland, G. V.; Kamat, P. V. *J. Phys. Chem. B* **1997**, *101*, 4826.

19. Burfeindt, B.; Hannappel, T.; Storck, W.; Willig, F. *J. Phys. Chem.* **1996**, *100*, 16463.

20. Boschloo, G. K.; Goossens, A. *J. Phys. Chem.* **1996**, *100*, 19489.

21. Alebbi, M.; Bignozzi, C. A.; Heimer, T. A.; Hasselmann, G. M.; Meyer, G. J. *J. Phys. Chem. B* **1998**, *102*, 7577-7581.

22. Asbury, J. B.; Anderson, N. A.; Hao, E.; Ai, X.; Lian, T. *J. Phys. Chem. B* **2003**, *107*, 7376-7386.

23. Asbury, J. B.; Ellingson, R. J.; Ghosh, H. N.; Ferrere, S.; Nozik, A. J.; Lian, T. *J. Phys. Chem. B* **1999**, *103*, 3110-3119.

24. Asbury, J. B.; Hao, E.; Wang, Y.; Ghosh, H. N.; Lian, T. *J. Phys. Chem. B* **2001**, *105*, 4545-4557.

25. Asbury, J. B.; Hao, E. C.; Wang, Y. Q.; Lian, T. *J. Phys. Chem. B* **2000**, *104*, 11957.

26. Asbury, J. B.; Wang, Y.-Q.; Hao, E.; Ghosh, H. N.; Lian, T. *Res. Chem. Inter.* **2001**, *27*, 393-406.

27. Ferrere, S. *Inorg. Chimi. Acta.* **2002**, *329*, 79-92.

28. Gregg, B.; Ferrere, S. *J. Am. Chem. Soc.* **1998**.

29. Yang, M.; Thompson, D. W.; Meyer, G. J. *Inorg. Chem.* **2000**, *39*, 3738-3739.

30. Yang, M.; Thompson, D. W.; Meyer, G. J. *Inorg. Chem.* **2002**, *41*, 1254-1262.

31. Bauer, C.; Boschloo, G.; Mukhtat, E.; Hagfeldt, A. *J. Phys. Chem. B* **2002**, *106*, 12693-12704.

32. Farzad, F.; Thompson, D. W.; Kelly, C. A.; Meyer, G. J. *J. Am. Chem. Soc.* **1999**, *121*, 5577-5578.

33. Ghosh, H. N.; Asbury, J. B.; Weng, Y. X.; Lian, T. *J. Phys. Chem. B* **1998**, *102*, 10208.

34. Grätzel, M. *Inorg. Chem.* **2005**, *44*, 6841-6851.

35. Hagfeldt, A.; Didriksson, B.; Palmqvist, T.; Lindstroem, H.; Soedergren, S.;

Rensmo. H. *Sol. Eng. Mat. Sol. Cells* **1994**, *31*, 481-8.

36.   Kelly. C. A.; Farzad. F.; Thompson. D. W.; Meyer. G. J. *Langmuir* **1999**, *15*, 731-737.

37.   Kuciauskas, D.; Freund. M. S.; Gray. H. B.; Winkler. J. R.; Lewis. N. S. *J. Phys. Chem. B* **2001**, *105*, 392.

38.   Kuciauskas. D.; Monat. J. E.; Villahermosa. R.; Gray. H. B.; Lewis, N. S.; McCusker, J. K. *J. Phys. Chem. B* **2002**, *106*, 9347-9358.

39.   Nazeeruddin. M. K.; Kay. A.; Rodicio. I.; Humphry-Baker, R.; Müller. E.; Liska. P.; Vlachopoulos. N.; Grätzel. M. *J. Am. Chem. Soc.* **1993**, *115*, 6382-6390.

40.   Nazeeruddin. M. K.; Pechy. P.; Grätzel. M. *Chem. Comm.* **1997**, 1705-1706.

41.   Nazeeruddin. M. K.; Pechy. P.; Renouard. T.; Zakeeruddin, S. M.; Humphry-Baker, R.; Comte. P.; Liska. P.; Cevey. L.; Costa, E.; Shklover, V.; Spiccia, L.; Deacon. G. B.; Bignozzi. C. A.; Grätzel. M. *J. Am. Chem. Soc.* **2001**, *123*, 1613-1624.

42.   Wang. Z.-S.; Yamaguchi. T.; Sugihara. H.; Arakawa. H. *Langmuir* **2005**, *21*, 4272-4276.

43.   Yang. M.; Thompson. D. W.; Meyer. G. J. *Inorg. Chem.* **2000**, *39*, 3738.

44.   Taratula. O.; Rochford. J.; Piotrowiak. P.; Galoppini. E.; Carlisle. R. A.; Meyer. G. J. *J. Phys. Chem. B* **2006**, *110*, 15734-15741.

45.   Wang. D.; Mendelsohn. R.; Galoppini. E.; Hoertz. P. G.; Carlisle. R. A.; Meyer. G. J. *J. Phys. Chem. B* **2004**, *108*, 16642-16653.

46.   Kilsä. K.; Mayo. E. I.; Kuciauskas. D.; Villahermosa. R.; Lewis. N. S.; Winkler. J. R.; Gray. H. B. *J. Phys. Chem. A* **2003**, *107*, 3379-3383.

47.   Kilsä. K.; Mayo, E. I.; Brunschwig. B. S.; Gray. H. B.; Lewis, N. S.; Winkler, J. R. *J. Phys. Chem. B* **2004**, *108*, 15640-15651.

48.   Hou, Y.-J.; Xie. P.-H.; Zhang. B.-W.; Cao, Y.; Xiao. X.-R.; Wang. W.-B. *Inorg. Chem.* **1999**, *38*, 6320-6322.

49.   Redmond. G.; Fitzmaurice. D. *J. Phys. Chem.* **1993**, *97*, 1426-1430.

50.   Watson. D. F.; Meyer. G. J. *Coord. Chem. Rev.* **2004**, *248*, 1391-1406.

51.   Wang. P.; Zakeeruddin. S. M.; Moser. J.-E.; Humphry-Baker. R.; Grätzel. M. *J. Am.*

Chem. Soc. **2004,** *126,* 7164-7165.

52. Clark, C. C.; Marton, A.; Srinivasan, R.; Sarjeant, A. A. N.; Meyer, G. J. *Inorg. Chem.* **2006,** *45,* 4728-4734.

53. Oskam, G.; Bergeron, B. V.; Meyer, G. J.; Searson, P. C. *J. Phys. Chem. B* **2001,** *105,* 6867-6873.

54. Juirs, A.; Balzani, V.; Barigelletti, F.; Campagna, S.; Belser, P.; von Zelewsky, A. *Coord. Chem. Rev.* **1988,** *88,* 85-277.

55. Barqawi, K. R.; Murtaza, Z.; Meyer, T. J. *J. Phys. Chem.* **1991,** *95,* 47-50.

56. Bergkamp, M. A.; Gutlich, P.; Netzel, T. L.; Sutin, N. *J. Phys. Chem.* **1983,** *87,* 3877-3883.

57. Creutz, C.; Chou, M.; Netzel, T. L.; Okumura, M.; Sutin, N. *J. Am. Chem. Soc.* **1980,** *102,* 1309-19.

58. Damrauer, N. H.; Cerullo, G.; Yeh, A.; Boussie, T. R.; Shank, C. V.; McCusker, J. K. *Science* **1997,** *275,* 54-57.

59. Shaw, G.; Styers-Barnett, D. J.; Gannon, E. Z.; Granger, J. C.; Papanikolas, J. M. *J. Phys. Chem. A* **2004,** *108,* 4998-5006.

60. Shaw, G. B.; Brown, C. L.; Papanikolas, J. M. *J. Phys. Chem. A* **2002,** *106,* 1483-1495.

61. Zhao, J. H.; Wang, A. H.; Green, M. A.; Ferrazza, F. *Appl. Phys. Lett.* **1998,** *73,* 1991.

62. Waterland, M. R.; Kelly, D. F. *J. Phys. Chem. A* **2001,** *105,* 4019-4028.

63. Wenger, B.; Grätzel, M.; Moser, J.-E. *J. Am. Chem. Soc.* **2005,** *127,* 12150-12151.

64. Kallioinen, J.; Benkoe, G.; Myllyperkioe, P.; Khriachtchev, L.; Skrman, B.; Wallenberg, R.; Tuomikoski, M.; Korppi-Tommola, J.; Sundstroem, V.; Yartsev, A. P. *J. Phys. Chem. B* **2004,** *108,* 6365-6373.

65. Ramakrishna, G.; Jose, D. A.; Kumar, K. K.; Das, A.; Palit, D. K.; Ghosh, H. N. *J. Phys. Chem. B* **2005,** *109,* 15445-15453.

66. Ellingson, R. J.; Asbury, J. B.; Ferrere, S.; Ghosh, H. N.; Sprague, J. R.; Lian, T.; Nozik, A. J. *J. Phys. Chem. B* **1998,** *102,* 6455-6458.

67. Heimer, T. A.; Heilweil, E. J.; Bignozzi, C. A.; Meyer, G. J. *J. Phys. Chem. A* **2000**, *104*, 4256-4262.

68. Furube, A.; Katoh, R.; Yoshihara, T.; Hara, K.; Murata, S.; Arakawa, H.; Tachiya, M. *J. Phys. Chem. B* **2004**, *108*, 12583-12592.

69. O'Regan, B.; Moser, J.; Anderson, M.; Grätzel, M. *J. Phys. Chem.* **1990**, *94*, 8720-8726.

70. Hannappel, T.; Burfeindt, B.; Storck, W.; Willig, F. *J. Phys. Chem. B* **1997**, *101*, 6799-6802.

71. Bhasikuttan, A. C.; Suzuki, M.; Nakashima, S.; Okada, T. *J. Am. Chem. Soc.* **2002**, *124*, 8398-8405.

72. McCusker, J. K.; Walda, K. N.; Dunn, R. C.; Simon, J. D.; Magde, D.; Hendrickson, D. N. *J. Am. Chem. Soc.* **1993**, *115*, 298-307.

73. Noack, V.; Weller, H.; Eychmueller, A. *Phys. Chem. Chem. Phys.* **2003**, *5*, 384-394.

74. Thompson, D. W.; Kelly, C. A.; Farzad, F.; Meyer, G. J. *Langmuir* **1999**, *15*, 650-653.

75. Bergeron, B. V.; Marton, A.; Oskam, G.; Meyer, G. J. *J. Phys. Chem. B* **2005**, *109*, 937-943.

76. Kelly, C. A.; Farzad, F.; Thompson, D. W.; Stipkala, J. M.; Meyer, G. J. *Langmuir* **1999**, *15*, 7047-7054.

77. Bergeron, B. V.; Meyer, G. J. *J. Phys. Chem. B* **2003**, *107*, 245-254.

78. Liu, F.; Meyer, G. J. *Inorg. Chem.* **2005**, *44*, 9305-9313.

79. Clark, C. C.; Marton, A.; Meyer, G. J. *Inorg. Chem.* **2005**, *44*, 3383-3385.

80. Marton, A.; Clark, C. C.; Srinivasan, R.; Freundlich, R. E.; Narducci Sarjeant, A. A.; Meyer, G. J. *Inorg. Chem.* **2006**, *45*, 362-369.

81. Katz, J. E.; Lewis, N. S. *PhD Dissertation California Institute of Technology* **2007**.

82. Monat, J. E.; McCusker, J. K. *J. Am. Chem. Soc.* **2000**, *122*, 4092-4097.

Chapter 2. The Influence of Electrolyte Composition on the Electron Injection Process of the Solar Cell Sensitizer N3.

2.1 Introduction

Michael Grätzel's report of efficient generation of a photocurrent with a ruthenium dye, launched research in the area of dye sensitized solar cells (DSSCs).[1] Since the initial report[2,3] over 20 years ago, research in the field of DSSCs has increased dramatically.[4,5] The continual growth of the field of DSSC research is a testament to the intricate balance of this type of cell.

While there are a multitude of directions DSSC research can go, we have chosen to focus on one aspect of the cell; that being the impact of the electrolyte composition on election injection. The impact of electrolyte on the DSSCs has been reported in the literature, mainly in terms of overall efficiency and recombination/regeneration rates. Few, if any, reports have focused on the impact the electrolyte composition has on the injection processes of sensitizers bound to TiO_2. Most studies of injection rates utilize ultrafast pump-probe spectroscopic techniques, which indicate that the injection time-scale can be as fast as 50 fs and extend as long as 100 ps.[6-9] The majority of the studies concerning injection rates are done on samples exposed to air[6,7,10-13] or immersed in an electrolyte composed of small cations.[9,11,14] The following study illustrates the difference in the injection dynamics between TBA^+ and Li^+-based electrolytes. Both anions, $-I^-$ and $-ClO_4^-$, are also compared to determine if using $-ClO_4^-$ salts in place of the more optically dense $-I^-$ salts is an accurate substitution for monitoring injection processes in TiO_2 based solar cells. The Lewis group has reported that the presence of a $TBAI/I_2$ as the electrolyte decreases the overall efficiency of a N3 sensitized TiO_2-based cell compared to a LiI/I_2 electrolyte by a factor of approximately five.[15] The impact of both the cation and the anion on the injection will be discussed in this paper and the implications this has on the overall efficiency of the cell.

2.2 Experimental

All materials were purchased from commercial sources and used without further purification unless otherwise noted. The Lewis Group at California Institute of Technology provided the N3 sensitizer, TiO_2, and ZrO_2 films.

2.2.1 Photoelectrode Preparation

A "sandwich-cell" configuration was used to study the injection dynamics associated with different electrolyte solutions. The sandwich-cell configuration consists of a sensitized slide, a Teflon spacer, and a glass cover slide. This configuration has been reported previously and is described briefly below.[15]

TiO_2 films on F-doped SnO_2 coated glass, received from the Lewis group, were treated with a 0.2 M $TiCl_4$ and allowed to rest in contact with the $TiCl_4$ solution for at least 8 hours. This pretreatment step was done to deposit a fresh layer of TiO_2 on the surface, which should increase the ability of the sensitizer to bind to the surface. After 8 hours, the films were rinsed and sintered under flowing air at 450 °C for 30 minutes. After cooling to 120 °C, the films were maintained at 120 °C for an additional 2 hours. Immediately after the films were removed from the furnace they were placed in an ethanoic solution of the N3 dye. The films were allowed to soak for approximately 12 hours. After soaking, the sensitized films were rinsed and assembled with the desired electrolyte in an Ar atmosphere. Once assembled the films were kept in a light tight container.

As a control, ZrO_2 films were prepared. ZrO_2 has a band gap of ~5 eV which is larger than that of TiO_2 at ~3.0 eV, preventing the injection of an electron into ZrO_2. Since little to no injection is expected when the sensitizer is bound to ZrO_2, elucidation of dynamics associated with the injection process can be more readily identified rather than artifacts of binding the sensitizer to a substrate.[5] ZrO_2 films were prepared for dye adsorption in a similar manner as for TiO_2, although without treatment with the $TiCl_4$ solution. The clean ZrO_2 films were sintered at 450 °C for 30 minutes and again allowed to rest at 120 °C for

an additional two hours. The 120 °C films were then immersed in an ethanoic solution of N3 for a minimum of 24 hours, due to the decreased binding efficiency of ZrO_2 compared to TiO_2. Assembly of the cell was achieved, as above, in an Ar atmosphere.

2.2.2 Electrolyte Solution Preparation

Electrolyte solutions were prepared in an Ar atmosphere with ultra dry acetonitrile (Baker) and fused salts of the necessary supporting electrolyte. I_2 was incorporated into the solutions using standard Schlenk techniques. Solutions used for optical experiments are listed in Table 2-1. To ensure a large concentration of small positive ions in the Li^+-

Table 2-1. Lifetimes of N3 Bound to TiO_2 in the Presence of Various Electrolytes

N3/TiO_2	700 nm	800 nm
0.5 M $LiClO_4$ 0.05 mM CH_3CO_2H	9.0 ± 0.5 ps	5.6 ± 0.7 ps
0.5 M $TBAClO_4$	9.3 ± 0.5 ps	9.5 ± 1.0 ps
0.5 M LiI 0.05 mM CH_3CO_2H	14 ± 1.5 ps	13 ± 1.3 ps
0.5 M TBAI	--	--
0.5 M LiI 0.05 mM CH_3CO_2H 0.4 M I_2	22 ± 2.8 ps	15 ± 1.5 ps
0.5 M TBAI 0.4 M I_2	--	--

All electrolytes were in ultra dry acetonitrile

based electrolytes a small amount of acetic acid was added. All TBA^+ based electrolytes were allowed to equilibrate in contact with the film for three hours prior to measurement. The electrolyte solution of interest was introduced into the cell via one of two 30-gauge needles placed between the Teflon spacer and the glass cover slip. Slow injection from a 1 mL syringe (plastic) was done to ensure that air bubbles did not remain in the optical window. Figure 2-1 shows a typical sandwich cell setup.

2.2.3 Steady-state Electronic Absorption Measurements

Absorption spectra of N3 bound to TiO_2 and ZrO_2 were collected with an 8425A HP
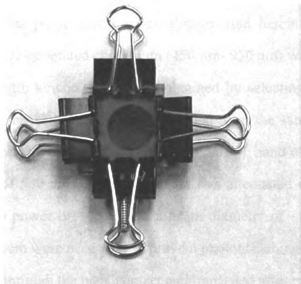
Figure 2-1. A typical sandwich cell used for time-resolved studies.

diode array spectrometer. Spectra were collected with and without correction for the TiO_2 or ZrO_2 background.

2.2.4 Photocurrent Measurements

Sensitized films were placed in an electrochemical cell specially designed to enable photocurrent measurements. Housed inside the cell are the counter and reference electrodes, a Pt wire and a Pt mesh, respectively. The working electrode, a sensitized film, was mounted so that constant contact with the electrolyte solution was maintained and positioned in close proximity to the Pt wire and Pt mesh. Illumination of the cell occurred through the back contact allowed the light to excite the N3 sensitizer without obstruction from the Pt electrodes. The back contact is considered to be the backside of the glass slide on which the film is deposited. A BAS potentiometer was used to scan the voltage from 200 mV to -800 mV in 5 mV steps. Current-voltage curves were only collected for electrolyte solutions that contain the I^-/I_3^- couple.

2.2.5 Femtosecond Time-Resolved Spectroscopy

The ultrafast pump-probe spectroscopy system used herein has been reported previously.[16] The sapphire-generated continuum (450 nm- 950 nm) was used as the probe source. Single wavelength kinetic traces were obtained by selecting wavelengths from the continuum with 10 nm band-pass filters positioned after the sample. Excitation of the films was achieved at the peak of the low energy MLCT band of N3 bound to TiO_2 corresponding to a λ_{ex} of 530 nm. The pump beam was attenuated with neutral density filters to obtain a pump power of ~ 2 μJ and a beam diameter of ~1 mm. Low power densities of the pump beam were necessary to prevent photobleaching of the N3 films.[17, 18] Films were illuminated through the back contact and translated after each scan, where one scan is one round trip of the delay stage, to ensure the integrity of the sample. The back contact is considered to be the backside of the glass slide on which the film is deposited, so that the beams are passing through the conductive glass, the sensitized film and then the electrolyte. This orientation also helps prevent some photobleaching. Absorption spectra were collected before and after time resolved measurements to determine the extent of photodecomposition of the films. The optical density of the N3 sensitized films at 530 nm was between 0.7-0.9 for TiO_2 and 0.3-0.5 for ZrO_2. At each probe wavelength, data was collected for both sensitized and bare films. Estimation of $\Delta t=0$ was achieved with signals from bare films or neat solvent at each prove wavelength. All measurements were performed at 298 K.

2.3 Results and Discussion

2.3.1 Steady-state Electronic Absorption Measurements

Blank TiO_2, N3 bound to TiO_2 in the presence of 0.5 M LiI with 50 mM CH_3CO_2H and N3 bound to TiO_2 in the presence of 0.5 M TBAI are shown in Figure 2-2. The spectra of the sensitized films were normalized at 540 nm to better compare the impact of the two electrolyte solutions on the ground state absorption spectra. Little to no shifting of
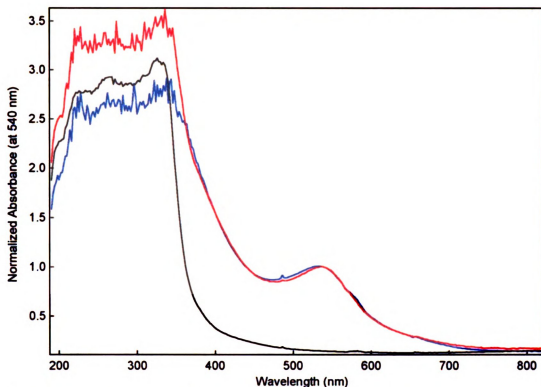
Figure 2-2. Absorption spectra of N3 Bound to TiO_2 in the presence of various electrolytes
Absorption spectra for TiO_2(—), N3/TiO_2 0.5 M LiI 50 mM CH_3CO_2H (—) and N3/TiO_2 0.5 M TBAI (—); normalized at 540 nm.

the low energy MLCT was observed between the two electrolyte solutions. The lack of a significant shift of the MLCT absorption between the two electrolyte solutions indicates that the [1]MLCT state was not significantly perturbed by the composition of the electrolyte.

2.3.2 Photocurrent Measurements

Figure 2-3 shows typical current-voltage curves for both Li^+ and TBA^+-based electrolytes. The Li^+-based electrolyte gave an open circuit voltage (V_{oc}) of approximately 475 mV and a short circuit current (i_{sc}) of approximately 3.3 mA, while the TBA^+-based electrolyte gave a V_{oc} of approximately 800 mV and an i_{sc} of approximately 0.2 mA.

An increase in V_{oc} was expected when changing from Li^+ to TBA^+ due to the fact that small cations, such as Li^+,[19] shift the flat-band potential of TiO_2 to more positive potentials thus reducing the V_{oc}. This positive shift is due to a band bending effect that
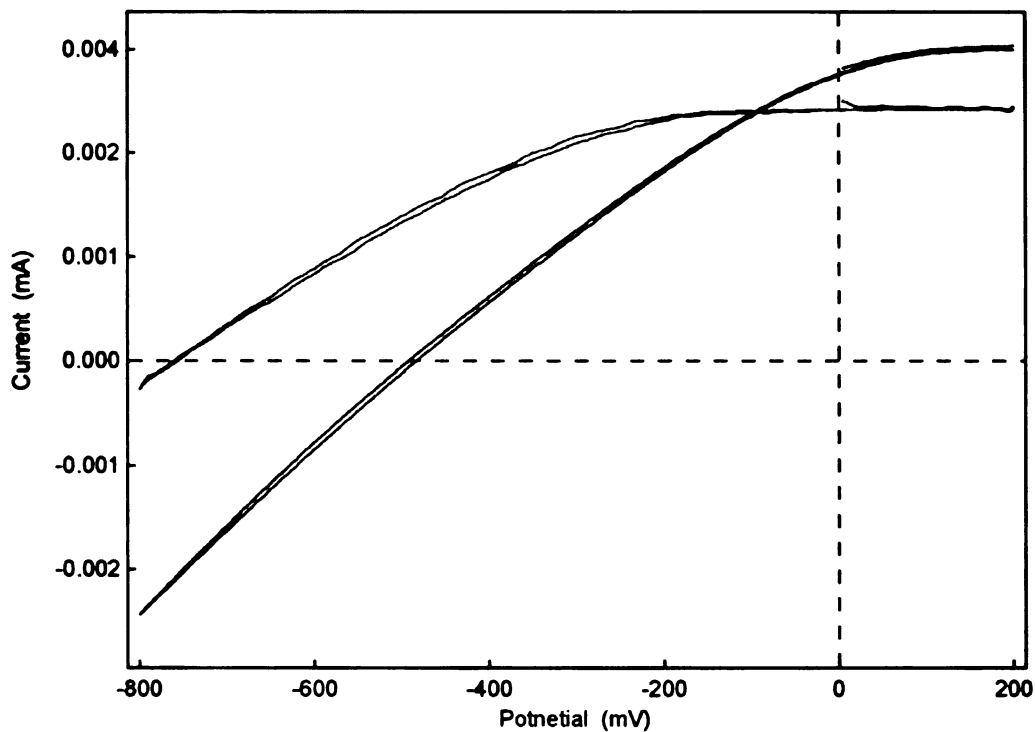
Figure 2-3. Current-voltage curves for N3 bound to TiO_2

Current-voltage traces for N3/TiO_2 in 0.5 M LiI 50mM CH_3CO_2H and 40 mM I_2 (—) and N3/TiO_2 in 0.5 M TBAI and 40 mM I_2 (—).

is most likely an electrostatic interaction between the small charges at the surface and the conduction band. The positive shift of the conduction band in the presence of small positive ions reduces the energy of the electron (V_{oc}) but it increases the driving force for electron injection from the sensitizer. Reduction of the i_{sc} between Li^+ and TBA^+ electrolytes may be due to a reduction in the injection yield; however, electrochemical measurements alone cannot determine if this is the case. Photocurrent measurements provide information on the energy of the electrons output from the cell and the number of electrons available for use; however, it provides no mechanistic information. Attempting to determine the source of a reduction in either the V_{oc} or the i_{sc} from a current-voltage alone is impossible, other techniques must be employed. Additionally, current-voltage curves can only be collected for electrolyte solutions that contain a redox couple, in this case the I^-/I_3^- couple, therefore spectroscopic measurements on the complete cell can prove difficult.

Most reports of optical measurements on sensitized TiO_2 films modify the electrolyte solution by substituting I⁻ salts with ClO_4^- salts or completely neglecting the electrolyte.[6, 7, 10-13] These simplifications made the cell more conducive to optical measurements; however, no redox species was present, which may impact the observed kinetics and thus the conclusions of the measurement. The most accurate way of determining the impact of the electrolyte on the injection process will require employing the I⁻/I_3^- couple when conducting optical measurements.

2.3.3 Injection Dynamics of N3 Sensitized Films

Dynamics associated with the injection process were probed with transient absorption difference spectroscopy. Excitation at 530 nm corresponds to exciting into the ¹MLCT state of N3. Probe wavelengths associated with the decay of the excited state (N3*) and the oxidized species (N3⁺) were chosen based on previously reported spectra.[20] The wavelengths of interest were 700 nm and 800 nm corresponding to dynamics of the excited state (N3*) and the oxidation product (N3⁺) respectively. When injection occurs we expect to see a decay of the N3* signal at 700 nm and a rise at 800 nm corresponding to the formation of N3⁺. These probe wavelengths are not ideal due to the fact that both N3* and N3⁺ have broad transitions that extend from 650 nm - 900 nm. The excited state, N3*, maximizes around 700 nm and the oxidized species, N3⁺, around 800 nm; each still possess small contributions from the other species. Despite the overlapping signals, 700 nm and 800 nm are the best wavelengths available to us currently to probe electron injection dynamics of N3 sensitized materials.

Ideally, we should be able to calculate an injection yield for N3 bound to TiO_2 in the presence of the different electrolytes. Calculating an injection yield requires that certain criteria be met to arrive at an accurate value. First, the sample should have a constant concentration of injecting species in the probe volume. Since these samples are translated and the films are not uniform, the concentration of N3 in the probe volume of a given scan may be different from the one before. Second, to get the most accurate value probing in a

region where only one species is contributing to the signal makes calculation of injection yield more accurate. When more than one species is present, it is difficult to account for the individual contributions they each make to the observed signal. Work is currently underway to enable detection of unique probe wavelengths that corresponds to the injected electron. Additionally, calculation of an accurate injection yield is hindered by the low pump intensities used to prevent photobleaching of the samples. The low pump intensities produce data that has small signal-to-noise ratios and thus any calculation of an injection yield would have a significant amount of error. Since we are exciting into the ^{1}MLCT state we should expect to see some injection from this initially populated state; however, due to the ultrafast lifetime of the ^{1}MLCT state we are unable to resolve any injection dynamics associated with its injection process. The observed dynamics in this study are due to injection from the long-lived ^{3}MLCT state, which has been well characterized. [20] Therefore, we can only qualitatively assess the impact of the different electrolytes on injection.

2.3.4 Dynamics Associated with Injection in N3 Sensitized Films and I⁻ Based Electrolytes

Photocurrent measurements on N3 sensitized TiO_2 films in the presence of LiI with I_2 and TBAI with I_2 yield dramatically different photocurrents as discussed above. LiI and TBAI salts were used to prepare electrolyte solutions that would best model the complete cell, yet still maintain an optically dilute electrolyte to facilitate the optical experiments of interest. To determine if the decrease in photocurrent was due to injection, N3/TiO_2 and N3/ZrO_2 films were prepared with the two electrolytes. ZrO_2 films provided a standard, in that injection from N3 cannot occur. Therefore, any dynamic processes observed on the ZrO_2 would be due to the electrolyte interaction with the excited state and be independent of injection.

Probing the ZrO_2 films at 700 nm (open triangles) yielded a positive signal that persisted at the same value for the duration of the time window for both electrolytes. The

positive feature observed with N3 bound to the ZrO_2 film was due to the absorption of the excited state that has a lifetime of approximately ~5 ns.[20, 21] Since injection cannot occur with N3 sensitized ZrO_2 films the observation of a constant signal was expected. Figure 2-4 shows the ZrO_2 data for both electrolytes at 700 nm probe (open triangles). The amplitude of the signal for the ZrO_2 films was smaller due to the reduced absorption cross-section of the films at 530 nm, stemming from the inability of ZrO_2 to bind N3 as well as TiO_2.
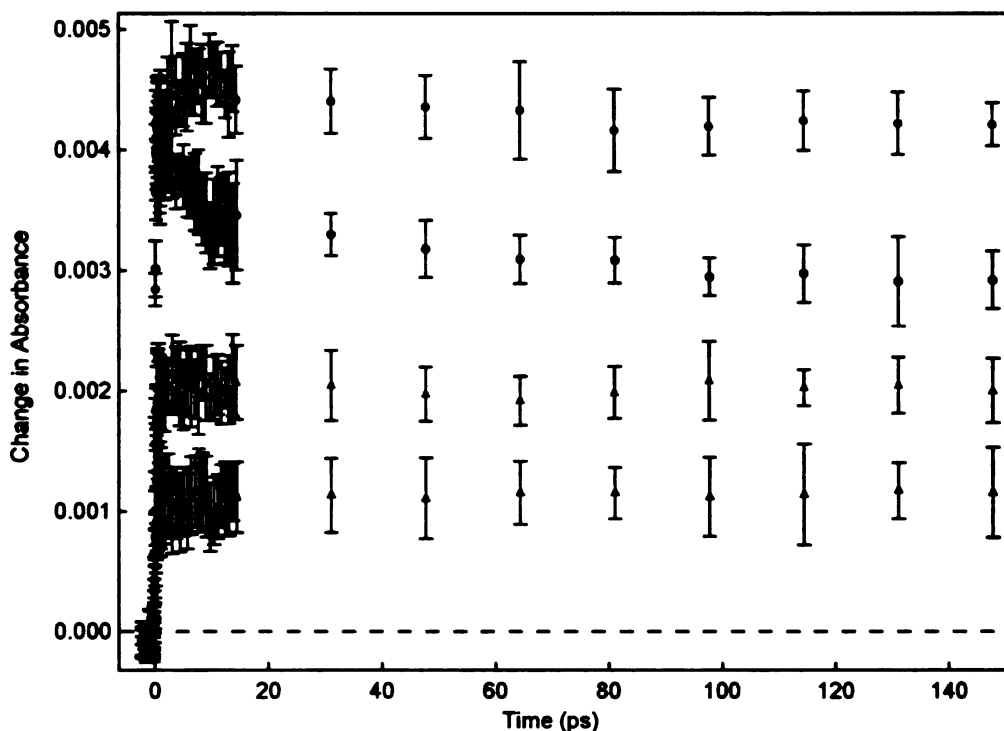
Figure 2-4. Transient absorption data for N3 bound to TiO_2: 700 nm probe.
530 nm pump and 700 nm probe for N3/TiO_2 with closed circles 0.5 M LiI 50 mM CH_3CO_2H (•) and N3/TiO_2 with 0.5 M TBAI (•) as closed circles. Corresponding N3/ZrO_2 data is also presented as the open triangles 0.5 M LiI 50 mM CH_3CO_2H (Δ) and 0.5 M TBAI (Δ).

Excited state deactivation of the N3 dye bound to TiO_2 monitored at 700 nm with LiI present exhibits an expected decay, associated with the loss of excited state population due to the injection of an electron. A single exponential fit of the 700 nm trace of N3 bound to TiO_2 in the presence of LiI yields a time constant of approximately 14 ps. Probing the

excited state deactivation at 700 nm with the TBAI electrolyte present exhibits a drastic difference from the excited state deactivation dynamics observed with the LiI electrolyte present. Data for the TBAI based electrolyte could not be fit, while there seemed to be a slight decay present, the small amplitude associated with this decay impaired the fitting of the trace. The marked decrease in the amplitude of decay of N3* in the presence of the TBAI electrolyte indicates that TBAI significantly impacts the injection dynamics of N3 bound to TiO_2. Closed circles in Figure 2-4 shows the marked difference in the ultrafast dynamics of N3 bound to TiO_2 in the presence of TBAI and LiI electrolytes. Although estimation of the injection yields could not be achieved for these samples, it is reasonable to assume that the amount of injection was significantly less for the TBAI electrolyte.

Probing the ZrO_2 films at 800 nm yielded a positive signal that persisted at the same value for the duration of the time window. Since injection cannot occur with the N3 sensitized ZrO_2 films, as mentioned above, the observation of a constant signal was also expected at 800 nm. The excited state has a broad absorption that extends past 800 nm, thus the signal observed at 800 nm on ZrO_2 was due to absorption of the excited state. Both electrolyte solutions, LiI and TBAI, show the similar positive signals with no dynamic features. Open triangles in Figure 2-5 shows the ZrO_2 data for both electrolytes at 800 nm probe. The amplitude of the signal for the ZrO_2 films was small due to a combination of reduced absorption of the films at 530 nm, stemming from the inability of ZrO_2 to bind N3, and that 700 nm was the maximum of the N3* signal.

Kinetics associated with the formation of the oxidized species, $N3^+$, were manifest as a signal that grew in amplitude over time. The LiI electrolyte data was well fit to a biexponential and yields time constants 1 ps and 15 ps. The 800 nm probe data for the TBAI based electrolyte could not be fit, while there seemed to be a slight rise the small amplitude associated with the rise impaired fitting the trace. Closed circles in Figure 2-5 shows the difference in the ultrafast dynamics of N3 bound to TiO_2 in the presence the TBAI and LiI electrolytes. Estimation of the injection yields could not be done; however, it is significant
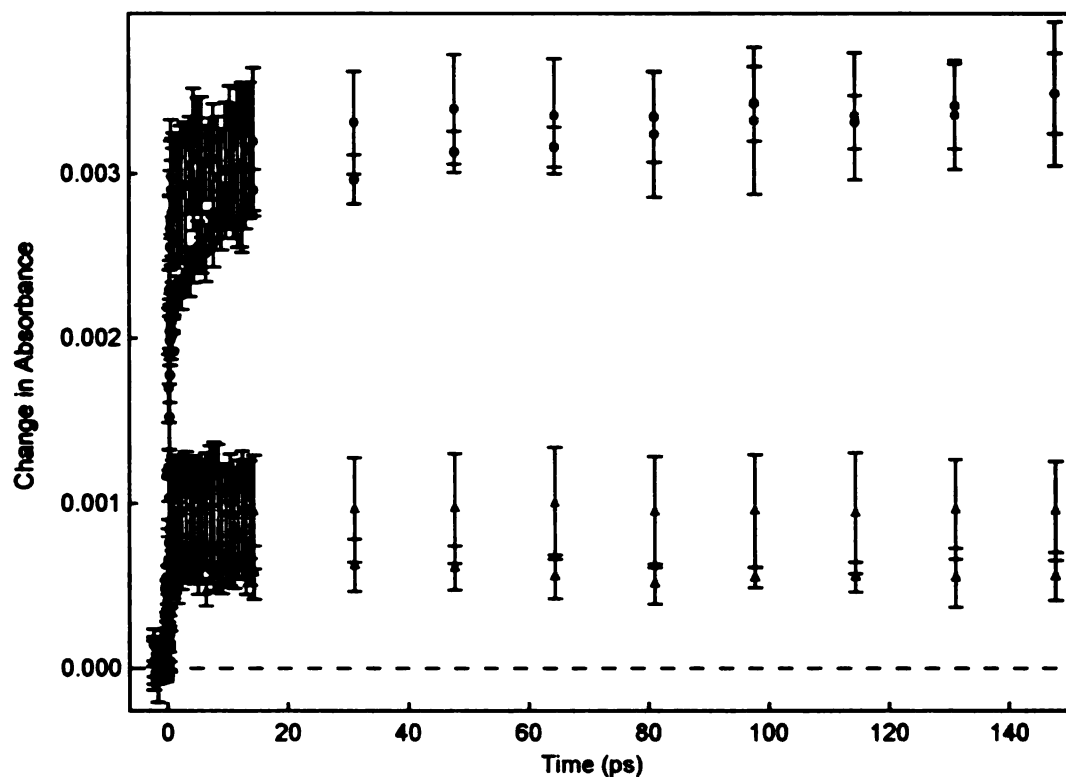
Figure 2-5. Transient absorption data for N3 bound to TiO₂; 800 nm probe.
530 nm pump and 800 nm probe for N3/TiO₂ with 0.5 M LiI 50 mM CH₃CO₂H (•) and N3/TiO₂ with 0.5 M TBAI (•) as closed circles. Corresponding N3/ZrO₂ data is also presented as the open triangles 0.5 M LiI 50 mM CH₃CO₂H (△) and 0.5 M TBAI (△)

to note the difference in the amplitude of rise associated with the TBAI electrolyte in comparison to the LiI electrolyte. This difference is most likely due to decreased injection from N3 into TiO_2 in the case of the TBAI electrolyte.

The difference in the excited state deactivation rates of N3 bound to TiO_2, Figure 2-4, and the differences in the rate of formation of N3⁺, Figure 2-5, indicate that electron injection is influenced by the composition of the electrolyte. The positive shift of the conduction band in the presence of Li⁺ most likely increased the injection yield of N3 into TiO_2; however, it was not possible to calculate an exact number. Additionally, data with N3 bound to ZrO_2 showed little difference between the two electrolyte solutions, indicating that on the timescale of this experiment the intrinsic excited state dynamics of N3 were not significantly impacted by the composition of the electrolyte.

2.3.5 Influence of I^-/I_3^- on Electron Injection in N3 Sensitized TiO_2 Films

Measuring the impact of TBAI and LiI electrolytes on the injection of N3 into TiO_2 without I_2 present may not have been the most accurate representation of the complete cell. A set of experiments was done to determine the impact I_2 had on the injection dynamics observed for the TBAI and LiI electrolytes. Due to the optical density of I^-/I_3^- in the visible region of the spectrum very few optical measurements on the ultrafast timescale have been done with the redox couple present.[14] The broad ground state absorption feature of the iodide redox couple dramatically decreases around 600 nm. thus ensuring probe wavelengths at 700 nm and 800 nm would not be significantly hindered by the strong absorption of the redox couple. Conveniently. illumination of the cells through the back contact ensures efficient excitation of the sensitizer with the visible excitation. so the sample is excited before the pump beam is attenuated by the optically opaque electrolyte. Maintaining the efficient excitation of the sensitizer and employing probe wavelengths that fall outside the I^-/I_3^- window. we should be able to monitor the dynamics of N3 bound to TiO_2 in a complete cell.

Figure 2-6 shows the kinetic traces at both 700 and 800 nm of N3 bound to TiO_2 in the presence of LiI and LiI with I_2. Similar measurements were done comparing TBAI and TBAI with I_2 electrolytes as shown in Figure 2-7. Since both TBAI and LiI electrolytes show such strong similarities with their corresponding I_2 electrolyte, we believe that using the more optically dilute -I^--based electrolytes are good model systems to study the injection dynamics of the sensitizer in DSSCs while maintaining an optically dilute electrolyte.

2.3.6 Dynamics Associated with Injection on N3 Sensitized Films and ClO_4^- Based Electrolytes

Many research groups overcome the optical density issues associated with the opaque redox couple by using media that has no transitions in the visible region of the spectrum. Often perchlorate salts are used due to the optically pure nature of the electrolyte
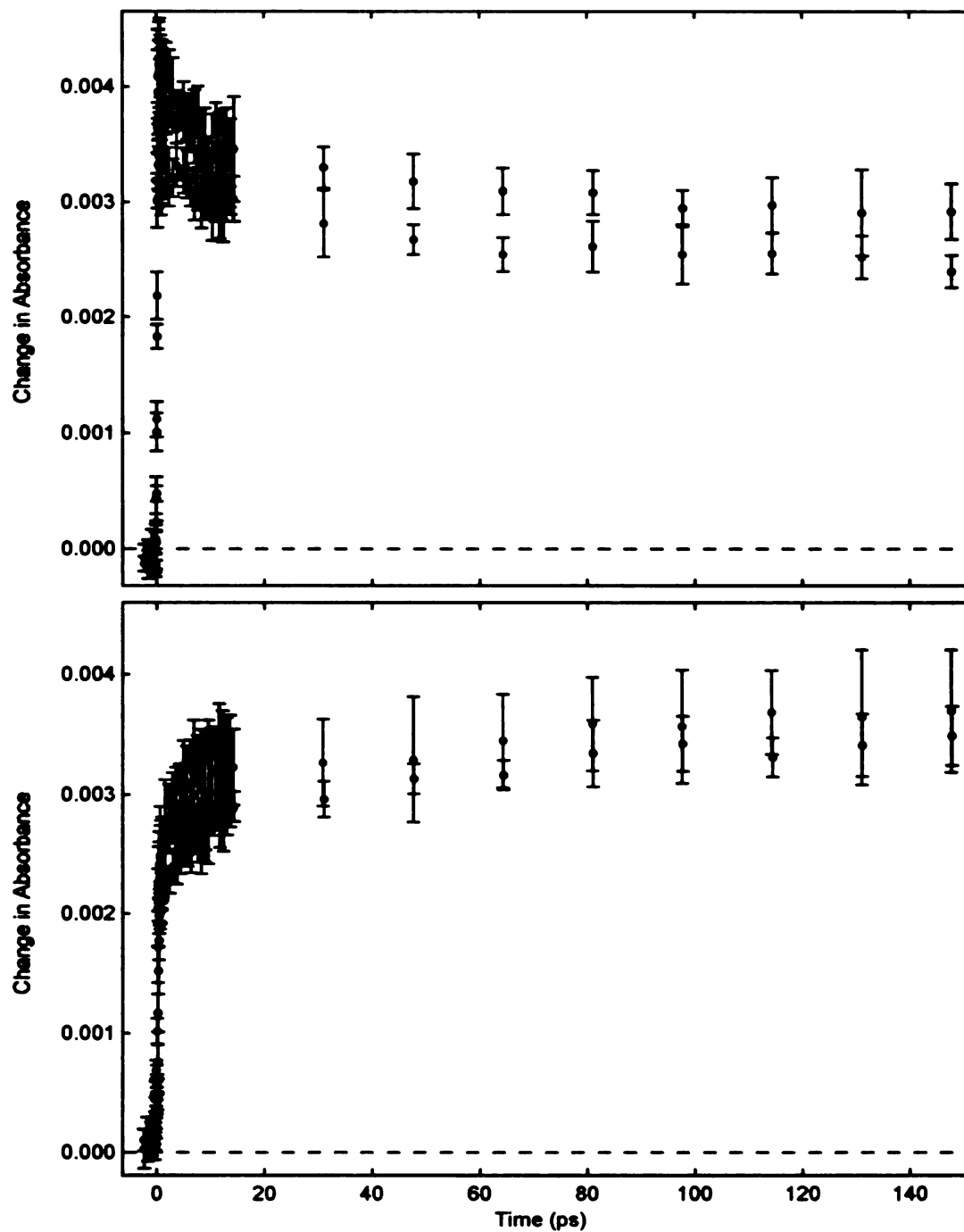
Figure 2-6. Transient absorption data for N3 bound to TiO_2 in the presence of LiI and I_2.

Top panel: 700 nm probe for $N3/TiO_2$ with 0.5 M LiI 50 mM CH_3CO_2H (•) and $N3/TiO_2$ with 0.5 M LiI 50 mM CH_3CO_2H and 40 mM I_2 (•) as closed circles. Bottom panel: 800 nm probe for $N3/TiO_2$ with 0.5 M LiI 50 mM CH_3CO_2H (•) and $N3/TiO_2$ with 0.5 M LiI 50 mM CH_3CO_2H and 40 mM I_2 (•) as closed circles.
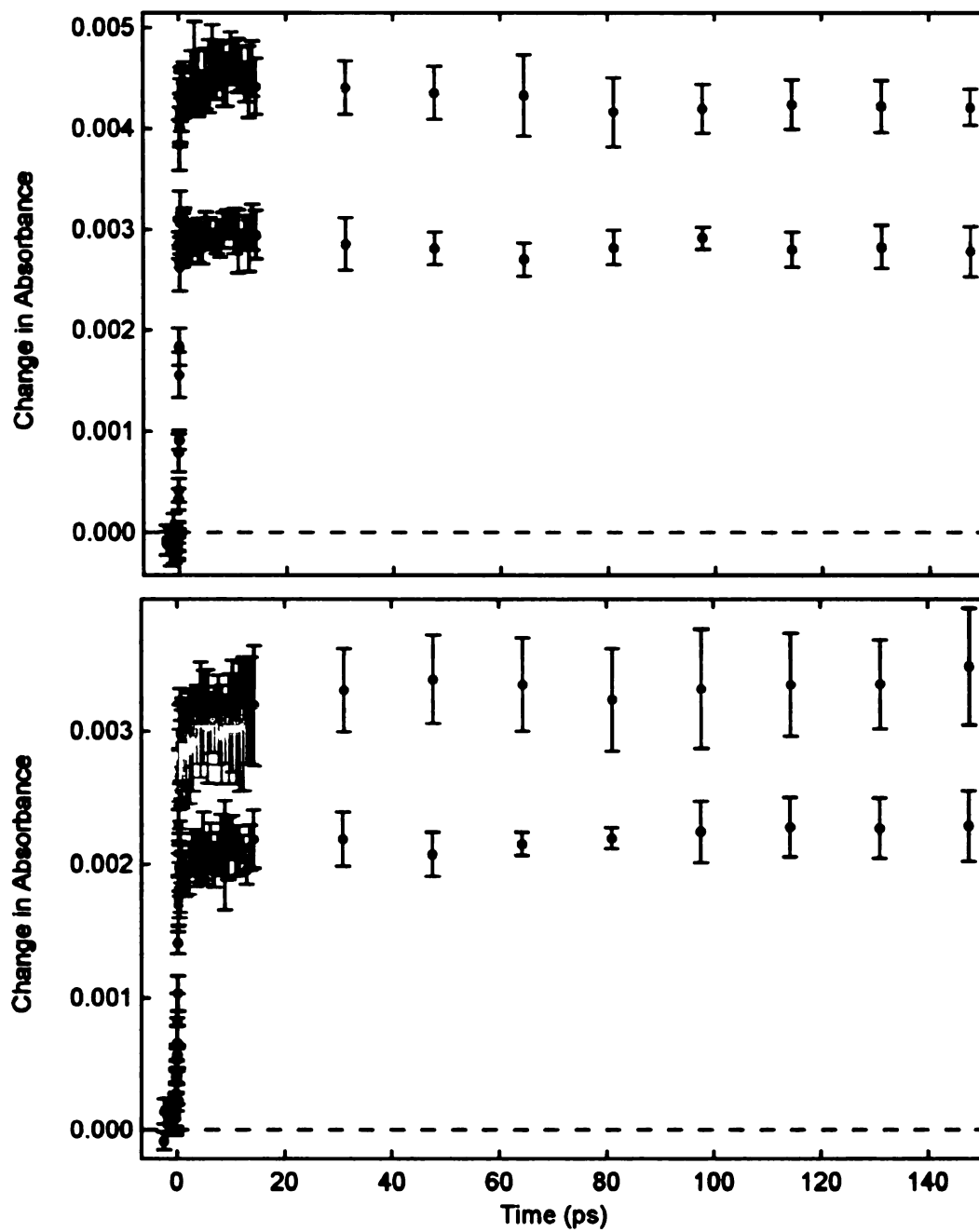
Figure 2-7. Transient absorption data for N3 bound to TiO$_2$ in the presence of TBAl and I$_2$.

Top panel: 700 nm probe for N3/TiO$_2$ with 0.5 M TBAl (•) and N3/TiO$_2$ with 0.5 M TBAl and 40 mM I$_2$ (•) as closed circles. Bottom panel: 800 nm probe for N3/TiO$_2$ with 0.5 M TBAl (•) and N3/TiO$_2$ with 0.5 M TBAl 40 mM I$_2$ (•) as closed circles.

with $LiClO_4$ or $TBAClO_4$ present. Using the perchlorate salts would provide the same concentration of the desired cation to achieve the desired position of the conduction band and would also enable probing optical transitions associated with N3 bound to TiO_2 that occur in the visible region of the spectrum. The hesitation to base this study solely on the dynamics of N3 bound to TiO_2 in perchlorate electrolytes was that the differences in the observed photocurrents were done so with I and I_2 present. Changing the electrolyte composition so drastically may not model the cell conditions well.

Kinetic traces of N3 sensitized TiO_2 in contact with ClO_4^--based electrolytes and -I-based electrolytes are shown as closed circles in Figures 2-8 and 2-9. Corresponding ZrO_2 data were collected and are shown as open triangle in each plot to provide a point of reference as to how the electrolyte impacts the intrinsic dynamics of the sensitizer.

Figure 2-8 shows the deactivation of N3* at 700 nm and in the case of $TBAClO_4$ and $LiClO_4$ electrolytes, the deactivation rate and amplitudes are almost identical. Similar result were observed for the rate of the growth of $N3^+$ at 800 nm probe (Figure 2-9). The kinetic similarity between the two ClO_4^--based electrolytes was interesting. As mentioned above, a stark difference was observed when the electrolyte was changed from TBAI to LiI; however, that was not the result with $TBAClO_4$ and $LiClO_4$ electrolytes.

If the presence I was a significant contributor to the reduced injection yield we should see a difference in the injection process when comparing the LiI and $LiClO_4$ electrolyte solutions. Figure 2-10 shows LiI and $LiClO_4$ at 700 and 800 nm probes. Lifetimes obtained from single exponential fitting of the 700 nm probe data shown in Figure 2-10 for the two solutions were similar. $LiClO_4$ was well fit with a lifetime of 9 ± 1 ps and LiI with a lifetime of 14 ± 2 ps at 700 nm probe. Similar differences arose at 800 nm probe where the $LiClO_4$ data was well fit with a lifetime of 8 ± 1 ps and LiI of 15 ± 1 ps. The small difference in the lifetimes between the -I and $-ClO_4^-$ electrolytes could be due to quenching of the excited state by I Figure 2-11 shows the corresponding data for the TBA^+ electrolytes. In the case of TBAI and $TBAClO_4$ the impact of I is more pronounced. The
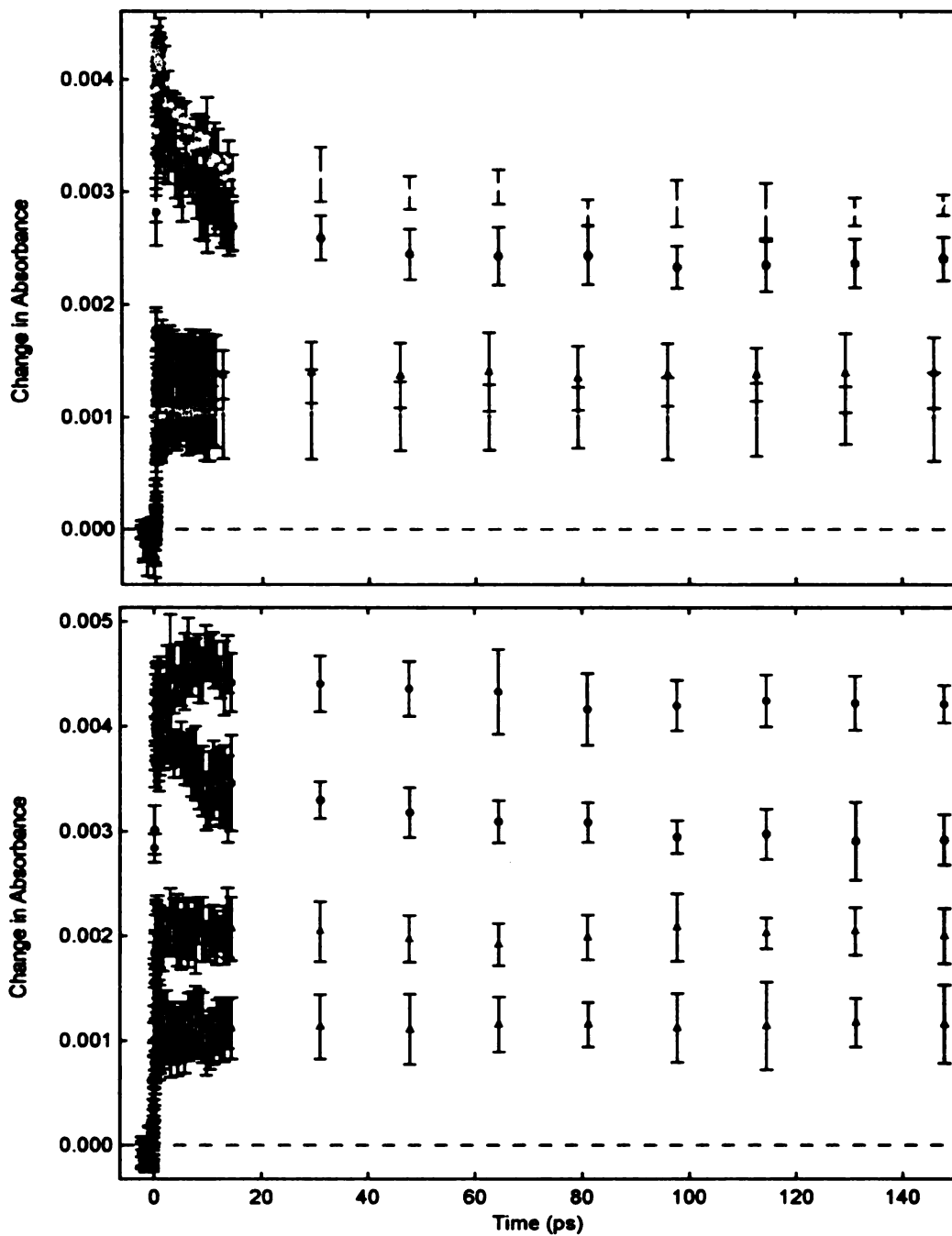
Figure 2-8. Transient absorption data for N3 TiO₂ or ZrO₂ at 700 nm probe.

Top panel: 700 nm probe after 530 nm excitation closed circles N3/TiO$_2$ in 0.5 M LiClO$_4$ 50 mM CH$_3$CO$_2$H(•), N3/TiO$_2$ in 0.5 TBAClO$_4$( ) and corresponding ZrO$_2$ data as open triangles N3/ZrO$_2$ in 0.5 M LiClO$_4$ 50 mM CH$_3$CO$_2$H(Δ), N3/ZrO$_2$ in 0.5 M TBAClO$_4$( ). Bottom panel: 700 nm probe for N3/TiO$_2$ with 0.5 M LiI 50 mM CH$_3$CO$_2$H(•) and N3/TiO$_2$ with 0.5 M TBAI(•) as closed circles and corresponding N3/ZrO$_2$ data as open triangles 0.5 M LiI 50 mM CH$_3$CO$_2$H(Δ) and 0.5 M TBAI(Δ).
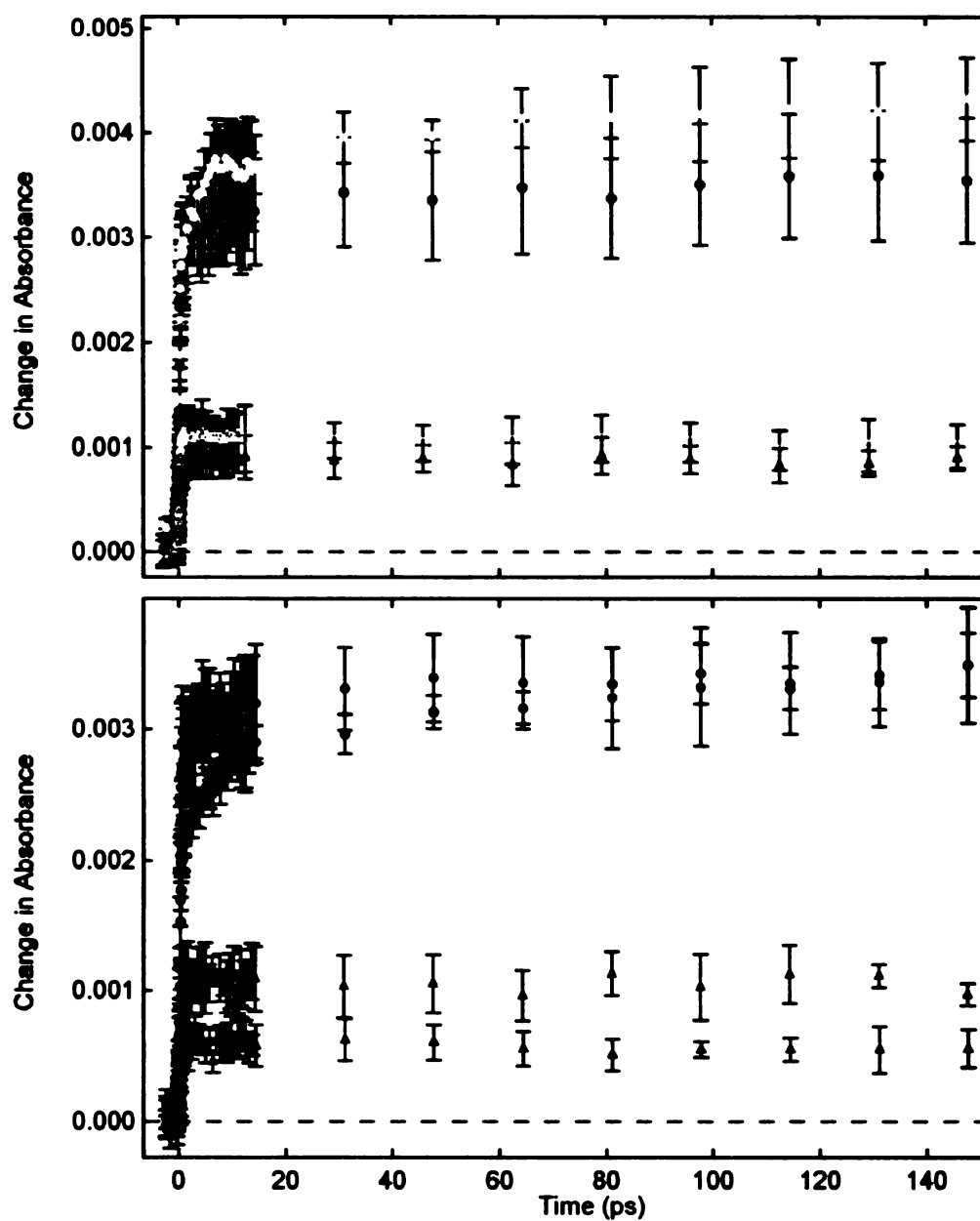
Figure 2-9. Transient absorption data for N3/TiO$_2$ or ZrO$_2$ at 800 nm probe.

Top panel: 800 nm probe following 530 nm excitation, closed circles N3/TiO$_2$ in 0.5 M LiClO$_4$ 50 mM CH$_3$CO$_2$H (•), N3/TiO$_2$ in 0.5 TBAClO$_4$ ( ) and corresponding ZrO$_2$ data as open triangles N3/ZrO$_2$ in 0.5 M LiClO$_4$ 50 mM CH$_3$CO$_2$H (Δ), N3/ZrO$_2$ in 0.5 M TBAClO$_4$ ( ). Bottom panel: 800 nm probe for N3/TiO$_2$ with 0.5 M LiI 50 mM CH$_3$CO$_2$H (•) and N3/TiO$_2$ with 0.5 M TBAI (•) as closed circles and corresponding N3/ZrO$_2$ data as open triangles 0.5 M LiI 50 mM CH$_3$CO$_2$H (Δ) and 0.5 M TBAI (Δ).
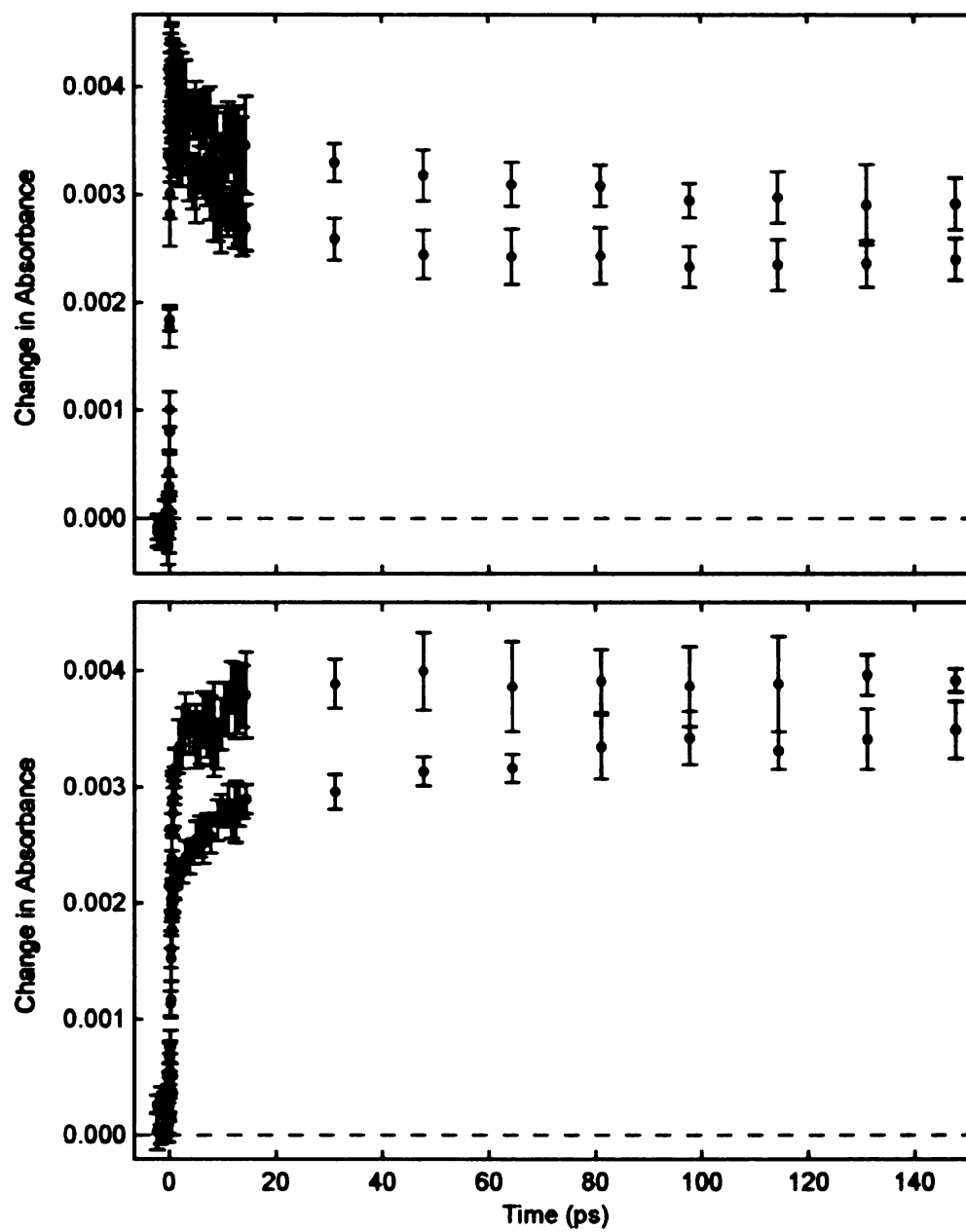
Figure 2-10. Transient absorption data for N3/TiO₂ in the presence of Li⁺-based electrolytes.

Top panel: 700 nm probe for N3/TiO₂ with 0.5 M LiI 50 mM CH₃CO₂H (•) and N3/TiO₂ with 0.5 M LiClO₄ 50 mM CH₃CO₂H (•) as closed circles. Bottom panel: 800 nm probe for N3/TiO₂ with 0.5 M LiI 50 mM CH₃CO₂H (•) and N3/TiO₂ with 0.5 M LiClO₄ 50 mM CH₃CO₂H (•) as closed circles.
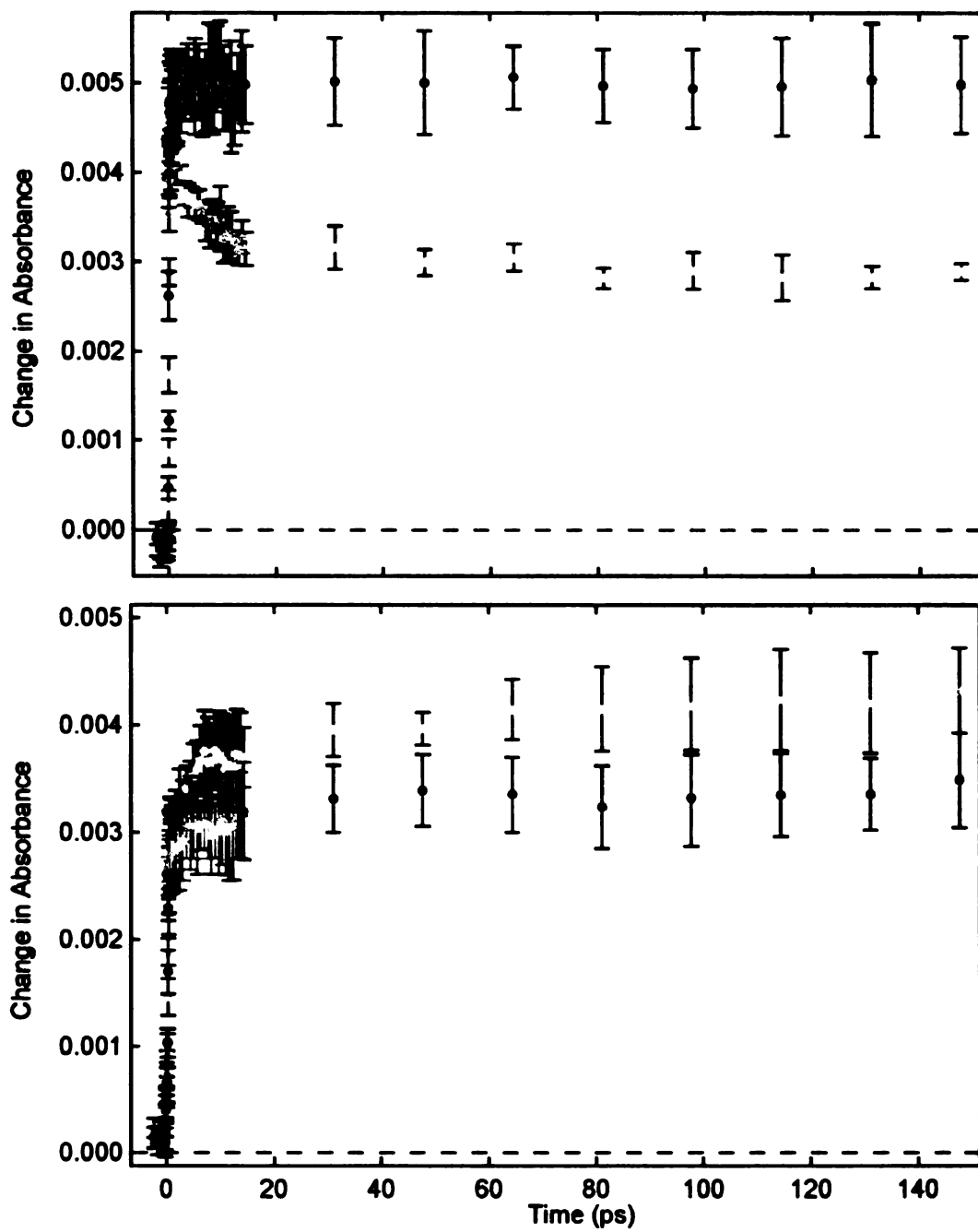
Figure 2-11. Transient absorption data for N3/TiO$_2$ in the presence of TBA$^+$-based electrolytes.
Top panel: 700 nm probe for N3/TiO$_2$ with 0.5 M TBAI (•) and N3/TiO$_2$ with 0.5 M TBAClO$_4$ ( ) as closed circles. Bottom panel: 800 nm probe for N3/TiO$_2$ with 0.5 M TBAI (•) and N3/TiO$_2$ with 0.5 M TBAClO$_4$ ( ) as closed circles.

TBAI traces could not be fit due to the small amplitude attributed with the decay process and the large error associated with the traces; however, fitting the TBACIO$_4$ traces yields similar lifetimes as those found for LiClO$_4$. At 700 nm probe TBACIO$_4$ was well fit with a lifetime of 9 ± 1 ps and 9.5 ± 1 ps at 800 nm. Perchlorate data for both cations showed little to no difference in the observed lifetimes. The similarity in lifetimes indicates that the driving force for electron injection is remaining constant between the LiClO$_4$ and TBACIO$_2$ electrolytes. For this to be true the ^{3}MLCT excited state must be shifting more negative by the same amount the conduction band shifts. The difference between the two TBA$^+$ containing electrolytes also indicates that the anion can play a significant role in the injection dynamics of a sensitizer.

Some research has been presented that suggests I⁻ readily quenches the excited state of some sensitizers thus inhibiting the ability for the sensitizer to undergo electron injection into TiO$_2$.[22-25] Meyer and coworkers have studied TBAI electrolyte solutions and found that increasing the concentration of Li⁺ in the electrolyte increased the injection yields of the systems.[26] While the quenching affect of I⁻ must be considered, we must also remember that the conduction band is sensitive to the concentration of small positive charges in the electrolyte and addition of Li⁺ ions will shift the conduction band to more positive potentials thus increasing the driving force for electron transfer.

2.4 Conclusions

By comparing both LiI and TBAI electrolytes with and without the redox active I⁻/I$_3$⁻ couple we can more readily assess the impact the cation has on the injection process and the implication these cations have on the overall efficiency of N3 sensitized TiO$_2$ based solar cells. The significant decrease in the photocurrent is most likely due to a combination of a more negative conduction band edge with the presence of TBA⁺ and the ability of I⁻ to quench the excited state of the N3 sensitizer. By employing conditions that accurately model those of a functional cell we are able to more readily account for the kinetic differences between the two electrolyte solutions.

From this study we have found that it is essential to employ conditions that model the functional cell as closely as possible. In using the more optically transparent ClO_4^- based electrolytes we would have neglected the critical impact that I^- has on the injection process. The ClO_4^- data shows that there is little impact on the injection when the cation is changed for TBA^+ to Li^+, which is not the case for the $-I^-$ data. Injection measurements that have been made in the presence of electrolytes that do not contain I^- may not be an accurate account of the actual injection processes occurring in the cell. We have shown that spectroscopic measurements on the injection dynamics associated with DSSCs are best done in the presence of I^- to achieve the most accurate picture of the injection process that occurs in the complete cell.

It is difficult to pin point the one factor that leads to the five-fold decrease in the observed efficiencies of the TBA^+ and Li^+ electrolytes but we can conclude that the TBAI electrolyte reduces the injection observed in these experiments. Any difference in the injection dynamics of N3 in the presence of $LiClO_4$ or $TBAClO_4$ were not observed, indicating that shifting the conduction band more negative is not the sole contributor to the reduced efficiency. Additionally, the quenching of the excited state of N3 is not significant enough to inhibit the injection of N3 in the presence of LiI based electrolytes. These two results indicate that the more negative potential of the conduction band in the presence of TBA^+ and the quenching ability of I^- on the excited state of N3 causes a significant decrease in the injection process. One suggestion has been proposed that the combination of the TBA^+ and the I^- causes the conduction band to shift negative enough to shutoff injection from the long-lived triplet state, placing the conduction band edge between the ^1MLCT state and the ^3MLCT state. A concern with this idea is that in a 1993 report, the conduction band is actually more positive with TBAI present than with $TBAClO_4$ present, which would imply that we should see a more pronounced decrease in the $TBAClO_4$ electrolyte. An additional suggestion has implied that the electrolyte shifts the excited states of the sensitizers enough to allow injection in the presence of the $TBAClO_4$ electrolyte and shut

it off in the presence of TBAI electrolyte. Another possible scenario is that the conduction band is shifted negative enough in the presence of TBAI that the rate of electron injection form the ^{3}MLCT state is comparable with that of the excited state quenching of I⁻. To determine which is the most correct mechanism additional experiments need to be done. One of those is the determination of the energies of the ^{3}MLCT state in the presence of the different electrolytes. This will enable us to determine if the excited state is affected by the electrolyte.

From these results we conclude that it is most likely the impaired injection process that decreases the overall efficiency of the functional cell when TBAI is present in the electrolyte. We have also shown that injection studies need to be done in situation that most accurately model the functional cell, which includes employing the more optically opaque I⁻ salts.

2.5 References

1. O'Regan, B.; Grätzel, M. *Nature* **1991**, *353*, 737.

2. Desilvestro, J.; Grätzel, M.; Kavan, L.; Moser, J.; Augustynski, J. *J. Am. Chem. Soc.* **1985**, *107*, 2988-2990.

3. Vlachopoulos, N.; Liska, P.; Augustynski, J.; Grätzel, M. *J. Am. Chem. Soc.* **1988**, *110*, 1216-1220.

4. Grätzel, M. *Inorg. Chem.* **2005**, *44*, 6841-6851.

5. Kalyanasundaram, K.; Grätzel, M. *Coor. Chem. Rev.* **1998**, *77*, 347-414.

6. Ellingson, R. J.; Asbury, J. B.; Ferrere, S.; Ghosh, H. N.; Sprague, J. R.; Lian, T.; Nozik, A. J. *J. Phys. Chem. B* **1998**, *102*, 6455-6458.

7. Asbury, J. B.; Ellingson, R. J.; Ghosh, H. N.; Ferrere, S.; Nozik, A. J.; Lian, T. *J. Phys. Chem. B* **1999**, *103*, 3110-3119.

8. Asbury, J. B.; Anderson, N. A.; Hao, E.; Ai, X.; Lian, T. *J. Phys. Chem. B* **2003**, *107*, 7376-7386.

9. Guo, J.; Stockwell, D.; Ai, X.; She, C.; Anderson, N. A.; Lian, T. *J. Phys. Chem. B* **2006**, *110*, 5238-5244.

10. Asbury, J. B.; Wang, Y.; Lian, T. *J. Phys. Chem. B* **1999**, *103*, 6643-6647.

11. Ai, X.; Anderson, N. A.; Guo, J.; Lian, T. *J. Phys. Chem. B* **2005**, *109*, 7088-7094.

12. Asbury, J. B.; Hao, E.; Wang, Y.; Ghosh, H. N.; Lian, T. *J. Phys. Chem. B* **2001**, *105*, 4545-4557.

13. Kuciauskas, D.; Monat, J. E.; Villahermosa, R.; Gray, H. B.; Lewis, N. S.; McCusker, J. K. *J. Phys. Chem. B* **2002**, *106*, 9347-9358.

14. Bauer, C.; Boschloo, G.; Mukhtat, E.; Hagfeldt, A. *J. Phys. Chem. B* **2002**, *106*, 12693-12704.

15. Katz, J. E. California Institue of Technology, 2007.

16. Juban, E. A.; McCusker, J. K. *J. Am. Chem. Soc.* **2005**, *127*, 6857-6865.

17. Hansen, G.; Gervang, B.; Lund, T. *Inorg. Chem.* **2003**, *42*, 5545-5550.

18. Kallioinen, J.; Benkoe, G.; Myllyperkioe, P.; Khriachtchev, L.; Skrman, B.; Wallenberg, R.; Tuomikoski, M.; Korppi-Tommola, J.; Sundstroem, V.; Yartsev, A. P. *J. Phys. Chem. B* **2004**, *108*, 6365-6373.

19. Redmond, G.; Fitzmaurice, D. *J. Phys. Chem.* **1993**, *97*, 1426-1430.

20. Tachinana, Y.; Moser, J. E.; Grätzel, M.; Klug, D. R.; Durrant, J. R. *J. Phys. Chem. B* **1996**, *100*, 20056-20062.

21. Waterland, M. R.; Kelly, D. F. *J. Phys. Chem. A* **2001**, *105*, 4019-4028.

22. Nasr, C.; Hotchandani, S.; Kamat, P. *J. Phys. Chem. B* **1998**, *102*, 4944-4951.

23. Marton, A.; Clark, C. C.; Srinivasan, R.; Freundlich, R. E.; Narducci Sarjeant, A. A.; Meyer, G. J. *Inorg. Chem.* **2006**, *45*, 362-369.

24. Clark, C. C.; Marton, A.; Srinivasan, R.; Sarjeant, A. A. N.; Meyer, G. J. *Inorg. Chem.* **2006**, *45*, 4728-4734.

25. Clark, C. C.; Marton, A.; Meyer, G. J. *Inorg. Chem.* **2005**, *44*, 3383-3385.

26. Wang, D.; Mendelsohn, R.; Galoppini, E.; Hoertz, P. G.; Carlisle, R. A.; Meyer, G. J. *J. Phys. Chem. B* **2004**, *108*, 16642-16653.

Chapter 3. Ultrafast Dynamics of a Model Iron(II) Sensitizer: Probing the Deactivation of the ^{1}MLCT State to the Ligand Field Manifold.

3.1 Introduction

In 2000, Monat and McCusker published a report on the ultrafast lifetime of a model sensitizer for TiO_2-based solar cells that focused on a unique iron(II) polypyridyl complex.[1] Their report was the first to quantify a lifetime of the ^{1}MLCT state of the iron(II) complex which was ~100 fs. The 2000 study used 400 nm excitation and probed at ~600 nm to isolate a signal that possessed a special spectroscopic handle that made it possible to identify the charge transfer state and the long-lived excited state.

Characterization of the long-lived excited state of and array of iron(II) complexes has been the focus of an area of physical inorganic research interested in the spin crossover nature of several complexes. Spin crossover complexes are unique in that their lowest energy excited state 1) is of different spin multiplicity and 2) is thermally accessible. The implementation of a technique called laser induced excited spin state trapping (LIESST) provided a significant amount of insight into the interconversion between low-spin and high-spin spin crossover complexes. The temporal resolution of these experiments limited the research to monitoring the long-lived states associated with these spin crossover complexes. A report in 1980 by Norman Sutin and coworkers concerning the excited state dynamics of a series of iron(II) complexes showed that the long-lived excited state, of all the iron(II) complexes studied, was populated within the instrument response time of the apparatus (~10 ps).[2] In 1993, Hendrickson and coworkers reconfirmed that the long-lived excited state of multiple iron(II) complexes was formed within the instrument response time of their apparatus.[3,4]

The availability of laser systems with ~100 fs pulses provide the opportunity to probe the dynamics associated with the early time excited state dynamics of iron(II) polypyridyl complexes. The previously mentioned 2000 report by Monat and McCusker

indicated that the initially populated ^{1}MLCT state deactivated to the long-lived ^{5}T$_2$ state in ~100 fs. An additional report of the ~100 fs ultrafast lifetime of the ^{1}MLCT state in a series of iron(II) complexes has recently been presented. With the understanding of the ultrafast nature of the ^{1}MLCT excited state of iron(II) polypyridyl complexes we set out to completely characterize the system employed in the initially report of these ultrafast dynamics, the [Fe(tren(6-R-py)$_3$)]$^{2+}$ complex.

[Fe(tren(6-R-py)$_3$)]$^{2+}$, where tren(py)$_3$ is tris(2-pyridymethyliminoetyl)amine and the 6-position on the pyridyl ring is substituted with either a -H or a -CH$_3$, is a unique complex in that depending on the nature of -R either a high-spin complex (R = -CH$_3$) or a low-spin complex (R = -H) is isolated. This substitution enables the synthesis of complexes that possess the opposite ground state from each other. The proximity of the two complexes to the spin crossover point enables this unique ground state situation. In this study the low-spin -H substituted complex is used for all transient measurements, while the high-spin -CH$_3$ substituted complex is used to model the long-lived excited state of the low-spin complex. With this unique situation we are able to calculate what the difference spectrum of the long-lived excited state looks like, which provides a spectroscopic tag to identify when this state is populated. We also employ spectroelectrochemical methods to determine the absorptive features of the MLCT state. These two spectral tags provide a spectroscopic handle for identification of both the ^{1}MLCT state and the long-lived ^{5}T$_2$ state. We found that after excitation at 560 nm the lifetime of the ^{1}MLCT state is ~100 fs and the vibrational cooling time of the ^{5}T$_2$ complex is ~10 ps. This is consistent with the report of Monat and McCusker and is indicates that the excited state dynamics are independent of excitation wavelength.[1]

3.2 Experimental

3.2.1 Synthesis

General. All reagents were obtained from commercial sources and used without

further purification unless noted. Elemental analyses were obtained through the Analytical Facilities at Michigan State University. ^{1}H NMR spectra were collected on a Varian 300 MHz spectrometer. The solvent used for each electronic absorption measurement is indicated below.

Tren•4HCl. The tren ligand tri(ethylamino)amine was purified according to literature methods.[5] A solution of 20.0 mL of methanol containing 10.0 mL (0.0668 mmol) of (2-aminoethyl)-amine (tren) was cooled to 0° C. Drop wise addition of 12 M HCl (16.7 mL) caused a white precipitate to form which was collected and recrystallized by addition of cold methanol to hot water. Calc. for tren•4HCl ($C_6H_{22}N_4Cl_4$): C, 28.20%; H, 8.28%; N, 21.92%. Found: C, 28.37%; H, 8.52%; N, 21.64%. ^{1}H NMR ($CDCl_3$) δ(ppm, multiplicity): 4.7 (s); 3.0 (t, J=7 Hz); 2.7 (t, J=7 Hz).

$FeCl_2$•$2H_2O$. Purification of $FeCl_2$•$4H_2O$ to $FeCl_2$•$2H_2O$ was done according to a literature method with the following modifications.[6] A round bottom flask was charged with 10 g (0.050 mol) of $FeCl_2$•$4H_2O$ with 50 mL of H_2O, and 0.42 g (7.5 mmol) of Fe^0. The solution was degassed and brought to reflux for five minutes under Ar. Then 2.0 mL of 12 M HCl was added and the reaction was maintained at reflux for 30 minutes, during which the solution changed from orange to pale green. Vacuum distillation removed excess water, leaving a few pale green crystals amongst white powder indicating a mixture of $FeCl_2$•$4H_2O$ and $FeCl_2$•$2H_2O$.

[Fe(tren(py)$_3$](PF$_6$)$_2$. The low-spin complex was synthesized by a modified literature procedure.[7] A Schiff base reaction was carried out to generate the tren(py)$_3$ (tris(2-pyridymethyliminoetyl)amine) ligand by dispersing 0.56 g (2.0 mmol) of tren•4HCl and 0.64 g (6.0 mmol) of 2-carboxaldehydepyridine in 25 mL of methanol containing 0.44 g (8.0 mmol) of NaOCH$_3$. The resulting solution was added to a round bottom flask charged with 0.33 g (2.0 mmol) of **2** under an inert atmosphere, producing a deep-purple solution, which generated the chloride salt. The chloride salt was metathesized by the addition 0.74 g (4.0 mmol) of solid potassium hexafluorophosphate to a saturated methanol

solution of the chloride salt producing the hexafluorophosphate salt. Further purification by ether diffusion into a saturated acetonitrile solution of the hexafluorophosphate complex produced crystals, which were collected and dried under vacuum to yield analytically pure product. Calc. for [Fe(tren(py)$_3$](PF$_6$)$_2$ (C$_{24}$H$_2$N$_7$P$_2$F$_{12}$Fe) (3): C, 37.98%; H, 3.58%; N, 12.91%. Found: C, 37.82%; H, 3.44%; N, 12.81%. UV-Vis, nm (ϵ, M^{-1}cm^{-1}): 204 (95 000); 234 (29 000); 276 (39 000); 370 (8 800); 516 (11 000); 560 (15 000).

[Fe(tren(6-Me-py)$_3$](PF$_6$)$_2$. The high-spin complex was synthesized by a modified literature procedure.[x] A Schiff base reaction was carried out to generate the tren(6-Me-py)$_3$ ligand (tris(6-methyl-2-pyridymethyliminoetyl)amine) by dispersing 0.2 g of distilled tren and 0.468 g of 6-methyl-2-carboxaldehydepyridine in 20 mL of methanol and allowed to stir 18 hours. The resulting solution was then degassed by bubbling dry N$_2$ into the solution. Once degassed the solution was then transferred to a round bottom flask charged with 0.24 g of 2 under an inert atmosphere, producing a deep-purple solution, which generated the chloride salt. Metathesis to the -PF$_6$ salt was achieved by the addition of 0.59 g of ammonium hexafluorophosphate to a saturated methanol solution of the hexafluorophosphate salt producing the desired compound. Further purification by ether diffusion into a saturated acetone solution produced a microcrystalline solid, which was collected and dried under vacuum to yield analytically pure product. Calc. for [Fe(tren(6-Me-py)$_3$](PF$_6$)$_2$ (C$_{27}$H$_{33}$N$_7$P$_2$F$_{12}$Fe): C, 40.47%; H, 4.15%; N, 12.23%. Found: C, 40.47%; H, 4.44%; N, 12.02%. UV-Vis, nm (ϵ, M-1cm-1): 204 (68 000); 234 (26 000); 292 (31 000); 496 (2 200).

3.2.2 Steady-state electronic absorption spectroscopy

Static absorption measurements were recorded with a Hewlett-Packard HP8452A diode array spectrophotometer. Molar absorptivities for each complex were acquired by serial dilution in acetonitrile.

3.2.3 Electrochemistry and spectroelectrochemistry

Electrochemical measurements were carried out with a BAS 100A electrochemical analyzer. Solutions of compounds were dissolved in degassed HPLC grade acetonitrile with 0.1 M Bu_4NPF_6 as the supporting electrolyte. A standard three-electrode setup was used with a Ag working electrode, a Pt wire counter electrode, and a Ag/Ag(NO_3) reference electrode. All measurements were made in an N_2 filled glovebox.

Once the first reduction and oxidation potentials were obtained for each complex spectroelectrochemical measurements were carried out as described previously.[1] Again, the desired complex was dissolved in HPLC grade acetonitrile and Bu_4NPF_6 was added to yield a 0.1 M solution of the supporting electrolyte. The concentration of the desired complex in a typical spectroelectrochemical measurement was 5×10^{-3} M. Depending on the spectral region of interest the concentrations were varied to enable spectral resolution in that region. Using a vitreous carbon working-electrode the sample was either oxidized or reduced and spectral are collected at predetermined time intervals. A fresh sample was used for each reductive and oxidative spectrum.

Spectroelectrochemical measurements provide insight into the absorptive properties of the lowest energy charge transfer state providing an initial guess as where the [1]MLCT state will absorb. Thus, we can use the spectroelectrochemical results as a guide as to where to probe for the spectroscopic handle of [1]MLCT state.

3.2.4 Nanosecond time-resolved transient absorption spectroscopy

Transient absorption data was collected with the nanosecond apparatus previously reported with the following modifications.[9] Probe wavelengths higher in energy of 350 nm required exchanging the glass achromats and cemented doublets that composed the probe beam path for quartz singlets. With the quartz lenses, probe wavelengths from 270 nm to approximately 900 nm were available. Pulsing of a Hamamatsu L2274 Xe arc lamp with an Applied Photophysics Arc Lamp Pulser generated the white light continuum. A Hamamatsu

R446 PMT detector was used for all nanosecond measurements. Each wavelength was an average of 15 sweeps, which was fit to a monoexponential decay function. Difference spectra were generated by plotting the pre-exponential factor acquired from the fit of the kinetic trace at each wavelength. Samples were prepared with an optical density between 0.5 and 0.8. Excitation energies were on the order of 2 mJ at 560 nm. Linearity of signals was verified.

3.2.5 X-ray absorption spectroscopy

Steady-state XAS on solutions of $[Fe(tren(py)_3)](PF_6)_2$ and $[Fe(tren(6-Me-py)_3)](PF_6)_2$ was performed in fluorescence mode at the iron K-edge on beam line 10.3.2 at the Advanced Light Source (ALS). A detailed description of the beam line has been reported previously.[10] 0.02 M solutions of the iron(II) complexes of interest are dissolved in acetonitrile and placed in thin walled quartz capillary tubes (0.3 mm thick), mounted on an x-y translation stage.

Transient XAS measurements were performed in a non-collinear pump-probe geometry on beam line 5.3.1 at the ALS; specifics on experimental details were discussed elsewhere.[11] Briefly, a 100 fs, 350 μJ, 400 nm pulse derived by frequency doubling the output of a 1 kHz Ti:sapphire femtosecond laser system initiates the iron(II) transition. The sample consists of a 0.5 mm thick free-flowing jet of 0.02 M $Fe[tren(py)_3](PF_6)_2$ dissolved in acetonitrile at room temperature. A single 70 ps synchrotron x-ray pulse, known as the camshaft pulse, was used to probe the photochemical reaction at the Fe K- edge.

3.2.6 Femtosecond time-resolved spectroscopy

The ultrafast pump-probe spectroscopy system used herein has been reported previously.[9]

Excitation energy was attenuated with neutral density filters and adjusted to a value that ensured a linear molecular response. The pump beam intensity was on the order of 5-6 μJ at a wavelength corresponding to the peak of the low energy metal to ligand charge

transfer (MLCT) transition. Linearity was verified. The optical density of the sample at the excitation wavelength was on the order of 0.6-0.8 in aerated HPLC grade acetonitrile.

Continuum generation was achieved by focusing 805 nm light into a 1 cm thick plate of translated CaF_2 yielding probe wavelengths from 330 nm to 900 nm. Early time full spectral data was corrected for temporal chirp by adjusting for $\Delta t=0$ from a solvent trace. Chirp-correction was needed to account for the fact that different wavelengths of light travel through a medium at different speeds. Due to the nature of the chirp correction early time spectra can look blocky and rough, further details on chirp correction have been reported previously.[12] The presented spectra were also smoothed with a boxcar averaging method available in WaveMetrics fitting program IGOR.

Depending on the wavelength of interest, single wavelength kinetic traces were acquired by selecting a small portion of the continuum with 10 nm band-pass filters or by selecting the desired wavelength with a second Light Conversions TOPAS. Neat solvent in 1 mm path length quartz cuvettes or a two-photon absorber, such as trichlorotoluene in acetonitrile, was used to establish $\Delta t=0$.

The output from the TOPAS was attenuated to ensure linear response of the signal and passed through an appropriate 10 nm band pass filter. Magic angle for each probe wavelength was checked prior to collection. Since the output from the TOPAS is linearly polarized, either vertically or horizontally, additional steps were needed to ensure magic angle polarization of the probe beam. Using uncoated Al mirrors, we were able to rotate the polarization of the TOPAS output to ensure magic angle polarization and maintain our temporal resolution. Parallel orientation of two mirrors maintains the input polarization through the two reflections; however, a perpendicular arrangement of the two mirrors causes the polarization to flip 90 °. By making small adjustments to a parallel set of mirrors the desired magic angle be achieved.

3.3 Results and Discussion

3.3.1 Steady-state electronic absorption

Figure 3-1 shows a drawing of the molecules of interest. The -R position on the pyridyl ring is significant in that when a -H is present the iron(II) complex that forms is a low-spin d^6 complex, which is reported to have a ground state of $^1A_1$. When -CH$_3$ is present at the -R position the iron(II) complex that forms is a high-spin iron(II) complex, with a ground state that is $^5T_2$ in nature. This unique feature of the [Fe(tren(6-R-py)$_3$)]$^{2+}$ complexes is what prompted us to use this system to study the excited sate processes in iron(II) complexes. The ligand field imposed by the tren(6-R-py)$_3$ ligand is such that either complex lies close enough to the spin crossover line for a d^6 complex that the slight modification of the ligand produces a complex that has a different ground state. Despite the proximity of the spin crossover point neither of these complexes are "spin crossover" complexes. To be a spin crossover complex the $^5T_2$ or $^1A_1$ state must be close enough in energy to the ground state that it can be thermally populated, this is not the case for the [Fe(tren(6-R-py)$_3$)]$^{2+}$ complexes. Considering the electronic impact the tren(6-Me-py)$_3$

		Ground State	Low Energy Excited State
[Fe(tren(6-R-py)$_3$)]	(R= H)	$^1A_1$	$^5T_2$
[Fe(tren(6-R-py)$_3$)]	(R= CH$_3$)	$^5T_2$	$^1A_1$
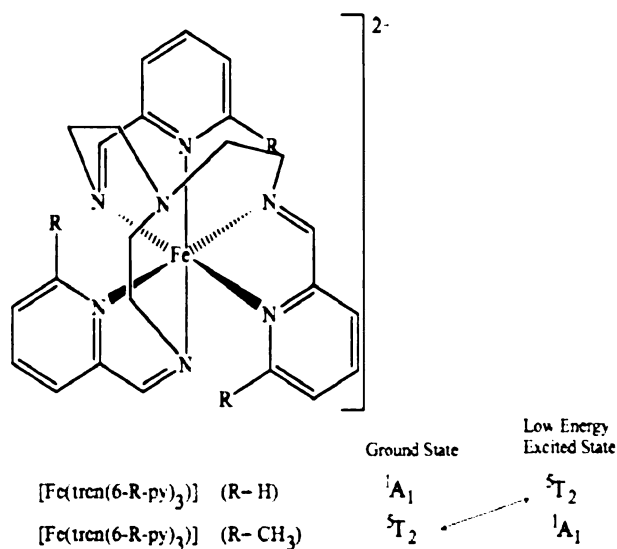
Figure 3-1. Schematic representation of [Fe(tren(6-R-py)$_3$)](PF$_6$)$_2$.

ligand on the spin state of iron(II), we would expect to isolate a low-spin complex, since -CH$_3$ is an electron donating substituent making the pyridyl moiety a better base. However, steric effects are the dominating factor in the generation of the high-spin complex, [Fe(6-Me-py)$_3$]$^{2+}$. The -CH$_3$ moiety is close enough to the N that the binding of the iron is impaired, resulting in a decrease in the overlap of the Fe-N orbitals thus weakening the effective ligand field of the complex and stabilizing the $^5T_2$ state.

Of the two complexes, the low-spin complex is the molecule of interest for this study due to its strong charge transfer transitions (^{1}MLCT) in the visible (Figure 3-2 Top). These strong charge transfer transitions in the visible are beneficial because they provide a good absorption cross-section for excited state production. Due to the nature of pump-probe spectroscopy we need to ensure that we produce as large an excited state population as possible. The high-spin complex with a ground state of $^5T_2$ (Figure 3-2 Middle), provided an means of acquiring an absorption spectrum of the long-lived excited state of the low-spin complex, which is reported to be $^5T_2$ in nature.[1] The availability of the high-spin complex enables us to calculate the difference spectrum of the low-spin complex in its long-lived excited state (Figure 3-2 Bottom) and thus enables us to determine when the long-lived excited state has been formed.

As mentioned above, the molecule of interest is the low-spin complex, where the $^1A_1$ to MLCT transitions dominate the visible region of its absorption spectrum. The weak transitions present in the visible region of the spectrum of the high-spin analogue indicate that the $^5T_2$ state absorbs weakly in this region. If we were able to excite 100 % of the sample into the excited state manifold we would expect to see an absorption spectrum that resembled that of the [Fe(6-Me-py)$_3$]$^{2+}$ complex. Due to experimental limitations we typically excite ~10 % of the sample, to identify the absorptive features of the excited state we must collect difference measurements where the excited state signal is collected and a difference is take between excited state signal and its ground state signal. Once the ground state is no longer populated we no longer observe the spectroscopic transitions
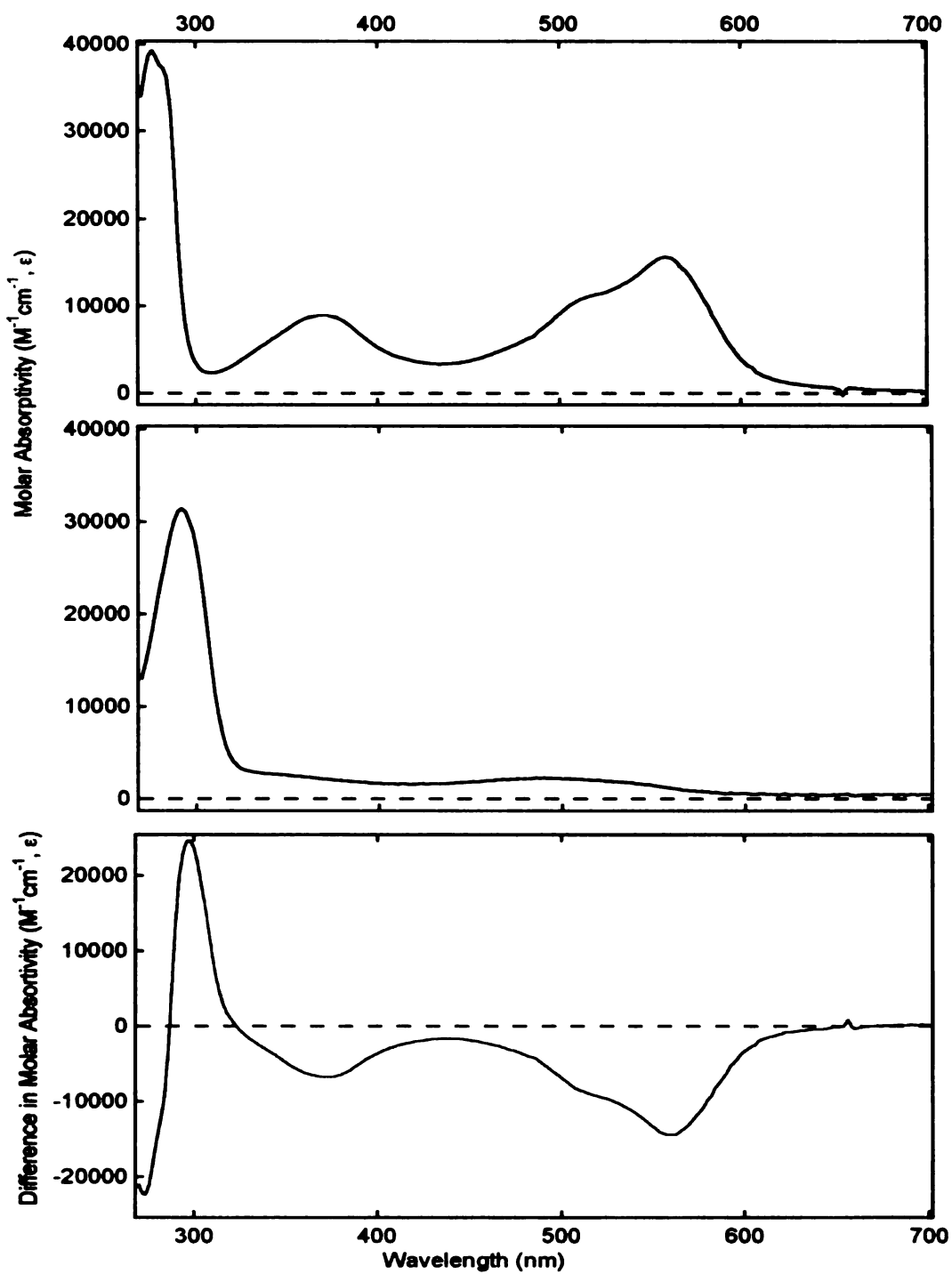
Figure 3-2. Molar absorptivities of $[Fe(tren(6-R-py)_3)](PF_6)_2$.

Top: $[Fe(tren(6-R-py)_3)](PF_6)_2$ where R= H, the low-spin complex $(GS = {}^1A_1)$; Middle: $[Fe(tren(6-R-py)_3)](PF_6)_2$ where R= CH_3, the high-spin complex $(GS = {}^5T_2)$; Bottom: Calculated difference spectrum $({}^5T_2 - {}^1A_1)$ of low-spin complex $[Fe(tren(py)_3)](PF_6)_2$.

associated with it, which results in a negative signal. In math terms it can be simplified as Δ, the difference is the product of a subtraction of the ground state signal from the excited state, Δ = ES - GS. In a case where the ground state absorbs more than the excited state, Δ = 0 - 1 = -1, and the converse is true for a case where the excited state absorbs more then the ground state, Δ = 1 - 0 = +1. Considering the excited state difference features of the low-spin complex, the combination of strong absorptions in the $^1A_1$ ground state with weak absorptions in the $^5T_2$ long-lived excited state will manifest as a negative signal termed a bleach, across the majority of the visible spectrum. The bleach is due to the fact that once the $[Fe(tren(py)_3]^{2+}$ is excited into its excited state manifold its ground state, the one that possess the strong absorption features in the visible, is no longer populated. In the UV; however, the excited state absorbs more than the ground state so we would expect a positive signal in this region.

A calculated difference spectrum is shown in Figure 3-2 Bottom. This difference spectrum is generated by subtracting the absorption spectrum of the molar absorptivity values of the low-spin $[Fe(tren(py)_3)]^{2+}$ complex absorption spectrum from that of the high-spin $[Fe(tren(6-Me-py)_3)]^{2+}$ and the UV region exhibiting positive features. Using the calculated difference spectrum we are able to identify several spectral tags that are indicative of the formation of the $^5T_2$ state. These tags will provide spectroscopic handles to identify when the $^5T_2$ state has been populated.

3.3.2 Electrochemistry and Spectroelectrochemistry

Electrochemical experiments on $[Fe(tren(py)_3)]^{2+}$ indicate that the first reduction of the ligand system occurs reversibly around -1.5 V and the oxidation of the iron(II) center occurs reversibly at +0.7 V. Acquisition of these potentials enables the collection of spectroelectrochemical data on $[Fe(tren(py)_3)]^{2+}$. Spectroelectrochemical data provides a means to generate the two halves of a charge transfer transition. In the case of iron(II) complexes, the typical charge transfer transitions are metal-to-ligand in nature therefore, oxidation of the metal center and reduction of the ligand system make up the two parts of

a MLCT transition. As shown in Figure 3-3 both reductive and oxidative waves exhibit absorptions in both the blue (< 500 nm) and the red (> 600 nm) regions. From 500 nm to 600 nm, both spectra exhibit a bleach, characteristic of loss of the ground state complex. Spectroelectrochemical data are also reported as difference spectra therefore we observe there the electrochemically-generated species absorbs more than the ground state species. Except for the positive features at ~295 nm and >600 nm, most likely due to ligand-to-metal transition, the oxidative spectrum is dominated by the loss of the ground state. The reductive spectrum exhibits strong absorptions across the 400 nm region and red of 600 nm, most likely due to the reduced ligand system. Absorption spectra of the radical anion of 2,2'-bipyridine has been reported to have strong absorptions around 350 nm with a harmonic around 650 nm[13], and despite the presence of pyridine rather than bipyridine the spectra correlate well.
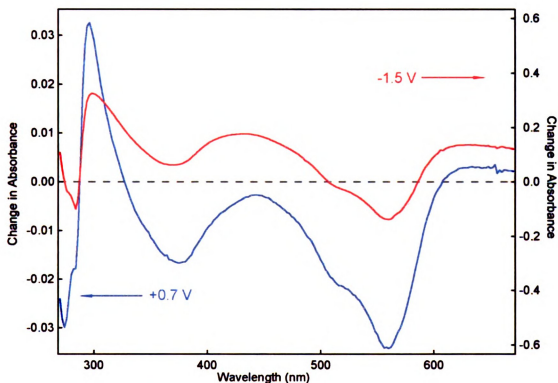
Figure 3-3. Spectroelectorchemical spectra of [Fe(tren(py)$_3$)](PF$_6$)$_2$.
Reductive data is shown by the red trace and oxidative data is shown by the blue trace. Reduction and oxidation potentials used to generate the spectra are provided in corresponding colors.

Positive features identified in the spectroelectrochemical measurements provide a spectral handle for the identification of the population of the MLCT state in $[Fe(tren(py)_3)]^{2+}$, since a MLCT state is a simultaneous reduction of the ligand system and an oxidation of the metal center. Attempting to use the signals present in the bleach region of the spectroelectrochemical data to identify a charge transfer state would be difficult since these signals are due to loss of ground state, which occurs when the complex is in any of its excited states, not just a charge transfer state. Observing positive signals in time resolved measurements around 400 nm and >600 nm will indicate the population of the MCLT of $[Fe(tren(py)_3]^{2+}$.

3.3.3 Nanosecond Time-Resolved Transient Absorption Spectroscopy.

The ground state recovery lifetime of the long-lived excited state in $[Fe(tren(py)_3)]^{2+}$ was found to be 57 ± 6 ns across the entire spectrum in Figure 3-4. The lifetime associated with ground state recovery was determined by fitting kinetic traces to a monoexponential decay function, where the fit yields a preexponential factor, A_0, and a lifetime, τ. The preexponential factor is used to generate the difference spectrum shown in Figure 3-4, by plotting A_0 versus wavelength. This difference spectrum is associated with the long-lived excited state of $[Fe(tren(py)_3)]^{2+}$ in acetonitrile. The dynamics associated with probe wavelengths from 280 nm to 350 nm have not been reported. This UV region is of interest because the signals are net positive, indicating that the long-lived excited state absorbs more than the ground state. These wavelengths can be used to directly probe the formation of the long-lived excited state. Again monoexponential fits of the kinetic data in this region yield lifetimes of ~57 ns. Ground state recovery dynamics of $[Fe(tren(py)_3)]^{2+}$ from 350 nm to 620 nm were published in 2000 by Monat and McCusker, where they also observed complete ground state recovery of the long-lived excited $^5T_2$ state with a lifetime of ~60 ns.

Scaling the calculated difference spectrum from Figure 3-2 Bottom and plotting it with the nanosecond difference spectrum, shows an excellent agreement between the
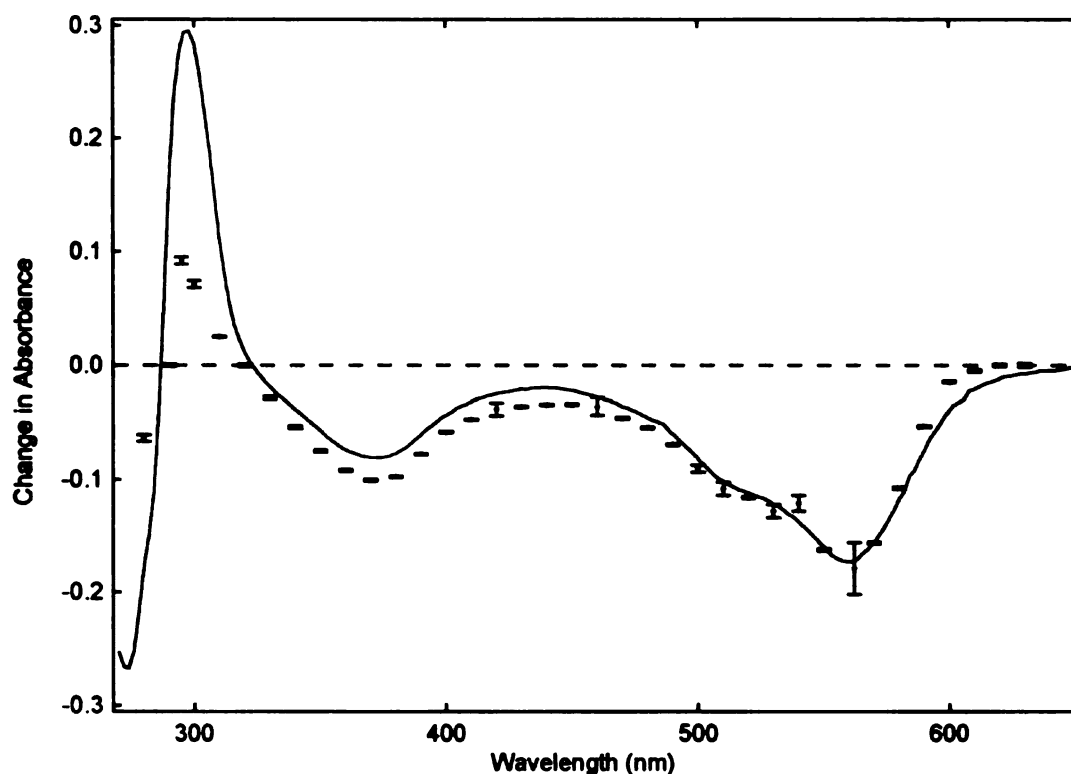
Figure 3-4. Difference spectra of [Fe(tren(py)$_3$)](PF$_6$)$_2$ in acetonitrile.

The calculated difference spectrum (^{5}T$_2$- 1A$_1$) of low-spin complex [Fe(tren(py)$_3$)](PF$_6$)$_2$ is shown as the red line; however, it has been scaled to match the nanosecond data at 560 nm. A nanosecond transient absorption spectrum is plotted as black dots. The strong correlation between the two spectra indicates that [Fe(tren(py)$_3$)](PF$_6$)$_2$ is in the ^{5}T$_2$ state on the nanosecond time scale.

two spectra. We expect there to be a strong correlation between the calculated difference spectrum (red trace in Figure 3-4) and the constructed difference spectrum if the long-lived excited state of [Fe(tren(py)$_3$)]$^{2+}$ is ^{5}T$_2$ in nature. Agreement between these two spectra indicates that: 1) [Fe(tren(py)$_3$]$^{2+}$ has a long-lived excited state that is ligand field in nature and classified as the ^{5}T$_2$ state, 2) complete ground state recovery from the ^{5}T$_2$ state happens with a time constant of 57 ± 6 ns, and 3) employing [Fe(tren(6-Me-py)$_3$]$^{2+}$ as a means of acquiring a spectrum of the long-lived excited state is a valid assumption.

3.3.4 X-ray Absorption Spectroscopy (XAS).

A collaborative effort with the Schoenlein group at Lawrence Berkeley Livermore National Lab produced a paper in 2006 that reported on the time resolved X-ray absorption spectroscopy of [Fe(tren(py)$_3$)]$^{2+}$.[11] A brief description of the findings are reported below.

This collaboration used X-ray absorption spectroscopy to probe the structural changes that occur in [Fe(tren(py)$_3$]$^{2+}$ after excitation with 400 nm radiation.

Knowing the long-lived excited state of the low-spin [Fe(tren(py)$_3$]$^{2+}$ is well modeled by its high-spin analogue [Fe(tren(6-Me-py)$_3$]$^{2+}$ X-ray absorption near-edge structure (XANES) and extended X-ray absorption fine structure (EXAFS) data for both complexes was collected at the Advanced Light Source. Figure 3-5 Top shows steady-state XAS data for both low-spin [Fe(tren(py)$_3$)]$^{2+}$ (solid line) and [Fe(tren(6-Me-py)$_3$]$^{2+}$ (dashed line) complexes. Fourier Transform of the fine structure (EXAFS) in the spectra of Figure 3-5 Top yields information on the average bond distance of the Fe-N bonds. As shown in Figure 3-5 Bottom, the high-spin analogue (open squares) has a 0.25 Å longer Fe-N bond distance than the low-spin complex (open circles). This Fe-N elongation represents an approximate 10% change in the bond distance, which is a significantly large change from the low-spin structure. Similar results have been reported for iron(II) spin-crossover compounds.[14, 15]

The main spectral features in Figure 3-5 Top, A(A') and B(B'), arise from electron transitions to the lowest unoccupied metal states. Noticeably, the intensity of the shoulder labeled A at 7124 eV increases from the low-spin complex to the high-spin complex, which is attributed to an increase in metal character of the Fe(4p) orbital being a consequence of the increasing Fe-N bond distance and a concomitant decrease in the interaction between the metal atom and ligand orbitals. The main resonance of the spectrum, B(B'), shifts to lower energies from B (7131 eV) to B' (7128 eV) when moving from the low-spin complex to the high-spin complex. This shift is attributed to the difference in the energies of the Fe(4s,4p)-N(2p) orbitals in the low-spin and high-spin complexes. Elongation of the Fe-N bond decreases the interaction of the Fe and N atoms and lowers the unoccupied Fe(4s,4p)-N(2p) orbitals shifting B to lower energy by ~2.5 eV.

The shoulder C (7142 eV), loses intensity and the broad feature D (~7198 eV) shifts to lower energy D' (7174 eV) when moving from the low-spin complex to the high-spin

60

complex. These changes are attributed to structural differences in the two complexes and agree well with previously published work on iron spin-crossover complexes.[14-18] The shift between D and D' is consistent with the change in the ratio of the average Fe-N bond distances in going from the low-spin to the high-spin complex.[15]
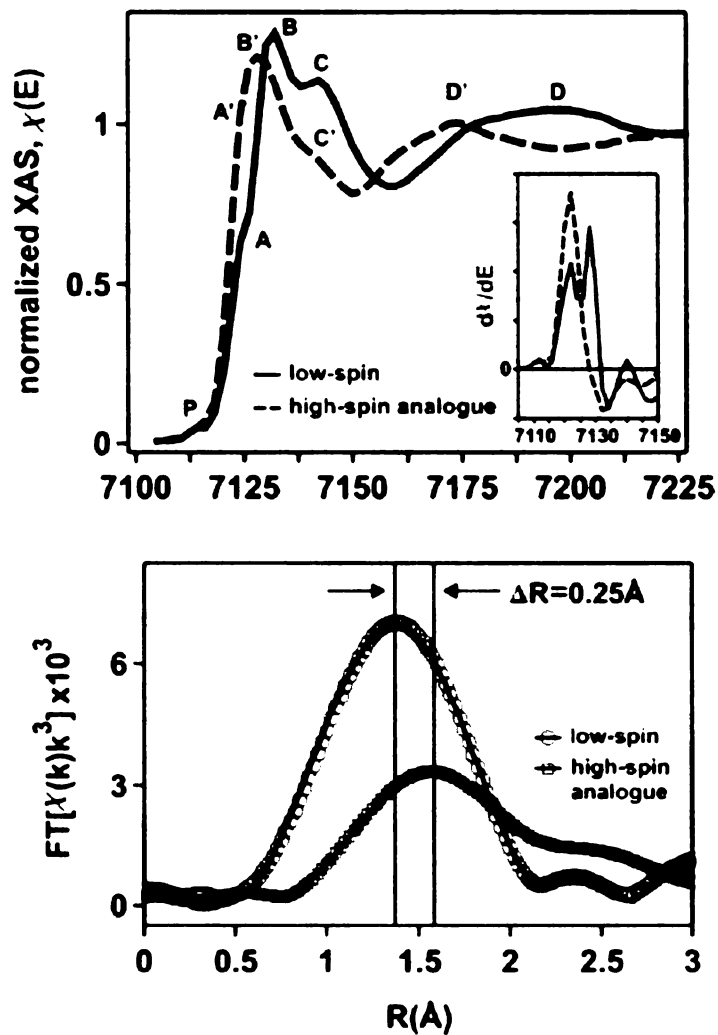
Figure 3-5. Steady-state XAS data at the Fe K-edge for [Fe(tren(py)₃)](PF₆)₂ and [Fe(tren(6-Me-py)₃)](PF₆)₂ in acetonitrile.

Top: The XANES spectra of the low-spin (solid line) and the high-spin analogue (dashed line) plotted with normalized x-ray absorption. The derivatives of the XANES spectra are plotted in the inset to highlight the differences in spectral positions and amplitudes for the two compounds. Bottom: Fourier-transformed XAFS spectra weighed by $(k)^3$. Note that the spectra are not corrected for the phases, so the displayed distances are shorter that the actual distances listed in Table 3-1. Modified from reference 11.

In addition to the main XANES features, there is a weak pre-edge feature P, present in both the spectra at 7114 eV, which is due to the forbidden 1s to 3d transition. Feature P indicates that there is a slight distortion from octahedral in the complex. Since feature P is present in both the low-spin and high-spin complexes we concluded that the amount of distortion from octahedral symmetry is similar in both complexes. The XANES derivative spectra plotted in the inset of Figure 3-5 Top highlights the above differences in the positions and amplitudes of the spectral features.

Transient XAS measurement on the low-spin complex, $[Fe(tren(py)_3]^{2+}$, probes the difference in electron density around the iron at various time delays. Figure 3-6 Top shows a typical spectrum collected at 330 ps after excitation. The top trace in Figure 3-6 Top (open circles) is the transient spectrum collected 330 ps after excitation and the bottom (solid line) is a calculated difference spectrum from the steady-state XANES and EXAFS data. The strong similarities indicate that $[Fe(tren(py)_3]^{2+}$ is in the $^5T_2$ state 330 ps after excitation. In an attempt to determine the timescale for the structural arrival in the $^5T_2$ state a kinetic trace was acquired at 7142 eV. Figure 3-6 Bottom shows the kinetic trace of $[Fe(tren(py)_3)]^{2+}$ at 7142 eV. The temporal evolution of the data in Figure 3-6 Bottom was described as a step function and is fit by a Gaussian error function with a time constant of 70 ± 20 ps. Temporal resolution of the instrumentation is 70 ps rendering the validity of the formation time constant derived from the time resolved XAS measurements is questionable. On the timescale of this experiment the $^5T_2$ state is formed immediately after photoexcitation. Table 3-1 lists the Fe-N bond length data acquired from the steady-state XAS measurements and those derived from the time-resolved measurement. Details on the fitting procedure used to acquire these data has been reported previously.[11]

XAS experiments provide us information on the structural changes associated with excited state evolution of $[Fe(tren(py)_3)]^{2+}$. The main goal of this on going collaboration is to understand how the structure of this iron(II) complex changes as it crosses from the initially excited ^1MLCT state to the long-lived $^5T_2$ state. With the current temporal resolution

Table 3-1. XAS data fitting results.

Complex	Fe - N bond length (R, Å)
[Fe(tren(py)$_3$)](PF$_6$)$_2$	1.94 ± 0.01
[Fe(tren(6-Me-py)$_3$)](PF$_6$)$_2$	2.19 ± 0.01
Δt = 330 ps [Fe(tren(py)$_3$)](PF$_6$)$_2$	2.15 ± 0.03
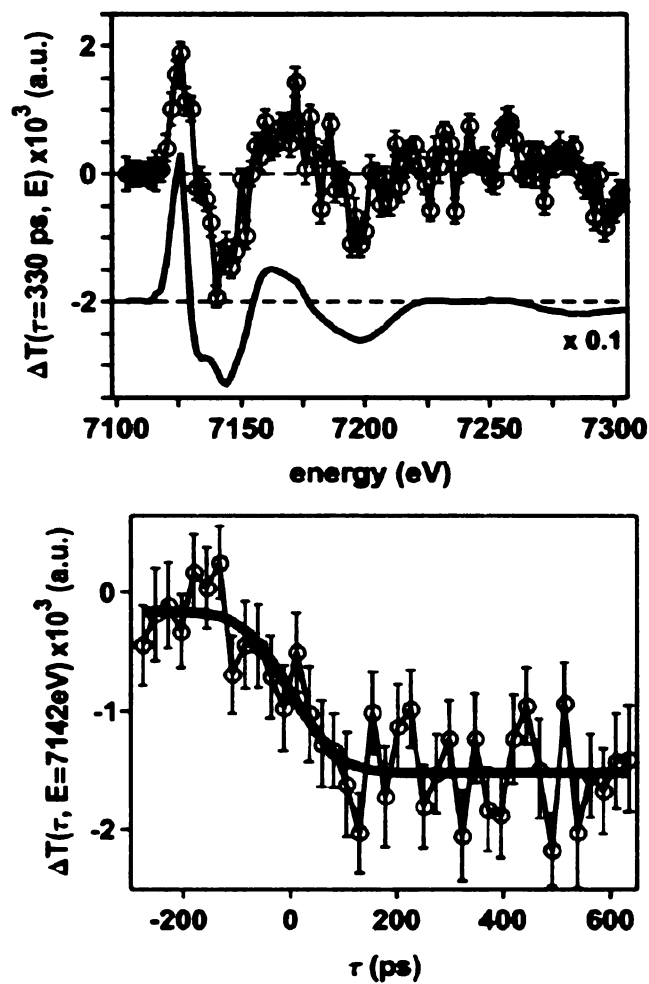
Figure 3-6. Time-resolved XAS difference spectroscopy of Fe[tren(py)$_3$](PF$_6$)$_2$ in acetonitrile.
Top: Transient difference x-ray absorption spectrum recorded 330 ps after excitation (open circles). The difference between the steady-state XAS spectra of the high-spin and low-spin compounds is plotted below as a solid line. Bottom: Transient differential XAS signal at 7142 eV as a function of the delay time. The thick solid line is a fit. Modified from reference 11.

of the XAS apparatus we are not able to observe the ^{1}MLCT to ^{5}T$_2$ conversion; however it provides us further evidence that the long-lived state is formed and thermalized in fewer than 70 ps. Current work at the ALS is focused on achieving faster X-ray pulses so that the next experiments will be able to observe the early time dynamics associated with this conversion to the ^{5}T$_2$ state. Structural information on the ^{1}MLCT to ^{5}T$_2$ conversion is of interest in that this process yields a ΔS=2 transition that must be occurring very rapidly.

Assuming that the ^{1}MLCT state structurally resembles the ^{1}A$_1$ state there is a 10 % dilation of the Fe-N coordination sphere that must occur in less than 100 fs and be completely thermalized in approximately 30 ps to achieve the structure of the ^{5}T$_2$ state. In the likely hood that the ^{5}T$_2$ to ^{1}A$_1$ transitions accurately models the ^{1}MLCT to ^{5}T$_2$ transition an expansion and twist of the facial planes of the complex must occur approximately three orders of magnitude faster than the ^{5}T$_2$ to ^{1}A$_1$. Spin crossover literature has established that the ^{5}T$_2$ state converts to the ^{1}A$_1$ state via a tortional[14] mode of the coordination sphere. Understanding the structural modes associated with the ^{1}MLCT to ^{5}T$_2$ transition would enable more efficient molecular engineering efforts to synthesize iron(II) complexes with longer lived ^{1}MLCT states.

3.3.5 Femtosecond Time-Resolved Spectroscopy.

The main interest of the research presented here lies in determining the lifetime of the charge transfer state. From the absorption spectrum of the low-spin [Fe(tren(py)$_3$)]$^{2+}$ complex we know that excitation into the low-energy feature at 560 nm produces an initially excited ^{1}MLCT state.

As discussed previously the best way to model a charge transfer transition is with spectroelectrochemistry, which provides insight into the absorptive properties of the two halves of the lowest energy charge transfer transition. Spectroelectrochemical data shown in Figure 3-3 the indicates that the ^{1}MLCT state absorbs red of 600 nm, around 420 nm, and in the ultraviolet region. Probing in these regions should yield positive signals that are indicative of population of the ^{1}MLCT state. After excitation of [Fe(tren(py)$_3$)]$^{2+}$ at
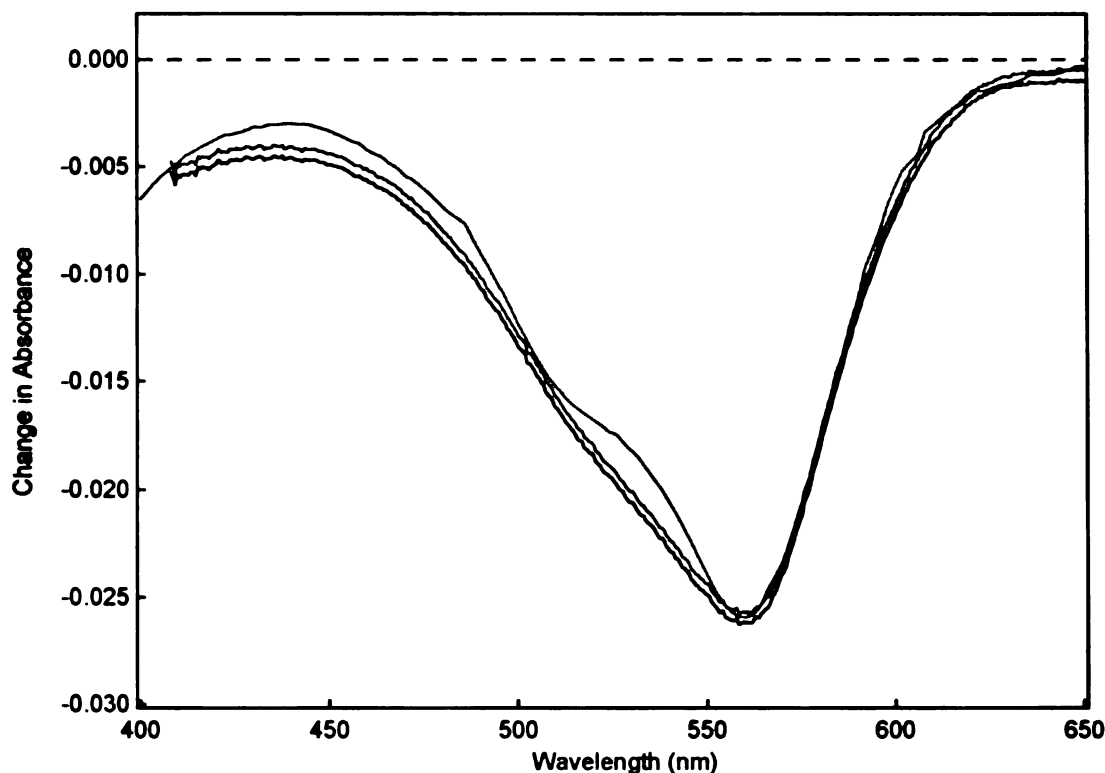
Figure 3-7. Difference spectra of [Fe(tren(py)$_3$)](PF$_6$)$_2$ in acetonitrile.
The calculated difference spectrum (^{5}T$_2$- 1A$_1$) of low-spin complex [Fe(tren(py)$_3$)](PF$_6$)$_2$ is shown as the red line; however, it has been scaled to match the other time resolved data at 560 nm. A full spectrum of [Fe(tren(py)$_3$)](PF$_6$)$_2$ at 5 ps delay is shown by the black trace and a 700 fs delay by the blue trace. The strong correlation between the three spectra indicates that [Fe(tren(py)$_3$)](PF$_6$)$_2$ populates in the ^{5}T$_2$ state faster than 700 fs.

560 nm there is no evidence of the MLCT state as shown in Figure 3-7 which lacks the

desired absorptions of the ^{1}MLCT state at both a 5 ps delay (blue) and at a 700 fs delay

(black). Both time traces match well with the scaled calculated difference spectrum in

red, indicating that the ^{1}MLCT state has deactivated to the ^{5}T$_2$ state in less than 700 fs.

To determine how quickly the ^{1}MLCT state deactivates to the ^{5}T$_2$ state single wavelength

kinetic traces were acquired at various wavelengths. A kinetic trace at 420 nm probe (Figure

3-8) reveals an initial positive signal that decays to a long-lived negative signal. This sign

change is associated with the deactivation of the ^{1}MLCT state to the ^{5}T$_2$ state. Similar

kinetic features were observed by Monat and McCusker in 2000.[1] At 420 nm the reductive

trace in Figure 3-3 shows a positive feature and the nanosecond difference spectrum shows

a negative signal, from this data we can conclude that the initially positive feature is due to
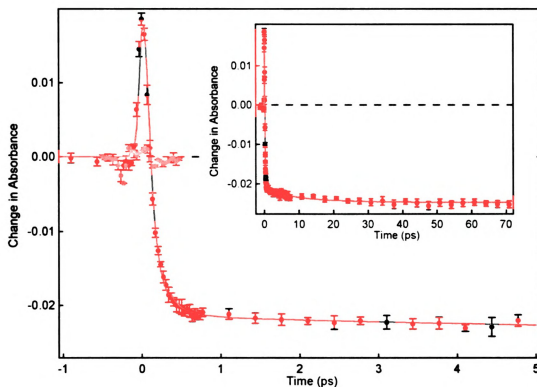
Figure 3-8. Single wavelength kinetic trace of [Fe(tren(py)$_3$)](PF$_6$)$_2$ at 420 nm probe after 560 nm excitation.
A deconvoluted fit is shown in red and yields time constants of: τ_1 = 70 ± 30 fs; τ_2 = 180 ± 20 fs ; τ_3 = 10 ± 2 ps.

the ^{1}MLCT state and the long-lived negative signal to the $^5T_2$ state.

A deconvolution program was used to fit the kinetic data and the time constants associated with the excited state dynamics were fit to an exponential function, the kinetic data and the corresponding deconvolved fit are displayed in Figure 3-8. Using a triexponential function convolved with a Gaussing function, the time constant associated with the deactivation of the ^{1}MLCT state was found to be 70 ± 20 fs. A second longer component attributed to vibrational cooling a was fit to 10 ± 2 ps, while a third component with a 180 ± 20 fs time constant was needed to achieve the best fit, although its origins are unclear. Some research suggest this is a librational mode of the solvent; however, the data provided in this paper are inconclusive to that end.[19, 20]

Fitting the same kinetic trace to a convolved biexponential fit with a 70 ps component and an 8 ps vibrational cooling time. However, the data around 100-200 fs was not fit well
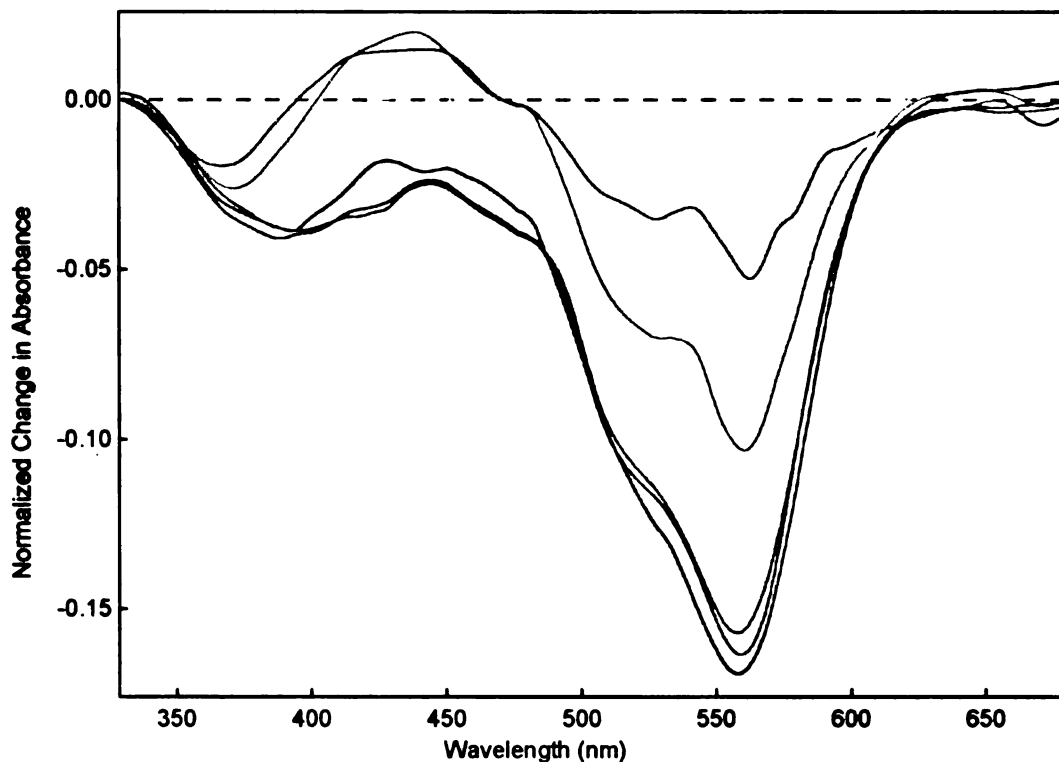
Figure 3-9. Chirp-corrected full spectral data for [Fe(tren(py)₃)](PF₆)₂ using a CaF₂ generated continuum. Time delays of 0 ps (---), 0.1 ps ( ), 0.2 ps( ), 0.3 ps(—), 0.5 ps(--), and 1 ps (—) are shown.

with the biexponential function, therefore the triexponential function was used. Monat reported a biexponential fit of t_1=80 fs and t_2=8 ps, which agrees well with our results. Since the ¹MLCT state deactivates to the $^5T_2$ state with a time constant less than 100 fs, spectral resolution of the dynamics associated with the ¹MLCT state will occur in the first picosecond after excitation. Full spectral data will provide a more complete picture of the kinetic processes in the excited state manifold of [Fe(tren(py)₃)]²⁺. Chirp-corrected full spectral data of [Fe(tren(py)₃)]²⁺ in acetonitrile is presented in Figure 3-9 show the spectral evolution that occurs in the first picosecond after 560 nm excitation of [Fe(tren(py)₃)]²⁺ in acetonitrile. Initially positive features around 420 nm and red of 600 nm indicate the presence of the ¹MLCT state and they rapidly deactivate to a negative signal. This rapid spectral evolution is exactly what the single wavelength kinetic traces indicate for the ¹MLCT to $^5T_2$.

Despite the ability of CaF₂ to generate a continuum of white light ranging from 330
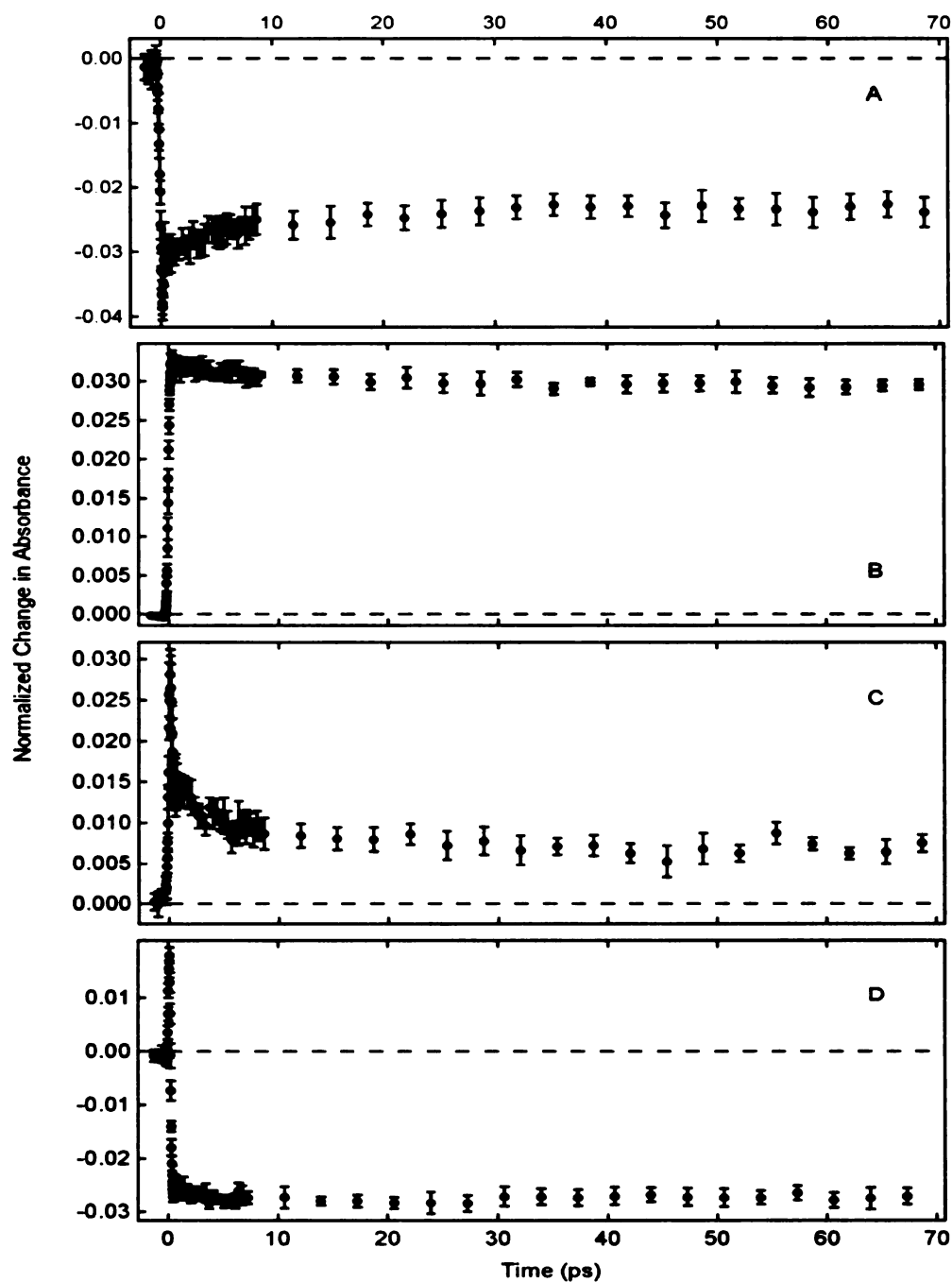
Figure 3-10. UV single wavelength kinetic data of $[Fe(tren(py)_3)](PF_6)_2$ in acetonitrile after 560 nm excitation.

All kinetic trace are normalized at 50 ps to the corresponding A_0 value from nanosecond transient absorption measurements. A: 285 nm probe. B: 290 nm probe. C: 325 nm probe. D: 330 nm probe

nm to 900 nm, the absorptive features in the ultraviolet region are no accessible without changing the nature of the probe source. Implementation of a second optical parametric amplifier (TOPAS 2) as a probe source provided access to wavelengths blue of 330 nm. Single wavelength kinetic traces were acquired by tuning TOPAS 2 to a desired wavelength and collecting a kinetic trace. Each trace was then normalized at a 50 ps delay to the values obtained from the nanosecond transient absorption data. Normalization of the UV traces was essential to accurately compare the difference between wavelengths, since the pump-probe cross section at each probe wavelength was not constant. Figure 3-10 shows several normalized single wavelength traces of interest; 285 nm(A) and 290 nm(B), being close to the blue isosbestic and 325 nm(C) and 330 nm(D), being close to the red isosbestic. Isosbestics are points where the ground state and the long-lived excited state have the same absorbance, effectively producing a difference signal equal to zero. Kinetic traces at an isosbestic provide information on the absorptive properties of any electronic state that is not the ground or long-lived excited state, in the scope of this study this would include the ^1MLCT state or a higher-energy ligand field state. In comparison to the CaF_2 continuum generation, the TOPAS output is considered to be monochromatic; however, ultrafast pulses require some amount of spectral bandwidth. The presence of this spectral bandwidth in the probe beam provides one explanation as to the presence of the signals observed for the kinetic traces in Figure 3-10A-D. Despite the residual signals in the kinetic traces around the isosbestic a rapidly decaying feature was still observable. The lower energy isosbestic (~328 nm) is less sharp than the higher energy isosbestic, therefore we are more likely to isolate contributions from the ^1MLCT state in this region. To more accurately probe the isosbestic a more reliable means of calibrating the output form TOPAS 2 needs to be developed.

Compilation of all the normalized single wavelength traces enabled the constructing of time-dependent full spectra in the ultraviolet region. The UV spectrum was then plotted with the spectra acquired with the CaF_2 continuum to generate a complete spectrum. As
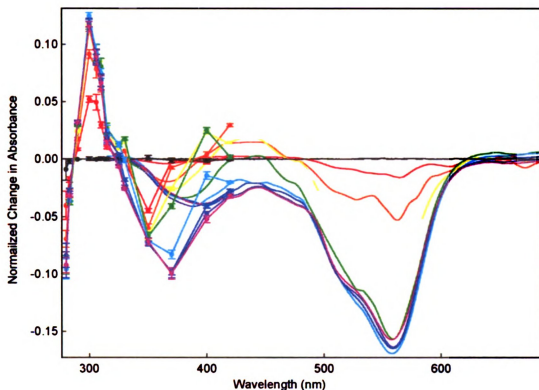
Figure 3-11. Full spectral analysis of [Fe(tren(py)₃)](PF₆)₂ in acetonitrile.
Chirp-corrected full spectra and UV time resolved transient absorption data at 0 ps(—), 0.05 ps(—), 0.1 ps( ), 0.2 ps(—), 0.3 ps( ), 0.4 ps(—), 0.5 ps(—) and 1 ps(—) are shown.

shown in Figure 3-11, the rapid deactivation of the initially formed ^{1}MLCT state is striking. The agreement between the two independently collected spectra was fair. The most noticeable deviation between the two spectra occurs in the blue region of the spectrum, <350 nm. This discrepancy is most likely due to the decreasing probe intensity from the continuum from 390 nm and the strong ground state absorptions of the complex this region. The amplitude of the transient signal is dependent on a few factors 1) the pump-probe cross section (amount of excited state produced), 2) the strength of the excited state signal, and 3) the intensity of the probe beam. If the intensity of the probe is low in a specific region and the molecule has strong ground state absorptions in the same the signal-to-noise ratio is greatly reduced, since detecting a small change on top of a small signal is difficult. This is the case for the ~350 nm region of the full spectral data collected with the continuum, therefore the discrepancy between the two spectra is insignificant.

No spectral shifting is observed on the one-picosecond time scale, uniform ultrafast decay from the ^{1}MLCT state to the ^{5}T$_2$ state is the only noticeable feature. If spectral shifting was observed it would indicate that a state other than the ^{5}T$_2$ state was populated
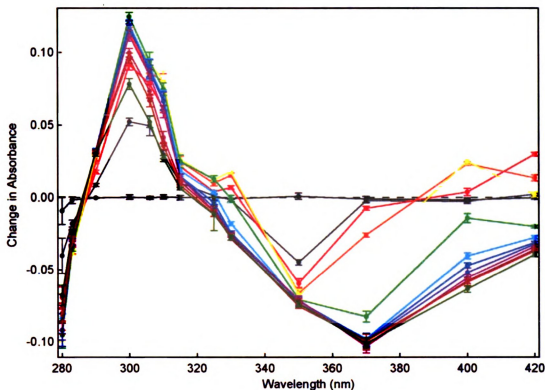
Figure 3-12. Vibrational cooling of [Fe(tren(py)$_3$)]$^{2+}$ in acetonitrile in the UV region after 560 nm excitation
UV time resolved transient absorption data at -1 ps (—), -0.1 ps ( ), 0 ps(—), 0.05 ps(—), 0.1 ps( ), 0.2 ps(—), 0.3 ps( ), 0.4 ps(—), 0.5 ps(—), 1 ps( ), 5 ps(—),10 ps(—) and 50 ps(—) are shown.

for a significant amount of time during the decay of the ^{1}MLCT state to the long-lived ^{5}T$_2$ state. The lack of spectral shifting indicates that it is unlikely that any other state between the ^{1}MLCT and ^{5}T$_2$ states is populated upon the deactivation of the ^{1}MLCT state. The lack of spectral shifting also supports the assignment of the long time component to vibrational cooling. Monat and McCusker previously reported that in the visible after 1 ps the only observed dynamic is vibrational cooling on the ^{5}T$_2$ surface.[1] Figure 3-12 shows results reminiscent of vibrational cooling in time slices from 0 to 50 ps, in that vibrational cooling narrows spectral features as seen in Figure 3-12.

Table 3-2. Pump wavelength dependence on vibrational cooling of [Fe(tren(py)$_3$)](PF$_6$)$_2$ in acetonitrile

Wavelength	Probe 330 nm	Probe 400 nm	Probe 420 nm	Probe 510 nm	Probe 530 nm
560 nm	2 ± 1 ps	15 ± 2 ps	13 ± 3 ps	19 ± 3 ps	26 ± 5 ps
570 nm	3 ± 1 ps	19 ± 5 ps	16 ± 3 ps	13 ± 2 ps	18 ± 3 ps
580 nm	2 ± 2 ps	14 ± 3 ps	22 ± 7 ps	21 ± 3 ps	22 ± 3 ps

A variable pump wavelength study was undertaken by monitoring several probe wavelengths and changing the amount of energy put into the system systematically by varying the pump wavelength. The time needed to vibrationally dissipate the different amounts of excess energy should change accordingly. This is valid if the intersystem crossing event happens prior to relaxation on the initially excited Frank-Condon ^{1}MLCT
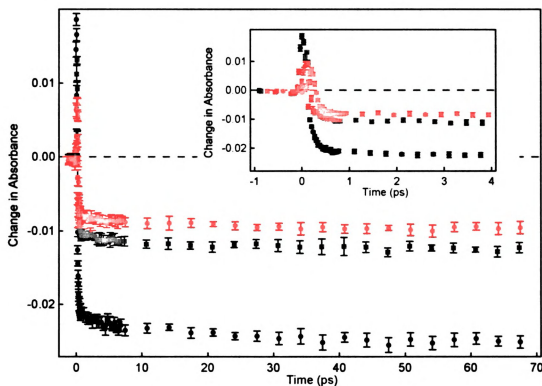
Figure 3-13. Pump wavelength dependence of vibrational cooling of [Fe(tren(py)$_3$)](PF$_6$)$_2$ in acetonitrile at 420 nm probe
Black: 560 nm pump, Red: 570 nm pump, Blue: 580 nm pump.

surface. If the system first relaxes on the ^{1}MLCT surface then crosses to the ligand field manifold little to no change in the long-time component will be observed. Table 3-2 presents the value of the long-time component for the three different pump energies. Figure 3-13 shows the corresponding variable pump wavelength kinetic traces at 420 nm probe. Little to no systematic variation is observed for the three different pump wavelengths, indicating that some cooling may take place on the ^{1}MLCT state prior to intersystem crossing to the ligand field manifold. Coincidentally, for each pump wavelength a systematic trend is observed for the probe wavelengths presented in Table 3-2. As the probe wavelength is tuned to the red the long-time component increases, which is also expected when probing a vibrational cooling process. The larger density of vibrational states at the top of a potential energy surface readily facilitates the rapid cooling of the vibrationally hot complex to the lower vibrational levels. Higher energy probes are only monitoring the population in the upper vibrational levels, the time constant at these wavelength is relatively short since the molecule is cooling rapidly to the lower vibrational levels. In the case of the lower energy probe wavelength the density of states is less lower on the potential energy surface, which slows the cooling process and results in longer lifetimes. With the full spectral data and the trend in the probe wavelengths the assignment of the long-time component as vibrational cooling is reasonable. Experiments that directly probe the vibrational modes of $[Fe(tren(py)_3)]^{2+}$ will be more diagnostic, and preparations are currently being made to begin those measurements.

3.4 Conclusions

Ultrafast decay of the initially excited ^{1}MLCT state of a low-spin iron(II) polypyridyl complex was observed at various pump wavelengths. The lifetime of the ^{1}MLCT state was consistently less than 100 fs, which is comparable to the temporal resolution of the instrumentation. The availability of ultraviolet probe wavelengths provided a unique view of the long-lived excited state and its subsequent population after deactivation of the ^{1}MLCT state. Little to no spectral shifting is observed in the UV or visible region of

73

the transient spectrum indicating the ^{1}MLCT deactivates rapidly to the $^5T_2$ state without populating any other state for any appreciable amount of time. Due to the large number of ligand field states that lie below the ^{1}MLCT state it is reasonable to conclude that the other ligand field states act as a continuum to facilitate the deactivation of the ^{1}MLCT state. The long-time component observed in the kinetic traces is ascribed to vibrational cooling on the $^5T_2$ surface.

Identification of a time constant associated with the short-lived ^{1}MLCT state of ~100 fs indicates that any reactivity of ^{1}MLCT state of the iron(II) complex is most likely short lived. This lack of excited state reactivity may explain previous work on an iron(II)-based sensitizer for a TiO_2-based solar cell, where the sensitizer was able to produce a photocurrent although significantly small in comparison to an analogous ruthenium(II) sensitizer.[21] The small photocurrent obtained with the iron(II)-based sensitizer may be due to the significantly short lifetime of the iron(II) charge transfer state (~100 fs) in comparison to the approximately the charge transfer state of a similar ruthenium(II)-based sensitizer, N3, (~5 ns).[22] Since a photocurrent was observed for the iron(II)-based sensitizer injection must be occurring and the ^{1}MLCT state of iron(II) complexes is most likely the injecting state since it is the only state with the energy and electronic coupling to facilitate electron injection. The ultrafast lifetime of the ^{1}MLCT state makes iron(II) complexes an ideal sensitizer for studying "hot" injection, meaning electron injection that is occurring from the initially formed state of the sensitizer, since the "cold" state of the iron(II) sensitizer is centered on the metal (ligand field in nature) and most likely lies below the conduction band of TiO_2. Hot injection is beneficial, in that all of the energy put into the sensitizer is harnessed to do work, not lost to intermolecular processes. However ideal iron(II) complexes may be for "hot" injection, the lifetime of their ^{1}MLCT excited state is still too short to enable a significant number of electrons to be injected significantly limiting the photocurrent associated with iron(II)-based sensitizers.

Attempts are being made to further understand that structural dynamics associated

with the deactivation of the initially formed ^{1}MLCT state. Once the pathway of deactivation is identified molecular engineering efforts can focus on attempting to extend the lifetime of the ^{1}MLCT state by modification or functionalizations of the ligand set. Continued collaborations with a research group at Lawrence Berkeley Livermore National Lab and the Miller group at the University of Toronto are working toward uncovering the structural mechanism of the ^{1}MLCT to $^5T_2$ conversion, while a collaboration with the Mathies research group at University of California, Berkeley, is working on utilizing ultrafast Raman to isolate specific modes associated with the same ^{1}MLCT to $^5T_2$ conversion. Hopefully these ventures will prove fruitful and thus enable us to better understand what allows such a rapid deactivation.

3.5 References

1.   Monat, J. E.; McCusker, J. K. *J. Am. Chem. Soc.* **2000**, *122*, 4092-4097.

2.   Creutz, C.; Chou, M.; Netzel, T. L.; Okumura, M.; Sutin, N. *J. Am. Chem. Soc.* **1980**, *102*, 1309-19.

3.   McCusker, J. K.; Walda, K. N.; Dunn, R. C.; Simon, J. D.; Magde, D.; Hendrickson, D. N. *J. Am. Chem. Soc.* **1993**, *115*, 298-307.

4.   McCusker, J. K.; Walda, K. N.; Dunn, R. C.; Simon, J. D.; Magde, D.; Hendrickson, D. N. *J. Am. Chem. Soc.* **1992**, *114*, 6919-6920.

5.   Jonassen, H. B.; Strickland, G. T. *J. Am. Chem. Soc.* **1958**, *80*, 312-318.

6.   Chang, H.-R.; McCusker, J. K.; Toftlund, H.; Wilson, S. R.; Trautwein, A. X.; Winkler, H.; Hendrickson, D. N. *J. Am. Chem. Soc.* **1990**, *112*, 6814-6827.

7.   Hoselton, M. A.; Wilson, L. J.; Drago, R. S. *J. Am. Chem. Soc.* **1975**, *97*, 1772-1729.

8.   Conti, A. J.; Xie, C. L.; Hendrickson, D. N. *J. Am. Chem. Soc.* **1989**, *111*, 1171.

9.   Juban, E. A.; McCusker, J. K. *J. Am. Chem. Soc.* **2005**, *127*, 6857-6865.

10.   Marcus, M. A.; MacDowell, A. A.; Celestre, R.; Manceau, A.; Miller, T.; Padmore, H. A.; Sublett, R. E. *J. Synchrotron Radiat.* **2004**, *11*, 239.

11.   Khaili, M.; Marcus, M. A.; Smeigh, A. L.; McCusker, J. K.; Chong, H. H.; Schoenlein, R. W. *J. Phys. Chem. A* **2006**, *110*, 38-44.

12.   Juban, E. A. Ultrafast Dynamics of Chromium(III) Coordination Compounds. University of California, Berkeley, 2006.

13.   Mahon, C.; Renoylds, W. *Inorg. Chem.* **1967**, *6*, 1927-1928.

14.   McCusker, J. K.; Rheingold, A. L.; Hendrickson, D. N. *Inorg. Chem.* **1996**, *35*, 2100-2112.

15.   Chen, L. X.; Wang, Z. Y.; Burdett, J. K.; Montano, P. A.; Norris, J. R. *J. Phys. Chem.* **1995**, *99*, 7958-7964.

16.   Toftlund, H.; McGarvey, J. J., Iron(II) Spin Crossover Systems with Multidentate Ligands. In *Spin Crossover in Transition Metal Compounds I*, 2004; Vol. 233, pp 151-166.

17. Brady, C.; McGarvey, J. J.; McCusker, J. K.; Toftlund, H.; Hendrickson, D. N., Time-resolved relaxation studies of spin crossover systems in solution. In *Spin Crossover in Transition Metal Compounds III*, 2004; Vol. 235, pp 1-22.

18. Hauser, A. *Coord. Chem. Rev.* **1991**, *111*, 275-290.

19. Ladanyi, B. M.; Stratt, R. M. *J. Phys. Chem.* **1995**, *99*, 2502-2511.

20. Roy, S.; Bagchi, B. *J. Chem. Phys.* **1993**, *99*, 9938-9943.

21. Gregg, B.; Ferrere, S. *J. Am. Chem. Soc.* **1998**, *120*, 843.

22. Tachinana, Y.; Moser, J. E.; Grätzel, M.; Klug, D. R.; Durrant, J. R. *J. Phys. Chem. B* **1996**, *100*, 20056-20062.

Chapter 4. Charge Transfer Dynamics Associated with Iron(II) Polypyridyl Complexes.

4.1 Introduction

Building on previous studies of excited state dynamics of transition metal complexes, specifically Sutin and coworkers 1980 report on the ground state recovery dynamics of a similar series of iron(II) complexes[1], we probe the a series of iron(II) complexes monitoring their behavior on the ultrafast timescale. Excitation in to the low energy ^{1}MLCT feature of the above molecules will enable us to probe the dynamics of the excited complexes without the complicating possibility of directly exciting ligand transitions, which would be the case if we excited into higher energy transitions ($\lambda_{ex} < 400$ nm). Upon excitation, we will initially populate the ^{1}MLCT in a spin-allowed transition from the $^1A_1$ ground state, thus enabling us to monitor the deactivation of the initially excited state and the subsequent dynamics associated with forming the long-lived excited state of these complexes.

4.2 Materials and Methods

All reagents were used as received from commercial sources unless otherwise noted. Elemental analysis was done at the analytical facilities here at Michigan State University.

4.2.1 Synthesis

Iron(II) complexes were synthesized as described below. Ruthenium(II) and osmium(II) complexes were already in hand.

$FeCl_2 \cdot 2H_2O$. Due to the large concentration of iron(III) in commercially available iron(II) dichloride, further purification was done using previously reported methods that achieve the $FeCl_2 \cdot 2H_2O$ used to synthesize the iron(II) complexes in this study.[2] Briefly, 10 g (0.05 mol) of commercially acquired $FeCl_2 \cdot 4H_2O$ and 0.42 g (7.5 mmol) of Fe^0 were placed in a 250 mL round bottom flask containing 50 mL of distilled water. The solution was brought to reflux under Ar for five minutes. After five minutes, 2 mL of 12 M HCl

were added to the solution and the mixture continued to reflux under N_2 for half an hour. During this time, the solution changed from an orange-brown colored opaque solution to a slightly cloudy pale green-blue solution. Still maintaining an inert atmosphere the solution was filtered and the water removed by vacuum distillation. The pale blue-white product was isolated and stored under inert conditions until needed.

[Fe(L)$_n$](PF$_6$)$_2$. Depending on the desired complex, 2 to 3 equivalents of ligand was dissolved in 20 mL of a 1:1 methanol:water solution. The ligand solution was deaerated by bubbling N_2 through a stirring solution for approximately 30 minutes. Once deareated, the ligand solution was transferred to a round bottom flask charged with 1 equivalent of FeCl$_2$•2H$_2$O. A deep red- purple color formed immediately upon addition of the ligand solution to the iron. The solution was allowed to stir for and additional 2 hours to ensure complete reaction of the Fe(II) with the ligand, at which point a 10 fold excess of NH$_4$PF$_6$ was added to the solution as a methanol:water mixture. Immediately, an intensely colored precipitate formed that was recovered by filtration and recrystallized by dissolution in a hot 1:1 methanol:water solution. Subsequent slow cooling of the hot methanol:water solution yielded microcrystalline solids of the molecule interest.

[Fe(bpy)$_3$](PF$_6$)$_2$. Where bpy is 2,2'-bipyridine and forms a deep red solution when bound to iron(II). Elemental Analysis: Calculated (C$_{30}$H$_{24}$N$_6$FeP$_2$F$_{12}$) C 44.25%, N 10.32%, H 2.97%; Found C 44.18%, N 9.92%, H 2.69%. UV-Vis in CH$_3$CN $\lambda(\varepsilon)$: 248 (17 000), 298 (40 000), 352 (4 100), 480 (4 500), 524 (5 400).

[Fe(dmb)$_3$](PF$_6$)$_2$. Where dmb is 2,2'-bipyridine-4,4'-dimethyl and forms a deep brick red solution when bound to iron(II). Elemental Analysis: Calculated (C$_{36}$H$_{36}$N$_6$FeP$_2$F$_{12}$Na$_{0.4}$Cl$_{0.4}$) C 46.90%, N 9.11%, H 3.95%; Found C 47.22%, N 9.07%, H 3.86%. UV-Vis CH$_3$CN $\lambda(\varepsilon)$: 216 (9 300), 254 (21 000), 360 (8 600), 494 (9 300), 539 (9 400).

[Fe(phen)$_3$](PF$_6$)$_2$. Where phen is 1,10-phenanthroline and forms a deep orange-red solution when bound to iron(II). Elemental Analysis: Calculated (C$_{36}$H$_{24}$N$_6$FeP$_2$F$_{12}$) C 48.78%, N 9.48%, H 2.72%; Found C 48.71%, N 9.60%, H 2.69%. UV-Vis CH$_3$CN $\lambda(\varepsilon)$:

228 (77 000), 266 (87 000), 440 (7 500), 514 (11 000).

[Fe(terpy)$_2$](PF$_6$)$_2$. Where terpy is 2,2':6',2''-terpyridine and forms a deep purple solution when bound to iron(II). Elemental Analysis: Calculated (C$_{30}$H$_{22}$N$_6$FeP$_2$F$_{12}$) C 44.36%, N 10.35%, H 2.73%; Found C 44.34%, N 10.34%, H 2.63%. UV-Vis CH$_3$CN $\lambda(\epsilon)$: 274 (42 000), 320 (52 000), 366 (4 000), 506 (6 000), 550 (11 000), 612 (2 000).

4.2.2 Steady-state electronic absorption spectra

Ground state absorption spectra were collected on an HP8420 diode array spectrometer. All spectra were collected with the desired complex dissolved in HPLC grade acetonitrile at ambient temperature and in aerated solutions. Extinction coefficients are acquired by serial dilution of the acetonitrile solution containing the complex of interest. Spectra at 5 different concentrations were collected and the absorbance versus concentration data, at a given wavelength, was fit to a linear regression, of which the slope was reported as extinction coefficient. Wavelengths chosen were based on corresponding significant spectral features.

4.2.3 Electrochemical and spectroelectrochemical measurements

Electrochemical measurements were carried out with a BAS 100A electrochemical analyzer. Solutions of compounds were dissolved in degassed HPLC grade acetonitrile with 0.1 M Bu$_4$NPF$_6$ as the supporting electrolyte. A standard three-electrode setup was used with a Pt-disk working electrode, a Pt-wire counter electrode, and a Ag/Ag(NO$_3$) reference electrode. All measurements were made in a N$_2$ filled glovebox.

Once the first reduction and oxidation potentials were obtained for each complex spectroelectrochemical measurements were carried out. Again, the desired complex was dissolved in HPLC grade acetonitrile and Bu$_4$NPF$_6$ was added to yield a 0.1 M solution of the supporting electrolyte. The concentration of the desired complex in a typical spectroelectrochemical measurement was 5 x10^{-3} M. Depending on the spectral region of interest the concentrations are varied to enable spectral resolution in that region. Using a Pt-

mesh working-electrode the sample was either oxidized or reduced and difference spectra collected at predetermined time intervals. A fresh sample was used for each reductive and oxidative spectrum.

Spectroelectrochemical measurements provide insight into the absorptive properties of the lowest energy charge transfer state providing an initial guess as where the ^{1}MLCT state will absorb. Thus, we can use the spectroelectrochemical results as a guide to determine where to probe for a spectroscopic handle associated with ^{1}MLCT state.

4.2.4 Ultrafast time-resolved transient absorption spectroscopy

The system used to collect the ultrafast transient absorption data has been reported elsewhere.[3]

Excitation energy was attenuated with neutral density filters and adjusted to a value that ensured a linear molecular response. Pump beam intensities were on the order of 5-6 µJ at wavelengths corresponding to the peak of the low energy metal-to-ligand charge transfer (MLCT) transition for each sample. Linearity was verified for each pump wavelength and sample combination. The optical density of each sample at the excitation wavelength was on the order of 0.6-0.8 in aerated HPLC grade acetonitrile.

Continuum generation was achieved by focusing 805 nm light into a 1 cm thick plate of CaF$_2$ yielding probe wavelengths from 330 nm to 700 nm. Single wavelength kinetic traces were acquired by selecting a small portion of the continuum with 10 nm band-pass filters. Either neat solvent in 1 mm path length quartz cuvettes or a two-photon absorber, such as trichlorotoluene in acetonitrile, were used to establish $\Delta t = 0$.

Early time spectra were corrected for temporal chirp by adjusting for $\Delta t=0$ from a solvent trace. The chirp-corrected spectra were also smoothed with an averaging method available in the fitting software.

4.3 Results and Discussion

4.3.1 Steady-state electronic absorption spectra

All complexes are intensely colored and possess transitions in the UV and mid-visible regions of the electromagnetic spectrum.

The molecules of interest are d^6 transition metal polypyridyl complexes of iron, ruthenium, and osmium. Polypyridyl complexes of ruthenium(II) and osmium(II) are all low-spin d^6 complexes (t_{2g}^6) due to the large splitting of the ligand field states attributed to the increased covalency in ruthenium and osmium complexes.[4] The small ligand field splitting in the iron(II) ion mandates that the strength of the coordinated ligand be considered in determining the nature of spin in the ground state. In cases where conjugated substituents are coordinated to the metal center the splitting of the d-states is large enough that the low-spin complex is stabilized. Due to the ability of conjugated ligands to stabilize the low-spin configuration we chose a ligand sets of consisting of polypyridyl type ligands thus generating a series of low-spin complexes that possess the $^1A_1$ ground state.

Figure 4-1 shows the absorption spectra of $[Fe(bpy)_3]^{2+}$, $[Ru(bpy)_3]^{2+}$ and $[Os(bpy)]^{2+}$ in acetonitrile. All three complexes have strong a broad transition in the visible region of the spectrum that is assigned to a metal-to-ligand charge transfer transition (MLCT), from the $^1A_1$ ground state to a ^{1}MLCT state.[5-11] In the case of $[Os(bpy)_3]^{2+}$, there is an additional broad transition red of the ^{1}MLCT band. This broad feature is assigned to a transition from the $^1A_1$ ground state to the ^{3}MLCT state, although the $^1A_1$ to ^{3}MLCT state is a formally a spin forbidden transition the large amount of spin-orbit coupling in third-row transition metals relaxes the spin selection rules allowing the $^1A_1$ to ^{3}MLCT transition.[7] Since neither $[Fe(bpy)_3]^{2+}$ nor $[Ru(bpy)_3]^{2+}$ possess a cleanly accessible ^{3}MLCT transition, we have chosen to focus our study on excitation into the ^{1}MLCT band of all complexes. Excitation into the ^{1}MLCT state will allow us to directly compare the observed dynamics for all complexes of interest.
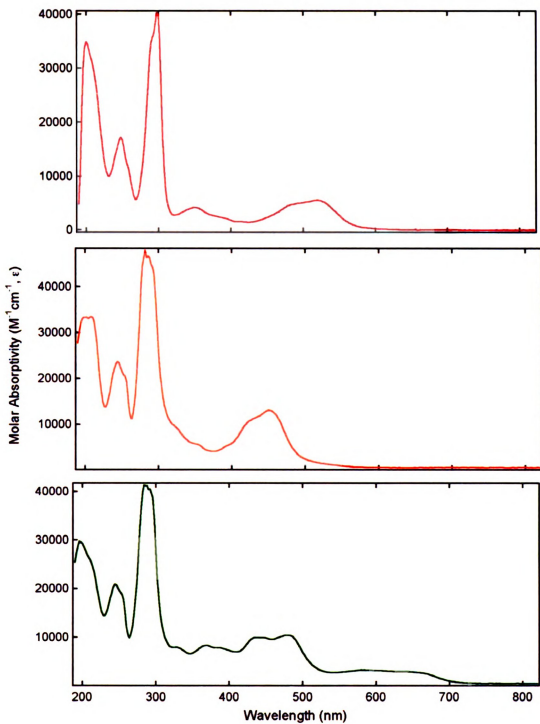
Figure 4-1. Electronic absorption spectra for $[M(bpy)_3]^{2+}$ in acetonitrile M=Fe(II), Ru(II) or Os(II). [Fe(bpy)$_3$](PF$_6$)$_2$ (Top), [Ru(bpy)$_3$](PF$_6$)$_2$ (Middle), and [Os(bpy)$_3$](PF$_6$)$_2$ (Bottom) in acetonitrile.

Due to the significant red shift of this ^{3}MLCT feature osmium complex could be directly excited into its long-lived state, which was not the case for either iron(II) or ruthenium(II) complexes. Papanikolas and coworkers report there is a difference in the observed dynamics of $[Os(bpy)_3]^{2+}$ when the excitation wavelength is tuned from excitation into the ^{1}MLCT to excitation into the ^{3}MLCT state.[12, 13]

In the ground state absorption spectra of $[Fe(bpy)_3]^{2+}$, $[Fe(dmb)_3]^{2+}$ and $[Fe(phen)_3]^{2+}$ the lowest energy feature is a broad feature that maximizes around 530 nm, 540 nm and 520 nm respectively (Figure 4-2A-C). Assignment of some of these transitions have been reported previously.[5-11, 14-17] The breadth of these features and their corresponding extinction coefficients indicate that the transitions are ^{1}MLCT in nature, similar to $[Ru(bpy)_3]^{2+}$ and $[Os(bpy)_3]^{2+}$.

$[Fe(terpy)_2]^{2+}$ possesses a similar broad feature centered around 560 nm; however, there is a uniquely sharp feature overlaid with the broad feature (Figure 4-2D). This relatively sharp feature is typical of $[M(terpy)_2]^{n+}$ transitions and is explained as a result of the ability of a terpyridine ligand to delocalize the electron over its three rings.[18, 19]

Excitation in to the low-energy ^{1}MLCT feature of the above molecules will initially populate the ^{1}MLCT in a spin allowed transition from the $^1A_1$ ground state. By exciting at the low energy MLCT band we ensure population of the ^{1}MLCT state with out the complicating factor of exciting ligand based transitions. Population of the ^{1}MLCT state will enable us to monitor the deactivation of the initially formed excited state and the subsequent dynamics associated with forming the long-lived excited state of these complexes.

4.3.2 Spectroelectrochemical measurements

Metal-to-ligand charge transfer transitions can be thought of as a simultaneous one electron oxidation of the metal center and one electron reduction of the ligand. Experimentally, this is achieved by acquiring spectra of singly reduced and oxidized samples of the complex of interest. By comparing the two traces we gain insight into the absorptive properties of the lowest energy charge transfer transition. The reductive trace reveals the
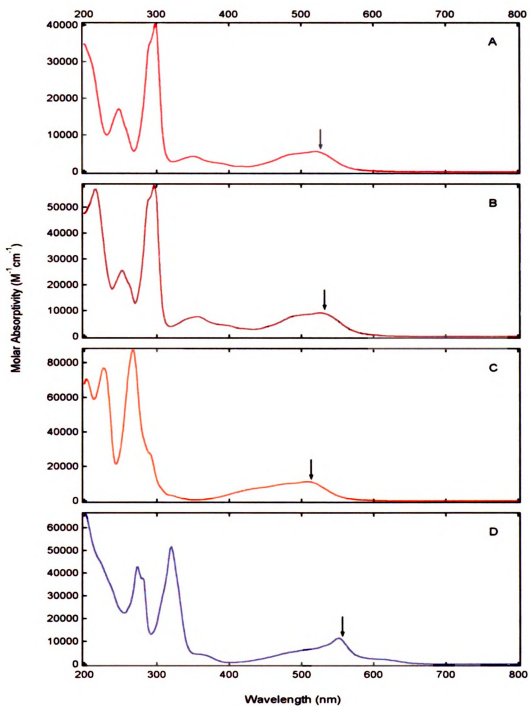
Figure 4-2. Absoprtion spectra of $[Fe(L)_n]^{2+}$ in acetonitrile.
A) L = 2,2'-bipyridine and n = 3, $[Fe(bpy)_3]^{2+}$; B) L = 2,2'-bipyridine-4,4'-dimethyl and n = 3, $[Fe(dmb)_3]^{2+}$; C) L = 1,10-phenanthroline and n = 3, $[Fe(phen)_3]^{2+}$; D) L = 2,2':6',2''-terpyridine and n = 2, $[Fe(terpy)_2]^{2+}$.

contributions of the reduced ligand to the ^{1}MLCT state and the oxidative trace reveals the contribution of the oxidized metal center. Spectra acquired in spectroelectrochemical measurements are often reported as difference spectra, which enables identification of regions where the electrochemically produced species absorbs more than (positive signal) or less than (negative signal) the ground state.

Spectroelectrochemical data for $[Fe(bpy)_3]^{2+}$, $[Ru(bpy)_3]^{2+}$, and $[Os(bpy)_3]^{2+}$ are presented in Figure 4-3, in which, red traces correspond to the reduced species and blue traces correspond to the oxidized species. In the reductive traces, of all three complexes exhibit positive features (absorptions) around 370 nm corresponding to the radical anion of a bipyridine ligand and red of 600 nm corresponding to an overtone of the same transition. [20] Oxidation of the complexes yield an absorptive feature red of 600 nm, which corresponds to a ligand-to-metal transition from a neutral bipyridine ligand to the oxidized metal center. The absorptive features identified in the spectroelectrochemical spectra are key in determining when the low-energy charge transfer state is populated. Monitoring time-resolved transient absorption measurements for positive signals in these regions will provide insight into determining if the molecule is in a charge transfer state.

Spectroelectrochemical traces are presented in Figure 4-4A-D for $[Fe(bpy)_3]^{2+}$, $[Fe(dmb)_3]^{2+}$, $[Fe(phen)_3]^{2+}$ and $[Fe(terpy)_2]^{2+}$ respectively. Braterman and coworkers previously reported the reductive spectra of these iron(II) complexes in dimethylformamide (DMF); [17] however, to enable a better comparison between the spectroelectrochemical measurements and our time-resolved measurements we reproduced the spectra in acetonitrile. An additional concern with the data reported in the Braterman paper is the ground state absorption spectra of the iron(II) complexes do not resemble those observed in this study. This deviation is attributed to the fact that commercially available iron(II) chloride has high concentrations of iron(III), which will impact the ground state absorption spectra and the reductive spectra reported by Braterman. Iron(II) chloride used in this study was purified as described above prior to complexation with the desired ligand to
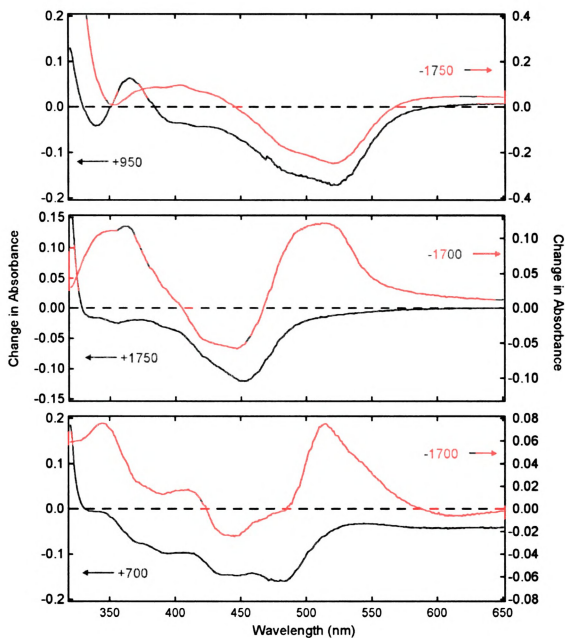
Figure 4-3. Reductive and oxidative spectra of $[Fe(bpy)_3]^{2+}$, $[Ru(bpy)_3]^{2+}$, and $[Os(bpy)_3]^{2+}$. Red traces correspond to the reductive spectrum and the blue traces correspond to the oxidative spectrum. Top: $[Fe(bpy)_3]^{2+}$; Middle: $[Ru(bpy)_3]^{2+}$; Bottom: $[Os(bpy)_3]^{2+}$.
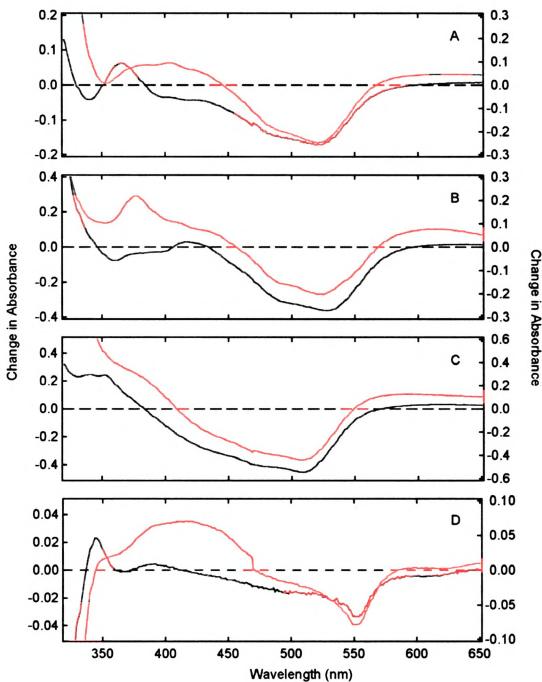
Figure 4-4. Reductive and oxidative spectra for the iron(II) series
Red traces correspond to the reductive spectrum and the blue traces correspond to the oxidative spectrum. A) $[Fe(bpy)_3]^{2+}$; B) $[Fe(dmb)_3]^{2+}$; C) $[Fe(phen)_3]^{2+}$; D) $[Fe(terpy)_2]^{2+}$.

ensure the presence of only iron(II) complexes.

Spectroelectrochemical measurements of $[Fe(bpy)_3]^{2+}$ and $[Fe(dmb)_3]^{2+}$ yield similar results (Figure 4-4A and B). Both sets of spectra show a negative feature around 530 nm, due to the loss of ground state absorption and the lack of strong absorption of the electrochemically generated species. The strong broad absorption in the reductive traces around 400 nm and 600 nm correspond to the formation of the radical anion of the bipyridyl ligand.[20] The slight blue shift of these radical anion transition from $[Fe(bpy)_3]^{2+}$ to $[Fe(dmb)_3]^{2+}$ correlates well to the increase of electron density on the bipyridine ligand when changing from unsubstituted to the $-CH_3$ substituted systems. Due to the electron donating ability of $-CH_3$ at the 4 and 4' positions of the bipyridyl ligand, dmb has a larger electron density that causes transitions to require more energy to occur, thus shifting the feature to the blue. Oxidative spectra of $[Fe(bpy)_3]^{2+}$ and $[Fe(dmb)_3]^{2+}$ emphasize the subtle energetic differences of the two ligands. The weak positive features present in the spectra are indicative of ligand-to-metal charge transfer (LMCT) transitions, where the neutral bipyridyl ligand transfers an electron to the iron(III) center. A small absorption around 400 nm in $[Fe(bpy)_3]^{2+}$ shifts to the red in $[Fe(dmb)_3]^{2+}$, this is consistent with the idea that the $-CH_3$ groups in the 4 and 4' position of the bipyridyl ligand increasing the electron density on the ligand making it easier to transfer the electron to the iron(III) center. The ease of this reduction shifts the transition to lower energy.

Figure 4-4C shows the spectroelectrochemical spectra of $[Fe(phen)_3]^{2+}$. The reductive trace for $[Fe(phen)_3]^{2+}$ exhibits strong absorptions due to the radical anion of a phenanthorline ligand in the blue region (< 400 nm) and to the red (> 550 nm). The oxidative trace shows positive features at wavelengths < 380 nm and > 570 nm. Both traces show a strong negative signal around 520 nm that corresponds to the loss of ground state absorption and a lack of absorbing electrochemically generated species.

Spectroelectrochemical measurements of $[Fe(terpy)_2]^{2+}$ exhibit strong and broad absorptions in the reductive trace shown in Figure 4-4D. These transitions correspond well

to the singlely reduced terpyridine ligand transitions reported by Braterman in 1992.[17] The oxidative spectrum shows two transitions in the blue and one in the red; one blue transition is around 400 nm and the other close to 350 nm, and the weak broad transition in the red occurs beyond 650 nm. The strong bleach at around 560 nm present in both spectra was again due to the loss of ground state absorption and a lack of electrochemical species absorption.

Since spectroelectrochemical measurements model the two halves of the lowest energy charge transfer state these measurements can be used to determine spectral regions that yield charge transfer state information in optical experiments. Therefore, once a molecule is excited it is no longer in its ground state and therefore will exhibit a difference spectrum that resembles an inversion of the ground state absorption spectrum if the excited state dose not absorb more strongly then the ground state. Probing in regions where both reductive and oxidative traces show a negative signal is not as useful as probing in regions where there are positive features in both traces.

For monitoring the lowest energy MLCT excited state in [Fe(bpy)$_3$]$^{2+}$ and [Fe(dmb)$_3$]$^{2+}$ it appears that probing to the red (> 510 nm) and in the 400 nm region will provide the greatest probability for observation of the lowest energy MLCT excited state. Spectroelectrochemical measurements indicate that the ^{1}MLCT of [Fe(phen)$_3$]$^{2+}$ absorbs blue of 390 nm and red of 570 nm while the lowest energy MLCT excited state of [Fe(terpy)$_2$]$^{2+}$ absorb in the blue around 350 nm, 400 nm, and to the red beyond 600 nm. We presume that the optically generated lowest energy MLCT excited state will absorb in similar regions as the electrochemically generated species; however, due to other contributing factors in an optical experiment, such as solvent dynamics, we may not be able to observe the desired spectral feature. Observation of a positive feature in these regions is most likely an indication that the lowest energy MLCT excited state is populated and subsequent determination of the lifetime associated with this charge transfer excited state can be achieved.

4.3.3 Identification of the MLCT state of $[Fe(bpy)_3]^{2+}$ with transient absorption measurements

In a 1980 report by Sutin and coworkers, a key comparison between the long-lived excited states of $[Fe(bpy)_3]^{2+}$, $[Ru(bpy)_3]^{2+}$ and $[Os(bpy)_3]^{2+}$ concluded that the relatively short lived low energy state of $[Fe(bpy)_3]^{2+}$ was of different character than that of $[Ru(bpy)_3]^{2+}$ or $[Os(bpy)_3]^{2+}$. This short lifetime was also found to be insensitive to the nature of the ligand, which is also different from that of $[Ru(bpy)_3]^{2+}$ or $[Os(bpy)_3]^{2+}$. Since both $[Ru(bpy)_3]^{2+}$ and $[Os(bpy)_3]^{2+}$ have been well characterized the nature of their long-lived excited state is well known and identified to be a ^{3}MLCT state for both. This charge transfer state is localized on the ligand system and has a lifetime of ~900 ns for $[Ru(bpy)_3]^{2+}$ and ~5 ns for $[Os(bpy)_3]^{2+}$.[1, 21] Due to the localization of the excited state in the ligand system it is reasonable that the lifetime of the long-lived excited state of ruthenium(II) and osmium(II) complexes be strongly dependent on the ligand. A significant difference in the lifetimes associated with different ligand sets of a series of ruthenium(II) and osmium(II) complexes was reported by Sutin in coworkers in 1980, where they also reported the lack of ligand dependent lifetimes in a similar iron(II) series.[1] Thus the independent nature of the excited state lifetime in the iron(II) complexes indicated that their long-lived excited states were not charge transfer in nature. The long-lived excited state of $[Fe(bpy)_3]^{2+}$ was subsequently identified as being, a metal-centered state which was further classified as a ligand field state either the $^3T_1$ or the $^5T_2$ state.[1] Figure 4-5 provides a comparison of the difference spectra of $[Fe(bpy)_3]^{2+}$, $[Ru(bpy)_3]^{2+}$ and $[Os(bpy)_3]^{2+}$ at a delay of ~10 ps. The strong absorptions around 400 nm and red of 600 nm in both the $[Ru(bpy)_3]^{2+}$ and $[Os(bpy)_3]^{2+}$ traces indicates the presence and persistence of a charge transfer state, as expected from spectroelectrochemical measurements shown in Figure 4-3; however, the absence of these feature in the $[Fe(bpy)_3]^{2+}$ trace indicates that the charge transfer state is not present. As seen in Figure 4-3, both $[Ru(bpy)_3]^{2+}$ and $[Os(bpy)_3]^{2+}$ possess charge transfer features in the blue (<400 nm) and red (>550 nm) regions of the visible spectrum. The
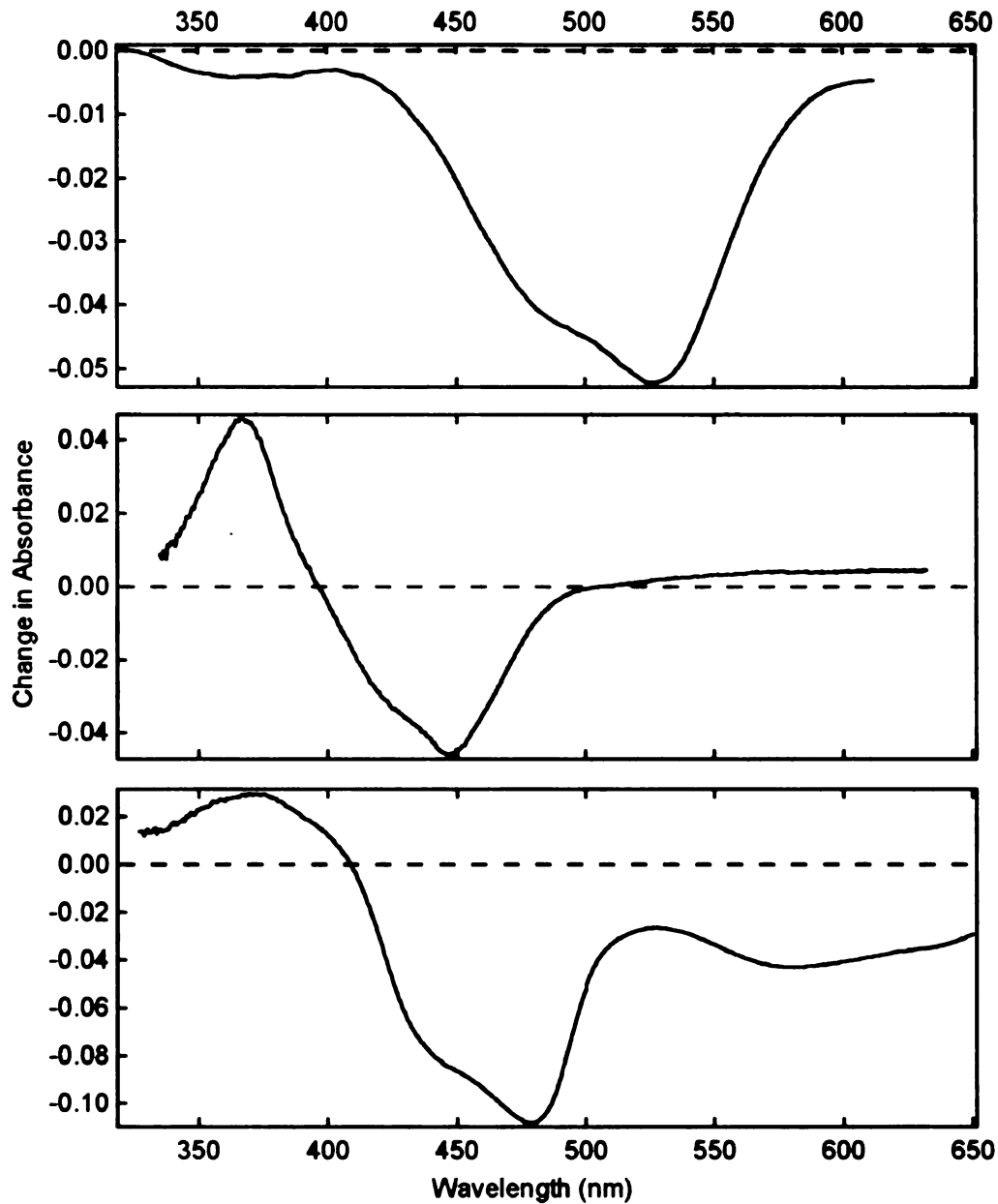
Figure 4-5. Transient absorption spectra of $[Fe(bpy)_3]^{2+}$, $[Ru(bpy)_3]^{2+}$, and $[Os(bpy)_3]^{2+}$

At $\Delta t = 10$ ps after excitation into the respective ^1MLCT states. Top: $[Fe(bpy)_3]^{2+}$; Middle: $[Ru(bpy)_3]^{2+}$;

fact that the difference spectra at a 10 ps delay display similar features as those observed

in the spectroelectrochemical measurements supports the identification of those features

as identifying the presence of a charge transfer long-lived excited state. Characterization

of this long-lived charge transfer state has been reported previously.[12, 13, 21-23] The lack of

positive features in the $[Fe(bpy)_3]^{2+}$ spectrum indicates that the lowest energy excited state

is not charge transfer in nature.

Since both $[Ru(bpy)_3]^{2+}$ and $[Os(bpy)_3]^{2+}$ possess long-lived charge transfer states it is worthwhile to fully characterize and examine the dynamics associated with the formation of this state. Establishing a fundamental understanding of the excited state dynamics of $[Ru(bpy)_3]^{2+}$ and $[Os(bpy)_3]^{2+}$ will provide a useful comparison for interpreting the dynamics associated with the iron(II) species of interest. Chirp-corrected full spectral data for $[Ru(bpy)_3]^{2+}$ and $[Os(bpy)_3]^{2+}$ in three different time windows, from 0 to 1 ps, 1 to 10 ps, and over 100s of picoseconds, are presented in Figure 4-6. Recent reports on the early time dynamics of $[Ru(bpy)_3]^{2+}$ indicate that the long-lived excited state is populated in less then 100 fs[24,26] and the majority of the dynamics are over by 500 fs.[23] Excited state dynamics of $[Os(bpy)_3]^{2+}$ have also been studied, but to a much lesser extent[22,27] and the majority of the ultrafast studies have focused on the polarization dynamics of the excited state manifold not on population dynamics.[12,13,28] The excited state population, magic angle, data available suggests that there is an interligand electron transfer event that occurs with a 10 ps lifetime.[12,13]

Comparison of the chirp-corrected full spectral data in Figure 4-6 provides insight into the differences of the excited state dynamics of $[Ru(bpy)_3]^{2+}$ and $[Os(bpy)_3]^{2+}$. The $[Ru(bpy)_3]^{2+}$ spectra correlate well to the previously reported spectra with very little spectral evolution after excitation into the ^1MLCT state as seen in the right column of Figure 4-6. The sharp peak at ~ 450 nm is laser scatter, and should not be considered when looking for spectral shifting in $[Ru(bpy)_3]^{2+}$. $[Os(bpy)_3]^{2+}$ shows considerable spectral evolution on the picosecond timescale after excitation into its ^1MLCT state as shown in the left column of Figure 4-6. The spectral evolution of $[Os(bpy)_3]^{2+}$ beyond 1 ps has been previously reported by Papanikolas and coworkers and is attributed to an interligand electron transfer process in concert with a significant amount of solvent relaxation.[13] The spectral evolution from 0 ps to 1 ps has not been reported. An initial red shift of the spectrum is most likely due to the intersystem crossing process from the ^1MLCT state to the ^3MLCT state. Excitation
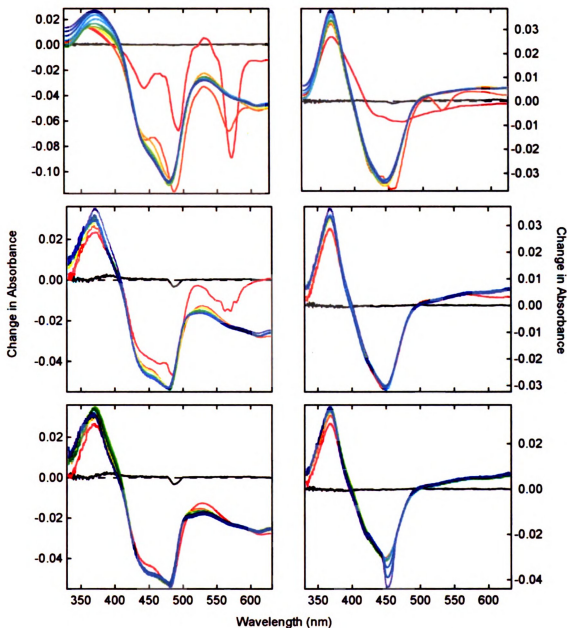
Figure 4-6. Full spectra of $[Os(bpy)_3]^{2+}$ and $[Ru(bpy)_3]^{2+}$ in acetonitrile after ^{1}MLCT excitation. Left: $[Os(bpy)_3]^{2+}$ Right: $[Ru(bpy)_3]^{2+}$ In time intervals of Top panel (0-1 ps): 0 ps(–), 0.1 ps(–), 0.2 ps( ), 0.3 ps( ), 0.4 ps( ), 0.5 ps(–), 0.6 ps(–), 0.8 ps( ), 0.9 ps(–), 1 ps(–), 1.2 ps (–) Middle panel (0.5-10 ps): 0.5 ps(–), 1 ps(–), 2 ps( ), 4 ps(–), 6 ps(–), 8 ps(–), 10 ps (–), and Bottom panel (1-300 ps): 0.5 ps(–), 2 ps(–), 5

into the triplet manifold, rather than the singlet manifold, yields differences in early time difference spectra of $[Os(bpy)_3]^{2+}$, which does not show the initial red shift. The absence of the initial red shift at early time when the ^{3}MLCT state is directly populated further

94

supports the idea that the red shift of the spectrum is due to intersystem crossing. Blue shifting of the spectrum on the picosecond timescale is less pronounced in with excitation into the ^{3}MLCT state; however, there is still a slight blue shift. The differences in the long-time dynamics with various pump wavelengths, from 10 ps to 300 ps, have been reported previously by Papanikolas and coworkers.[13] Figure 4-7 presents full spectral data at various time intervals for excitation into the ^{1}MLCT state (left) and excitation into the ^{3}MLCT state (right). Scatter from the pump beam is manifest at ~600 nm and is more pronounced at early times. As mentioned above these unique early time dynamics are most likely due to intersystem crossing, as the initial red shift in the ^{1}MLCT excitation spectra, and interligand electron transfer couple with solvent relaxation which is manifest as a blue shift and present at both excitation wavelengths.

Despite the differences in the dynamics associated with forming the long-lived excited states of $[Ru(bpy)_3]^{2+}$ and $[Os(bpy)_3]^{2+}$, both complexes possess charge transfer long-lived excited states as implied by the correlation of the spectroelectrochemical measurements (Figure 4-3) and the long time spectra of each complex. Due to the intrinsically large crystal field splitting intrinsic to second and third row transition metals[4], it is reasonable to assume that the complexes possess unoccupied π^* orbitals of the ligand which lie below the unoccupied e_g^* orbitals of the metal making a ligand localized, charge transfer state, the lowest energy excited state. In the case of first row transition metals, such at iron, the crystal field splitting is significantly less, causing the e_g^* orbitals to lie below the π^* orbitals of the ligand. With the unoccupied metal centered orbitals lower in energy than the unoccupied ligand orbital the lowest energy excited state for iron(II) will be localized on the metal resulting in an excited state that is ligand field in nature. Comparison of the long time spectra in Figure 4-5 illustrate this difference, in that both the $[Ru(bpy)_3]^{2+}$ and $[Os(bpy)_3]^{2+}$ long time spectra retain charge transfer features consistent with their long-lived charge transfer excited states; while $[Fe(bpy)_3]^{2+}$ shows no evidence of a charge transfer state.
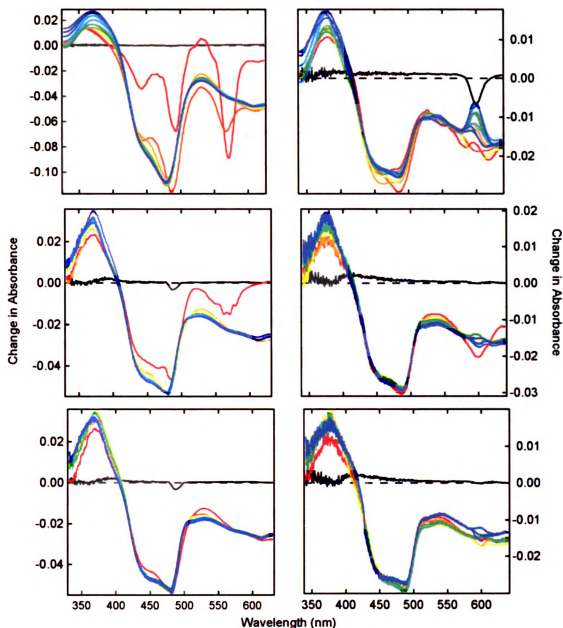
Figure 4-7. Variable pump full spectra of [Os(bpy)₃]²⁺ in acetonitrile.
Left: 490 nm excitation (¹MLCT) Right: 600 nm excitation (³MLCT) In time intervals of Top panel (0-1 ps):
0 ps(–), 0.1 ps(–), 0.2 ps( ), 0.3 ps( ), 0.4 ps( ), 0.5 ps(–), 0.6 ps( ), 0.8 ps( ), 0.9 ps(–), 1 ps(–), 1.2 ps (–)
Middle panel (0.5-10 ps): 0.5 ps(–), 1 ps(–), 2 ps( ), 4 ps(–), 6 ps(–), 8 ps(–), 10 ps (–), and Bottom panel

A report by Monat and McCusker suggests that the ¹MLCT state of iron(II) complexes is deactivated in less than 100 fs.[29] Considering the spectra of [Fe(bpy)₃]²⁺, [Ru(bpy)₃]²⁺, and [Os(bpy)₃]²⁺ at Δt = 0 ps, Figure 4-8, the three spectra show positive features in the

anticipated regions indicating that the charge transfer state is populated. Figure 4-9 shows data collected at 390 nm probe, corresponding to the radical anion of the bipyridine ligand. The early-time positive signal present for the three complexes is indicative of the formation
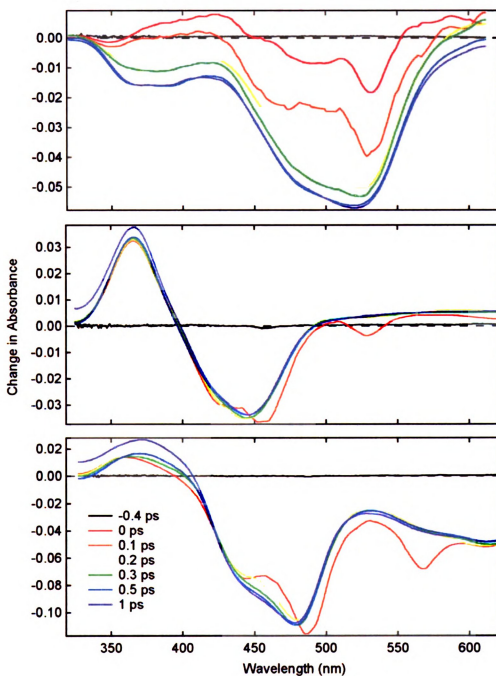
Figure 4-8. Transient absorption spectra of $[M(bpy)_3]^{2+}$ in acetonitrile.
Top panel is $[Fe(bpy)_3]^{2+}$; Middle panel is $[Ru(bpy)_3]^{2+}$; Bottom panel is $[Os(bpy)_3]^{2+}$.
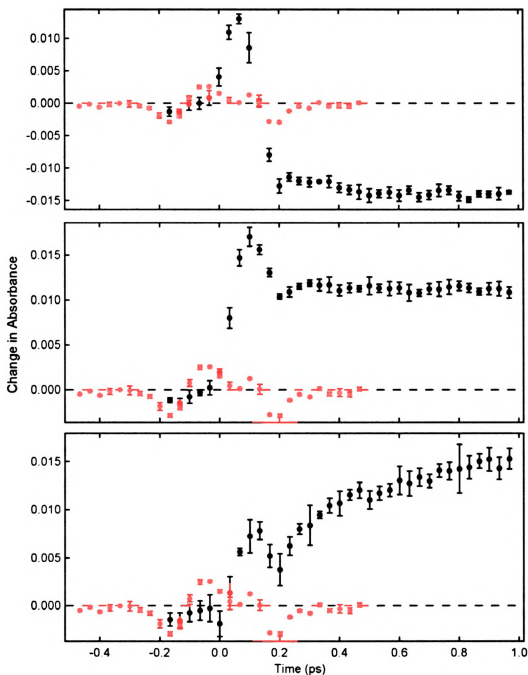
Figure 4-9. Early time kinetic traces of of $[M(bpy)_3]^{2+}$ in acetonitrile.
Kinetic data at 450 nm pump is shown for each $[M(bpy)_3]^{2+}$ complex. A corresponding solvent response is also plotted for each trace in red. Top panel is $[Fe(bpy)_3]^{2+}$ at 420 nm probe; Middle panel is $[Ru(bpy)_3]^{2+}$

of a MLCT state, in the case of $[Ru(bpy)_3]^{2+}$ and $[Os(bpy)_3]^{2+}$ the signal persists for longer

than 1 ps[13, 23] and the $[Fe(bpy)_3]^{2+}$ signal rapidly decays to a negative value. The presence

of a positive feature in the $[Fe(bpy)_3]^{2+}$ trace at early-times emphasizes a couple of points.

First, the initially formed ^{1}MLCT excited state is observable at early times and the spectral features correlate well with those observed in spectroelectrochemical measurements. Second, the lifetime of the ^{1}MLCT state in [Fe(bpy)$_3$]$^{2+}$ is ultrafast, indicating depopulation of the initially excited state happens very rapidly.[29-31]

4.3.4 Ultrafast time-resolved transient absorption spectroscopy of low-spin polypyridyl iron(II) complexes

In 1980, Carol Creutz and Norman Sutin published a report on the excited state lifetimes of a series of iron(II) complexes.[1] Since this publication time-resolved spectroscopic techniques have undergone significant advances. While an instrument response function (IRF) on the order of 10 ps was obtained for the experimental set up used in the 1980 Creutz and Sutin report, an IRF of approximately 120 fs is now available with our ultrafast transient absorption apparatus. Despite this temporal restriction Creutz and Sutin were able to successfully resolve the ground state recovery times of a series of iron(II) polypyridyl complexes and those lifetimes are presented in Table 4-1. These lifetimes ranged from 0.8 ns for [Fe(bpy)$_3$]$^{2+}$ in water to 2.5 ns for [Fe(terpy)$_2$]$^{2+}$ in water, and similar values have been reported in methanol.[1, 30, 31] Figure 4-10 illustrates ground state recovery dynamics associated with a series of iron(II) complexes, [Fe(bpy)$_3$]$^{2+}$, [Fe(dmb)$_3$]$^{2+}$,[Fe(phen)$_3$]$^{2+}$ and

Table 4-1. Relevant lifetimes for select iron(II) polypyridine complexes of interest.

	$\tau\,^5T_2{}^a$	τ_1 (MLCT)	τ_2 (Solvent)	τ_3 (Vibrational Cooling)
[Fe(bpy)$_3$]$^{2+}$	0.81 ± 0.07 ns	60 ± 10 fs	220 ± 10 fs	-
[Fe(dmb)$_3$]$^{2+}$	0.76 ± 0.04 ns	60 ± 10 fs	270 ± 10 fs	-
[Fe(phen)$_3$]$^{2+}$	0.80 ± 0.07 ns	70 ± 20 fs	420 ± 20 fs	10 ± 1.5 ps
[Fe(terpy)$_2$]$^{2+}$	2.5 ± 0.13 ns	80 ± 20 fs	300 ± 20 fs	1 ± 0.2 ps

^{a} From references 1 and 21
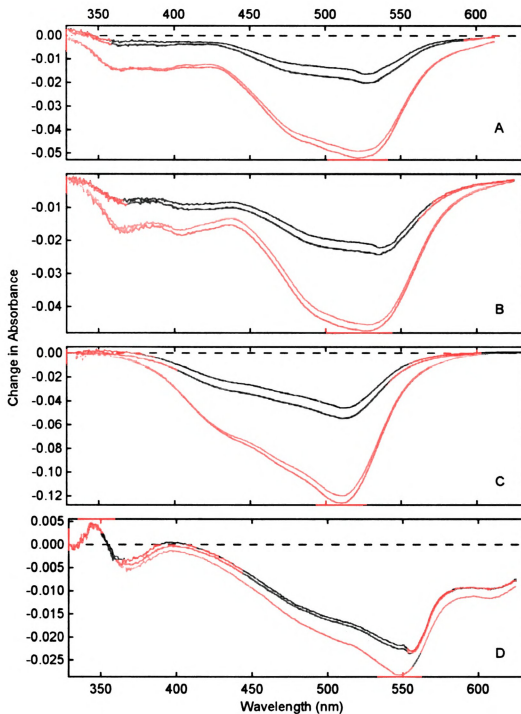
Figure 4-10. Transient absorption spectra showing ground state recovery for the iron(II) series. Delays of 1 ps (red, —), 90 ps (orange, —), 200 ps (yellow, —), 500 ps (green, —), and 1 ns (blue, —) are shown for all complexes. A) $[Fe(bpy)_3]^{2+}$; B) $[Fe(dmb)_3]^{2+}$; C) $[Fe(phen)_3]^{2+}$; D) $[Fe(terpy)_2]^{2+}$.

[Fe(terpy)$_2$]$^{2+}$. All traces show the expected dynamics reported by Sutin in 1980 and others.[1,] [30-32] It can be seen from Figure 4-10 that the long-lived excited states of both [Fe(bpy)$_3$]$^{2+}$ and [Fe(dmb)$_3$]$^{2+}$ manifest as negative signals across the entire spectral window presented. While [Fe(phen)$_3$]$^{2+}$ and [Fe(terpy)$_2$]$^{2+}$ exhibit small positive features in the ~350 nm region of their long-lived excited state spectra. This indicates that for the most part population of the long-lived excited state of iron(II) polypyridyl complexes results in a negative feature called a bleach, due to the lack of ground state population and weak if any excited state absorption. The exception being the 350 nm region for [Fe(phen)$_3$]$^{2+}$ and [Fe(terpy)$_2$]$^{2+}$, where the long-lived state absorbs more than the ground state. Initial classification of this ligand field state was difficult due to the high density of low-lying ligand field state present in iron(II) complexes; however, it is now know that this state is the $^5T_2$ state.[33]

In the interest of establishing a more complete understanding of the photophysics associated with the iron(II) polypyridyl complexes mentioned above both single wavelength kinetic traces and time-resolved full spectral data are presented for each complex. Using the spectroelectrochemical data in Figure 4-4 wavelengths that correspond to a positive signal absorption will be probed to determine if the ^{1}MLCT state can be observed. And Figure 4-10 indicates that once the system has crossed into the long-lived state the signal should change to a negative signal. Single wavelength kinetic studies were focused on finding the spectroscopic handle of a positive signal decaying to a negative signal. Monat and McCusker reported a similar spectroscopic handle in 2000 and follow up studies have further strengthened their argument.[29].

[Fe(bpy)$_3$]$^{2+}$ dynamics. Excitation of a sample of [Fe(bpy)$_3$]$^{2+}$ was achieved with 530 nm, corresponding to the peak of the lowest energy MLCT band. Figure 4-2A shows the absorption spectrum of [Fe(bpy)$_3$]$^{2+}$ in acetonitrile and the arrow indicates the wavelength of excitation. Figure 4-11 illustrates the spectral evolution of the excited state of [Fe(bpy)$_3$]$^{2+}$ from the initially formed ^{1}MLCT state to the long-lived ligand field state ($^5T_2$). The majority of the decay occurs in less than a picosecond.
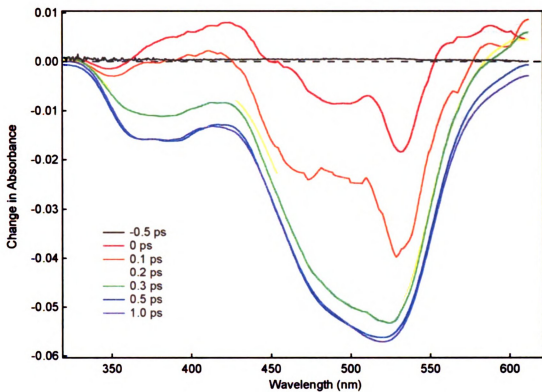
Figure 4-11. Early time transient absorption full spectral traces for $[Fe(bpy)_3]^{2+}$ in acetonitrile following 520 nm excitation.
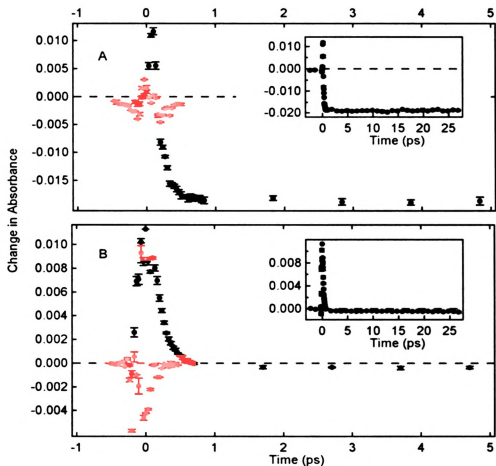
Figure 4-12. Single wavelength kinetic traces for $[Fe(bpy)_3]^{2+}$ in acetonitrile.
A: 420 nm probe following 520 nm excitation. B: 650 nm probe following 520 nm excitation. Corresponding solvent traces are shown in red for each probe wavelength.

Single wavelength traces at 400 nm and 650 nm show the ultrafast decay of the ^{1}MLCT signal and the rapid population of the $^5T_2$ state, respectively Figure 4-12A and B. Deconvolution of the 400 nm trace yields a time constant for the deactivation of the ^{1}MLCT as 60 fs ± 10 fs.

$[Fe(dmb)_3]^{2+}$ dynamics. Excitation of a sample of $[Fe(dmb)_3]^{2+}$ was achieved with 520 nm, corresponding to the peak of the lowest energy MLCT band. Figure 4-2B shows the absorption spectrum of $[Fe(dmb)_3]^{2+}$ in acetonitrile with the arrow marking the wavelength of excitation. Figure 4-13 illustrates the spectral evolution of the excited state of $[Fe(dmb)_3]^{2+}$ from the initially formed ^{1}MLCT state to the long-lived $^5T_2$ state. Again,

Figure 4-13. Early time transient absorption full spectral traces for [Fe(dmb)₃]²⁺ in acetonitrile following 510 nm excitation.

Figure 4-14. Single wavelength kinetic traces for $[Fe(dmb)_3]^{2+}$ in acetonitrile.
A: 420 nm probe following 510 nm excitation. B: 650 nm probe following 510 nm excitation. Corresponding solvent traces are shown in red for each probe wavelength.

the majority of the decay occurs in less than a picosecond.

Single wavelength traces at 400 nm and 650 nm show the ultrafast decay of the ^1MLCT signal and the rapid population of the $^5T_2$ state, respectively Figure 4-14A and B. Deconvolution of the 400 nm trace yields a time constant for the deactivation of the ^1MLCT as 60 fs ± 10 fs.

$[Fe(phen)_3]^{2+}$ dynamics. Excitation of a sample of $[Fe(phen)_3]^{2+}$ was achieved at 510 nm, corresponding to the peak of the lowest energy MLCT band. Figure 4-2C shows the absorption spectrum of $[Fe(phen)_3]^{2+}$ in acetonitrile and the arrow indicating the
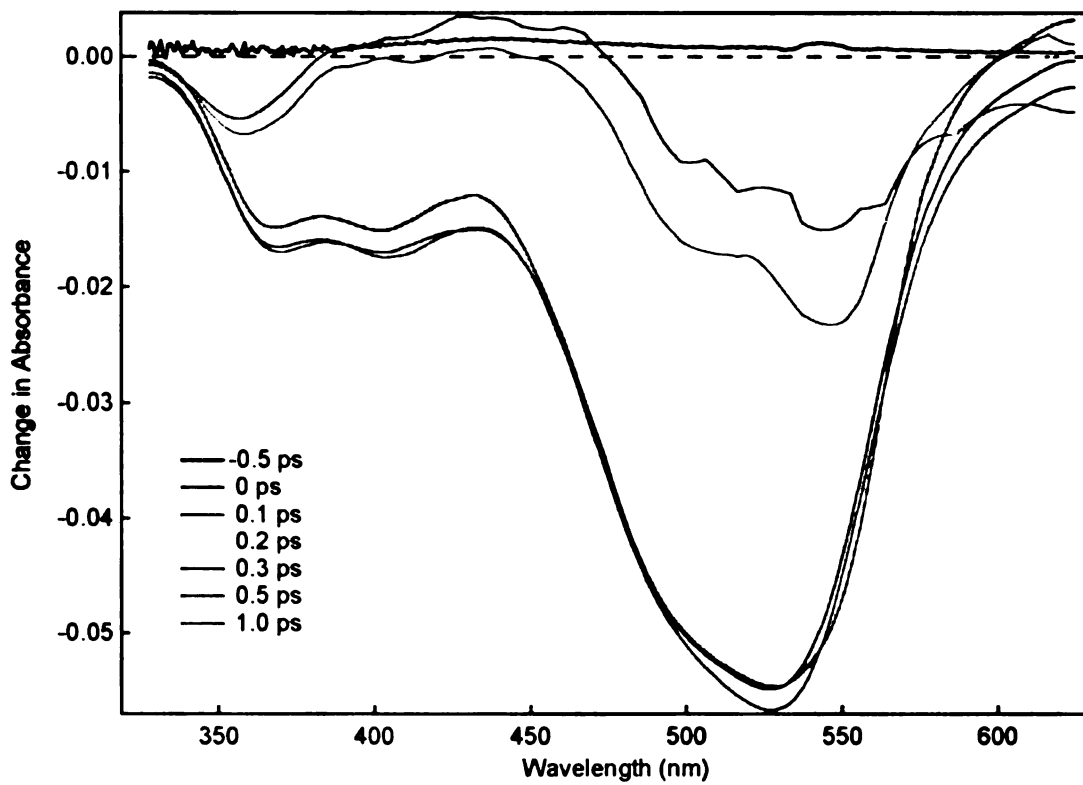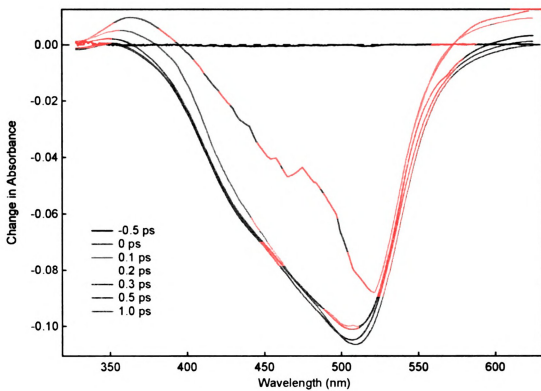
Figure 4-15. Early time transient absorption full spectral traces for [Fe(phen)$_3$]$^{2+}$ in acetonitrile following 530 nm excitation.

wavelength of excitation. Figure 4-15 illustrates the spectral evolution of the excited state of $[Fe(phen)_3]^{2+}$ from the initially formed ^{1}MLCT state to the long-lived $^5T_2$ state with the majority the decay from the ^{1}MLCT state occurs in under a picosecond.

Single wavelength traces at 370 nm and 650 nm show the ultrafast decay of the ^{1}MLCT signal and the rapid population of the $^5T_2$ state, respectively Figure 4-16A and B. Deconvolution of the 370 nm trace yields a time constant for the deactivation of the ^{1}MLCT as 70 fs ± 20 fs. Figure 4-17 shows an enlarged view of the blue region of the
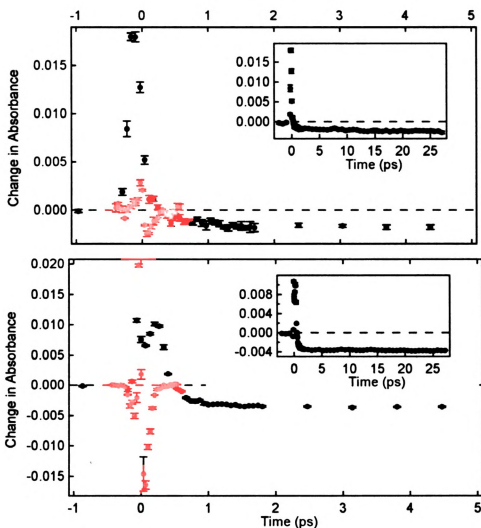
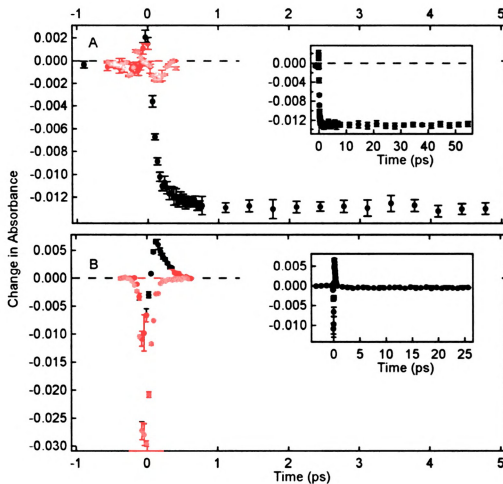

Figure 4-16. Single wavelength kinetic traces for $[Fe(phen)_3]^{2+}$ in acetonitrile. Top: 370 nm probe following 530 nm excitation. Bottom: 650 nm probe following 530 nm excitation. Corresponding solvent traces are shown in red for each probe wavelength.

spectrum. Here the long-lived excited state absorbs more than the ground state yielding a net positive signal on the picosecond timescale. As shown in the single wavelength kinetic traces the ^{1}MLCT state still rapidly deactivated to the ligand field manifold. In the 350 nm trace the long-lived state shows the net absorption and the 390 nm show a net bleach, when
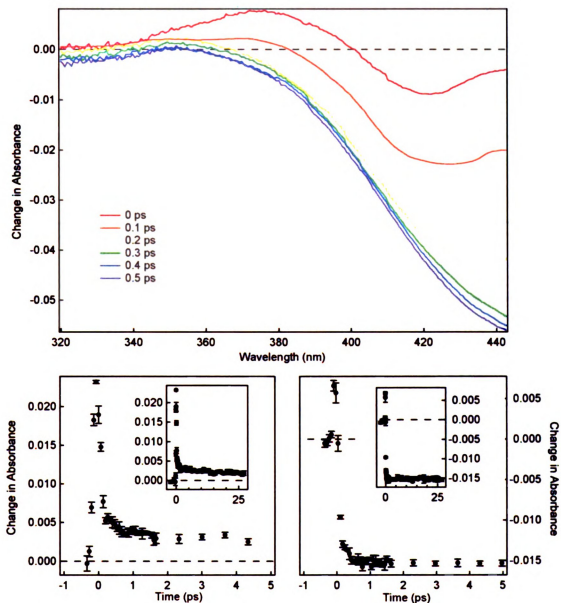
Figure 4-17. Transient absorption full spectral traces for [Fe(phen)$_3$]$^{2+}$ and blue single wavelength kinetic traces in acetonitrile following 530 nm excitation.
Full spectral data (Top) is an expanded view of the blue region of the transient spectra of Figure 3-11. Single wavelength kinetic data (Bottom) shows the rapid decay of the ^{1}MLCT state to the ligand field manifold. The kinetic trace on the left shows 350 nm probe data and the trace on the right shows 390 nm probe data, as

the molecule populates the long-lived state. Deconvolution of the 350 nm trace yields a time constant for the deactivation of the ^{1}MLCT as 80 fs $\pm$ 20 fs, a 120 $\pm$ 20 fs component, and a long time component of 10 $\pm$ 1.5 ps attributed to vibrational cooling. The 120 fs component was assigned to a librational mode of the solvent, which has been reported previously.[34, 35]

[Fe(terpy)$_2$]$^{2+}$ dynamics. Excitation of a sample of [Fe(terpy)$_2$]$^{2+}$ was achieved with 560 nm, corresponding to the peak of the lowest energy MLCT band. Figure 4-2D shows the absorption spectrum of [Fe(terpy)$_2$]$^{2+}$ in acetonitrile and the arrow marks the wavelength of excitation. Figure 4-18 illustrates the spectral evolution of the excited state of [Fe(terpy)$_2$]$^{2+}$ from the initially formed ^{1}MLCT state to the long-lived ^{5}T$_2$ state with the majority of the decay occurring in less than a picosecond.
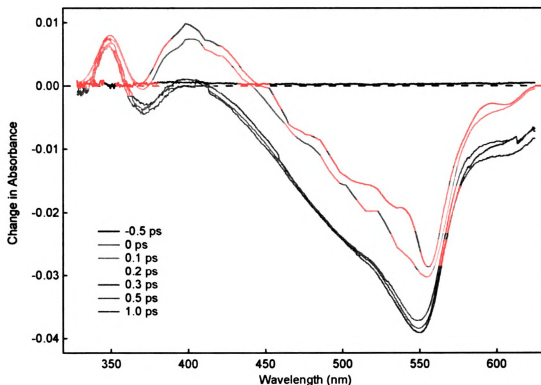
Figure 4-18. Early time transient absorption full spectral traces for [Fe(terpy)$_2$]$^{2+}$ 560 nm excitation.

Single wavelength traces at 410 nm and 680 nm show the ultrafast decay of the
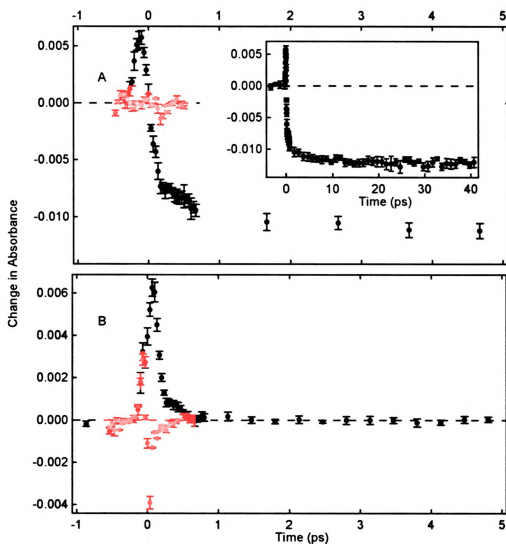
Figure 4-19. Single wavelength kinetic traces for $[Fe(terpy)_2]^{2+}$ in acetonitrile.
Top: 460 nm probe following 560 nm excitation. Bottom: 700 nm probe following 560 nm excitation.
Corresponding solvent traces are shown in red for each probe wavelength.

^{1}MLCT signal and the rapid population of the $^5T_2$ state, Figure 4-19A and B respectively.

Deconvolution of the 410 nm trace yields a time constant for the deactivation of the

^{1}MLCT as 80 fs $\pm$ 10 fs. Figure 4-20 shows an enlarged view of the blue region of the

spectrum. Here the long-lived excited state absorbs more than the ground state yielding a

positive signal on the nanosecond timescale. As shown in single wavelength kinetic traces

the ^{1}MLCT state still rapidly deactivated to the $^5T_2$ state. In the 350 nm trace the long-

lived state shows a net absorption and the 410 nm shows a net bleach, when the molecule
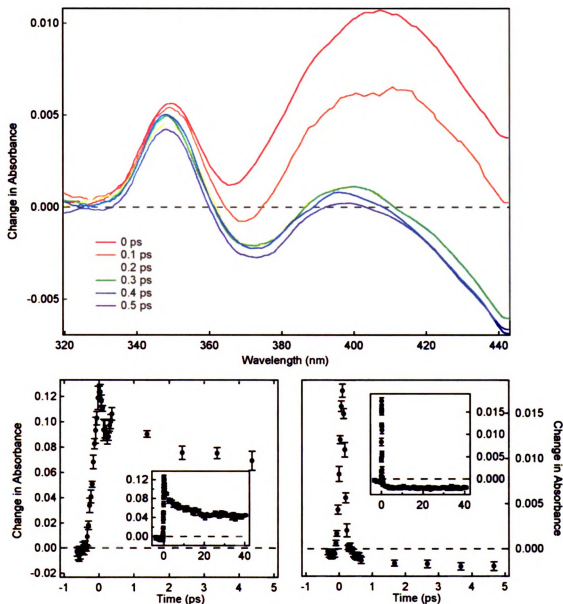
Figure 4-20. Transient absorption full spectral traces for [Fe(terpy)₂]²⁺ and blue single wavelength kinetic traces in acetonitrile following 560 nm excitation.

Full spectral data (Top) is an expanded view of the blue region of the transient spectra of Figure 3-18. Single wavelength kinetic data (Bottom) shows the rapid decay of the ¹MLCT state to the ligand field manifold. The kinetic trace on the left shows 350 nm probe data and the trace on the right shows 410 nm probe data, as discussed in the text.

populates the long-lived state. Deconvolution of the 350 nm trace yields a time constant for the deactivation of the ^{1}MLCT as 60 fs ± 20 fs, a component that has a 200 ± 10 fs lifetime, and a longer time component of 10 ± 1 ps that is assigned to vibrational cooling.

The 200 fs component was assigned to a librational mode of the solvent, which has been reported previously.[34, 35]

4.4 Conclusions

In the 1980 report of the excited state dynamics of iron(II) polypyridyl complexes, the lack of a spectroscopic tag for the ^{1}MLCT state indicated that the observes excited state for the iron(II) polypyridyl complexes was not charge transfer in nature and the observable dynamics were insensitive to the ligand coordinated to the metal center[1], which was not the case for two well studies chromophores $[Ru(bpy)_3]^{2+}$ and $[Os(bpy)_3]^{2+}$.[12, 13, 23, 28, 36] The long-lived state of a series of iron(II) polypyridyl complexes is ascribed to a ligand field state, $^5T_2$, due to their spectral features and ligand insensitive lifetime.[1] A report in 2000, from Monat and McCusker indicates that iron(II) polypyridyl complexes rapidly populate the long-lived ligand field state in less than 100 fs, which explain the lack of evidence for the population of a charge transfer state in the iron(II) complexes since the iron chromophores had populated their long-lived state within the instrument response time.[1, 29]

In this study all complexes studied exhibit a spectroscopic handle of a positive signal decaying rapidly to a negative signal, associated with the ^{1}MLCT state decaying rapidly to the ligand field manifold, which was. The results from the iron(II) polypyridyl complexes in this study indicated that the deactivation of the initially excited ^{1}MLCT state to the long-lived $^5T_2$ ligand field state is ultrafast. While time constants vary, the deactivation process seemed to take less than 100 fs and was complete by 500 fs in all complexes, as reported in Table 4-1. Assignments of subsequent processes, once in the ligand field manifold were not easily achieved, due to the high density of low-lying ligand field states present in iron(II) complexes. From spin-crossover literature[33, 37] and the Tanaube-Sugano diagram for d^6 metals we have reason to believe that the long-lived state is $^5T_2$ in nature and it returns to the ground state in approximately 800 ps for $[Fe(bpy)_3]^{2+}$, $[Fe(dmb)_3]^{2+}$ and $[Fe(phen)_3]^{2+}$ and approximately 2.5 ns for $[Fe(terpy)_2]^{2+}$.[1, 30, 31]

The 1998 report of a very small photocurrent from an iron(II) polypyridyl complex

bound to TiO_2 is an ideal forum to apply the results obtained in this study.[38] Ferrere and Gregg reported the generation of a photocurrent from an iron(II)-based sensitizer; however, the observed current was approximately three orders of magnitude smaller than that obtained from a similar ruthenium(II) based sensitizer. The significantly small photocurrent observed by Ferrere and Gregg may be a consequence of the ultrafast conversion from the [1]MLCT state to a ligand field state in iron(II) polypyridyl complexes. Studies are underway to better characterize the intrinsic behavior of the iron(II)-based sensitizer used by Ferrere and Gregg; in an attempt to determine if the ultrafast deactivation of the [1]MLCT state significantly reduces the photocurrent of iron(II)-based dye sensitized solar cells.

4.5 References

1. Creutz, C.; Chou, M.; Netzel, T. L.; Okumura, M.; Sutin, N. *J. Am. Chem. Soc.* **1980**, *102*, 1309-19.

2. Chang, H.-R.; McCusker, J. K.; Toftlund, H.; Wilson, S. R.; Trautwein, A. X.; Winkler, H.; Hendrickson, D. N. *J. Am. Chem. Soc.* **1990**, *112*, 6814-6827.

3. Juban, E.; McCusker, J. K. *J. Am. Chem. Soc.* **2005**, *127*, 6857-6865.

4. Lever, A. B. P. *"Inorganic Electronic Spectroscopy"*. American Elsevier: New York, 1968; p 302-303.

5. Fergusson, J. E.; Harris, G. M. *J. Chem. Soc. A, Inorg. Phys., Theoret.* **1966**, 1293-6.

6. Felix, F.; Ferguson, J.; Guedel, H. U.; Ludi, A. *Chem. Phys. Lett.* **1979**, *62*, 153-7.

7. Decurtins, S.; Felix, F.; Ferguson, J.; Guedel, H. U.; Ludi, A. *J. Am. Chem. Soc.* **1980**, *102*, 4102-6.

8. Ceulemans, A.; Vanquickenborne, L. G. *J. Am. Chem. Soc.* **1981**, *103*, 2238-41.

9. Ferguson, J.; Herren, F. *Chem. Phys. Lett.* **1982**, *89*, 371-375.

10. Kober, E. M.; Meyer, T. J. *Inorg. Chem.* **1982**, *21*, 396739-77.

11. Ferguson, J.; Herren, F. *Chem. Phys.* **1983**, *76*, 45-59.

12. Shaw, G. B.; Brown, C. L.; Papanikolas, J. M. *J. Phys. Chem. A* **2002**, *106*, 1483-1495.

13. Shaw, G.; Styers-Barnett, D. J.; Gannon, E. Z.; Granger, J. C.; Papanikolas, J. M. *J. Phys. Chem. A* **2004**, *108*, 4998-5006.

14. Hanazaki, I.; Nagakura, S. *Inorg. Chem.* **1969**, *8*, 648-54.

15. Hazra, D. K.; Lahiri, S. C. *Zeitschrift fuer Physikalische Chemie (Leipzig)* **1976**, *257*, 497-506.

16. Madeja, K.; Konig, E. *J. of Inorg. Nuc. Chem.* **1963**, *25*, 377-385.

17. Braterman, P. S.; Song, J. I.; Peacock, R. D. *Inorg. Chem.* **1992**, *31*, 555-9.

18. Berger, R. M.; McMillin, D. R. *Inorg. Chem.* **1988**, *27*, 4245-4249.

19.   Zhou, X.; Ren, A. M.; Feng, J. K. *Journal of Organometallic Chemistry* **2005**, *690*, 338-347.

20.   Mahon, C.; Renoylds, W. *Inorg. Chem.* **1967**, *6*, 1927-1928.

21.   Juirs, A.; Balzani, V.; Barigelletti, F.; Campagna, S.; Belser, P.; von Zelewsky, A. *Coord. Chem. Rev.* **1988**, *88*, 85-277.

22.   Bergkamp, M. A.; Gutlich, P.; Netzel, T. L.; Sutin, N. *J. Phys. Chem.* **1983**, *87*, 3877-3883.

23.   Damrauer, N. H.; Cerullo, G.; Yeh, A.; Boussie, T. R.; Shank, C. V.; McCusker, J. K. *Science* **1997**, *275*, 54-57.

24.   Bhasikuttan, A. C.; Suzuki, M.; Nakashima, S.; Okada, T. *J. Am. Chem. Soc.* **2002**, *124*, 8398-8405.

25.   Kukura, P.; Yoon, S.; Mathies, R. A. *Anal. Chem.* **2006**, 5953.

26.   Yoon, S.; Kukura, P.; Stuart, C. M.; Mathies, R. A. *Molecular Physics* **2006**, *104*, 1275-1282.

27.   Murtaza, Z.; Graff, D. K.; Zipp, A. P.; Worl, L. A.; Jones, W. E.; Bates, W. D.; Meyer, T. J. *J. Phys. Chem.* **1994**, *98*, 10504-10513.

28.   Pogge, J. L.; Kelley, D. F. *Chem. Phys. Lett.* **1995**, *238*, 16-24.

29.   Monat, J. E.; McCusker, J. K. *J. Am. Chem. Soc.* **2000**, *122*, 4092-4097.

30.   McCusker, J. K.; Walda, K. N.; Dunn, R. C.; Simon, J. D.; Magde, D.; Hendrickson, D. N. *J. Am. Chem. Soc.* **1992**, *114*, 6919-6920.

31.   McCusker, J. K.; Walda, K. N.; Dunn, R. C.; Simon, J. D.; Magde, D.; Hendrickson, D. N. *J. Am. Chem. Soc.* **1993**, *115*, 298-307.

32.   Hauser, A. *Chem. Phys. Lett.* **1990**, *173*, 507-512.

33.   Hauser, A. *Coord. Chem. Rev.* **1991**, *111*, 275-290.

34.   Roy, S.; Bagchi, B. *J. Chem. Phys.* **1993**, *97*, 9938-9943.

35.   Ladanyi, B. M.; Stratt, R. M. *J. Phys. Chem.* **1995**, *99*, 2502-2511.

36.   Damrauer, N. H.; McCusker, J. K. *J. Phys. Chem. A* **1999**, *103*, 8440-8446.

37.   Browne, W. R.; McGarvey, J. J. *Coord. Chem. Rev.* **2006,** *250,* 1696-1709.

38.   Ferrere, S.; Gregg, B. *J. Am. Chem. Soc.* **1998,** *120,* 843.

Chapter 5. Ultrafast Dynamics Associated with Iron(II)-based Sensitizers for TiO$_2$-based Dye Sensitized Solar Cells.

5.1 Introduction:

Following the initial report of a ruthenium(II) polypyridyl complex successfully generating a photocurrent when bound to TiO$_2$ by Grätzel and coworkers the field of dye sensitized solar cells (DSSCs) exploded.[1] The novel idea of using simple coordination compounds as sensitizers for wide band gap semiconductors took off. Extensive amounts of time and effort have gone into synthesizing the perfect sensitizer and optimal electrolyte conditions.[2] A majority of the sensitizers reported to date are ruthenium(II) containing sensitizers; however, a wide range of complexes have been incorporated into these versatile DSSCs.[3] In 1998, Susanne Ferrere and Brian Gregg reported on the first iron(II) based sensitizers.[4] The observed photocurrent was low ~290 µA compared to the 16 mA commonly observed with ruthenium(II) sensitizers.[2,4]

While there have been few studies of iron(II) based sensitizers some information is available on the intrinsic dynamics associated with iron(II) polypyridyl complexes. A 1980 report by Sutin and coworkers found that ground state recovery of a series of iron(II) polypyridyl complexes occurred on the hundreds of picoseconds to nanosecond time scale.[5] Sutin also proposed that the long-lived excited state in the series of iron(II) complexes studied was ligand field in nature. In 2000, Monat and McCusker published their findings of ultrafast dynamics associated with charge transfer to ligand field conversion of the excited state of a low-spin iron(II) polypyridyl complex.[6] Monat and McCusker were able to identify their long-lived excited state at the $^5T_2$ state by synthesizing a second complex, high-spin iron(II), that closely resemble their low-spin molecule of interest.

Recent work, also by McCusker and coworkers, indicates that the lifetime of the ^{1}MLCT state of a series of low-spin iron(II) complexes is less than 100 fs.[7] The focus of this research is to determine the lifetime of the initially formed excited state of the known

iron(II) sensitizer bis(cyano)bis(2,2'-bipyridine-4,4'-dicarboxcylic acid)iron(II) and its impact on electron injection. Other closely related complexes will be studied to provide a more in depth understanding of the intrinsic dynamics of iron(II) based sensitizers.

5.2 Experimental

5.2.1 Synthesis

General. All reagents were obtained from commercial sources and used without further purification unless noted. Elemental analyses were obtained through the Analytical Facilities at Michigan State University. ^{1}H NMR spectra were collected on a Varian 300 MHz spectrometer. The solvent used for each electronic absorption measurement is indicated below.

FeCl$_2$•2H$_2$O. Purification of FeCl$_2$•4H$_2$O to FeCl$_2$•2H$_2$O was done according to a literature method with the following modifications.[8] A round bottom flask was charged with 10 g (0.050 mol) of FeCl$_2$•4H$_2$O with 50 mL of H$_2$O, and 0.42 g (7.5 mmol) of Fe^0. The solution was degassed and brought to reflux for five minutes under Ar. Then 2.0 mL of 12 M HCl was added; and the reaction was maintained at reflux for 30 minutes, during which the solution changed from orange to pale green. Vacuum distillation removed excess water, leaving a few pale green crystals amongst white powder indicating a mixture of FeCl$_2$•4H$_2$O and FeCl$_2$•2H$_2$O.

2,2'-bipyridine-4,4'-dimethyl (dmb). Synthesis of dmb was achieved by following a procedure presented in the literature.[9] 700 mL of 4-methylpiocline were freshly distilled into a round bottom flask. Then 20 g of Pd/carbon catalyst was added to the charged round bottom. The mixture was then brought to reflux and maintained for five days. After five days, 50 mL of hot benzene was added to the reaction and refluxed for and additional half an hour. To obtain product the reaction mixture was filtered while hot and then the volume reduced. An off white precipitate formed; and this was then recrystallized with ethyl acetate to yield crystalline product. Calc. for 2,2'-bipyridine-4,4'-dimethyl (C$_{12}$H$_{12}$N$_2$): C, 78.23;

H, 6.565: N, 15.20.

H$_2$dcbpy. Preparation of 2,2'-bipyridine-4,4'-dicarboxcylic acid was achieved by oxidation of 2,2'-bipyridine-4,4'-dimethyl (dmb) with 10 fold xs CrO$_3$ in concentrated sulfuric acid.[10] 0.5 g of dmb was placed in 50 mL of conc H$_2$SO$_4$ and allowed to stir until completely dissolved. 5 g of CrO$_3$ was added slowly to the stiring solution to ensure that the temperature did not exceed 70 C. After stirring for and additional 2 hours the reaction was poured over crushed ice and a white precipitate formed. The precipitate was recovered via vacuum filtration. Recyrstallization was achieved by dissolution of the crude product in basic water (pH = 10) and precipitation with 2 M HCl. The precipitate was collected via vacuum filtration and dried under vacuum. Elemental Analysis: Calculated (C$_{12}$H$_8$N$_2$O$_4$) C 59.02%, N 11.47%, H 3.30%; Found C 58.85 %, N 11.07 %, H 4.01%. ^{1}H NMR (D$_2$O) δ(ppm, multiplicity): 8.60 (d, J=6 Hz); 8.21 (s); 7.68 (d, J=6 Hz).

Na$_2$dcbpy. The disodium(2,2'-bipyridine-4,4'-dicarboxylate) was isolated by dissolution of the H$_2$dcbpy in basic water and precipitation of the sodium salt by addition of 5 M sodium hydroxide. The product was isolated with vacuum filtration and dried under vacuum. Elemental Analysis: Calculated (Na$_2$C$_{12}$H$_6$N$_2$O$_4$) C 50.02%, N 9.72%, H 2.10%; Found C 49.75%, N 9.22%, H 3.06%.

[Fe(bpy)$_3$](Cl)$_2$ (1). Preparation of the chloride salt of [Fe(bpy)$_3$]$^{2+}$ was done as reported previously, without the metathesis to the hexaflurophophate salt.[7] Briefly, a 100mL round bottom flask was charged with 0.11 (0.67 mmol) g of FeCl$_2$•2H$_2$O and 0.315 g (2 mmol) of 2,2'-bipyridine in an inert nitrogen atmosphere. Approximately 50 mL of methanol was degassed via bubbling dry nitrogen and stirring for 30 minuets, at which point the degassed methanol was canula transferred to the charged round bottom. A deep red color developed immediately. The solution was allowed to stir for an additional 1 hour under a nitrogen blanket. Isolation of the dichloride salt was achieved with precipitation of the reaction mixture with diethylether and subsequent recrystallization from methanol via ether diffusion. Elemental Analysis: Calculated [Fe(bpy)$_3$](Cl)$_2$•5.5H$_2$O (C$_{30}$H$_{35}$N$_6$Cl$_2$O$_{5.5}$Fe): C,

51.90; H, 5.08; N, 12.15. Found: C, 51.90%; H, 5.13%; N, 11.99%. UV-Vis in CH_3CN $\lambda(\epsilon)$: 248 (17 000), 298 (40 000), 352 (4 100), 480 (4 500), 524 (5 400). ^1H NMR (d_3-acetonitrile) δ(ppm, multiplicity): 8.5 (d, J=10 Hz); 8.1 (m, J=8 Hz); 7.4 (d, J=4 Hz)

$Na_4[Fe(dcbpy)_3]$ (2). Where dcbpy is 2,2'-bipyridine-4,4'-dicarboxylate. $[Fe(dcbpy)_3]^{4-}$ was prepared by dissolution of 0.347 g of Na_2dcbpy in deionized water and addition of 0.147 g of $FeCl_2 \cdot 2H_2O$ to the stirring solution. A deep magenta color formed instantaneously and the reaction was allowed to stir for an additional hour to ensure complete reaction. Isolation of $Na_4[Fe(dcbpy)_3]$ was achieved by precipitation of the reaction mixture by pouring it into 150 mL of acetone. The product was collected by vacuum filtration and dried under vacuum. Recrystallization of $Na_2[Fe(dcbpy)_3]$ was achieved by dissolution of the crude product in 50 mL of methanol and placed in the refrigerator overnight. The chilled methanol solution was filtered and the filtrate was concentrated to 25 mL and precipitated by pouring the methanol solution into ~150 mL of acetone. Elemental Analysis: Calculated $Na_4[Fe(dcbpy)_3]$ ($Na_4C_{30}H_{24}N_6Fe$) (2): C 49.34%, N 9.59%, H 2.30%; Found C 48.89%, N 9.09%, H 3.50%. UV-Vis in CH_3OH $\lambda(\epsilon)$: 266 (18 000), 312 (41 000), 378 (6 900), 500 (7 200), 544 (9 300).

$Fe(bpy)_2(CN)_2$ (3). $Fe(bpy)_2(CN)_2$ was synthesized according to literature procedures with slight modification.[11] Briefly, 0.2 g of 1 was dissolved in 20 mL of deionized water. The solution was then heated to 90 °C and 0.313 g of KCN was added to the hot stirring solution. The mixture was allowed to stir an additional 30 minutes and upon cooling a dark precipitate formed. The precipitate was isolated by vacuum filtration. Recrystalization of 3 was done by precipitation from an acetonitrile solution upon addition of diethylether. Calc. for $Fe(bpy)_2CN_2 \cdot 1.4H_2O$ ($C_{22}H_{18.8}N_6O_{1.4}Fe$) (3): C, 59.32; N, 18.87; H. 4.25. Found: C, 59.23; N, 18.34; H, 4.08. UV-Vis in acetonitrile, nm (ϵ, $M^{-1}cm^{-1}$): 300 (33 000) 390 (6 800) 530 (4 100) 615 (7 100).

$Fe(dcbpy)_2(CN)_2$ (4). Synthesis of 4 was attempted using a literature preparation method described by Ferrere and Gregg.[4, 11, 12] To a suspension of 0.31 g (1.3 mmol) of

H$_2$dcbpy in 30 mL of water 1 M NaOH was added drop wise until complete dissolution was achieved. Then 0.41 g (0.4 mmol) of (NH$_4$)$_2$Fe(SO$_4$)$_2$•8H$_2$O was added and solution turned a deep red. The solution was heated to just below boiling and 1.01 g (0.015 mol) of KCN was added. The resultant solution was allowed to stir an additional 30 minuets. It was then cooled to room temperature and slowly acidified to remove excess CN⁻. The solution was further acidified to precipitate the excess ligand present in solution. At pH 4 the solution was filtered and further acidified to enable precipitation of the desired complex. Analytical analysis of the isolated complex indicated that **4** had not been successfully synthesized. Additional attempts will be discuss in the results section.

5.2.2 Sensitization of TiO$_2$ Films

A sandwich-cell configuration was used to study the injection dynamics associated with different sensitizers. The sandwich cell configuration consists of a sensitized slide, a Teflon spacer, and a glass cover slide. This configuration has been reported previously and is described below briefly.[13]

TiO$_2$ films on F-doped SnO$_2$ coated glass, received from the Lewis group at California Institute of Technology, were treated with a 0.2 M TiCl$_4$ for 8 hours. After at least 8 hours the films were rinsed and sintered under flowing air at 450 °C for 30 minutes and then maintained at 120 °C for approximately 2 hours.

As a control, ZrO$_2$ films are also prepared. ZrO$_2$ has a band gap of ~5 eV, compared to that of TiO$_2$ at ~3.0 eV. Little to no injection is expected when the sensitizer is bound to ZrO$_2$, which will enable the elucidation of dynamics associated with the injection process rather than an artifact of binding the sensitizer to a substrate.[3] Sensitized ZrO$_2$ films are prepared for dye adsorption in a similar manner as for TiO$_2$; however, no treatment of the surface with TiCl$_4$ was done prior to sintering. The clean ZrO$_2$ films were sintered at 450 °C for 30 minutes and allowed to rest at 120 °C for two hours, similar to the TiO$_2$ films.

The 120 °C films are immediately immersed in a solution of the sensitizer for a minimum of 24 hours.

5.2.3 Steady-state Absorption and Time-resolved Transient Absorption Spectroscopy

Steady-state absorption measurements were acquired with a Hewlett-Packard HP8452A diode array spectrophotometer. Samples were dissolved in an appropriate spectroscopy grade solvent.

The system used to collect the ultrafast transient absorption data has been reported elsewhere.[14]

Excitation energy was attenuated with neutral density filters and adjusted to a value that ensured a linear molecular response. Pump beam intensities were on the order of 6-7 µJ at wavelengths corresponding to the peak of the low energy metal to ligand charge transfer (MLCT) transition for each sample. Linearity was verified for each pump wavelength and sample combination. The optical density of each sample at the excitation was length was on the order of 0.6-0.8 in aerated HPLC grade acetonitrile or distilled water.

Continuum generation was achieved by focusing 805 nm light into a 1 cm thick plate of CaF_2 yielding probe wavelengths from 330 nm to 700 nm. Single wavelength kinetic traces were acquired by selecting a small portion of the continuum with 10 nm band-pass filters. Either neat solvent in 1 mm path length quartz cuvetts or a two-photon absorber, such as trichlorotoluene in acetonitrile, was used to establish $\Delta t=0$. Kinetic data was an average of approximately 8 scans, where a single scan was representative of a round trip of the translation stage collecting intensity information at each time point on the translation stage.

Presented full spectra are an average of 16-32 scans, with a single scan retaining its definition as indicated in the single wavelength measurements. Early time full spectral data were corrected for temporal chirp by adjusting for $\Delta t=0$ from a time-resolved full spectrum solvent trace. As mentioned previously, chirp-correction of rapidly evolving spectral features manifest with large amplitude changes are difficult to smoothly correct with the time resolution of the current instrumentation.[15] The presented early-time spectra were smoothed after chirp-correction with a box-car averaging method available in the

fitting software IGOR.

Due to temporal limitations of the instrumentation, complete ground state recovery was not observed. Each sample was checked for possible decomposition after the measurement and no signs of decomposition were observed, therefore we concluded that the ground state was completely repopulated, despite the limitation of our instrumentation, and no photoproducts are produced.

5.3 Results and Discussion

5.3.1 Synthesis

Synthesis of complexes **1-3** was straightforward and final products were easily isolated. Complex **4**; however, proved to be more difficult. The initial attempts at forming complex **4** followed the information provided in the 1998 report by Gregg and Ferrere.[4] Products collected from these reaction were evaluated by elemental analysis. All samples came back significantly disparate from the anticipated values. One possibility for the lack of correlation of the experimental elemental analysis with the anticipated values is the presence of excess salts. A second synthetic route was devised in an attempt to eliminate as many side products as possible.

The second route was to first isolate the tris(2,2'-bipyridine-4,4'-dicarboxylate)iron(II) complex and take that purified product on to the bis(cyano)bis(2,2'-bipyridine-4,4'-dicarboxylate)iron(II), complex **4**. In this attempt various equivalents of KCN were used to determine if the excess CN⁻ caused displacement of more then one dcbpy ligand. Isolation of a product that yielded an elemental analysis resembling any possible product was not obtained.

A second possible explanation for the significant difference in elemental analyses is that the sample may not be uniformly decomposed. Due to the strong hydrogen bonding ability of the $-CO_2H$ groups and the very hygroscopic nature of the $-CN^-$ ligands it is reasonable to assume that the sample was not completely decomposed during the

measurement and thus preventing accurate values from being obtained.

Other techniques such as IR and NMR should be able to identify if the complex has formed and if other species are present. By products that could form are $[Fe(H_2dcbpy)(CN)_4]^{2-}$, $[Fe(CN)_6]^{4-}$, $[Fe(H_2dcbpy)_2(CN)_2]^{1+}$, $[Fe(H_2dcbpy)(CN)_4]^{-}$, and $[Fe(CN)_6]^{3-}$, of these possible contaminates the first one is actually of interest in future studies. The feasibility of displacing more than one H_2dcbpy ligand is small, due to the fact that it requires hours in a steam bath to convert the bis(cyano)bis(2,2'-bipyridine)iron(II) to tetrakis(cyano)(2,2'-bipyridine)iron(II) percholrate.[11] Despite the less basic nature of the H_2dcbpy ligand extensive heating, not present in the above reactions, should still be required to form the tetrakis species.

While the target complex could not be synthesized, a fundamental understanding of the dynamics of similar complexes, 1-3, is critical in establishing a protocol for studying the injection dynamics of iron(II)-based sensitizers. Dr. Susane Ferrere kindly donated some purified 4 to enable us to gather preliminary results on the injection dynamics of 4 bound to TiO_2.

5.3.2 Steady-state Electronic Absorption

Absorption spectra of complexes 1-3 are shown in Figure 5-1. In the case of these complexes the low energy charge transfer bands are metal to ligand (MLCT) in nature and singlet in character due to the low-spin d^6 configuration of polypyridyl complexes of iron(II). All complexes possess broad visible MLCT bands, which have maxima at 524 nm, 615 nm, and 544 nm corresponding to complexes 1, 2, and 3, respectively.

Comparison of the absorption spectra of complexes 1 and 2 is shown in Figure 5-2. Both spectra show a charge transfer absorption in the visible ~530 nm and ligand based transitions in the ultraviolet region. The spectrum of complex 2 shows that the ^{1}MLCT band was shifted slightly to the red from complex 1. Due to the ability of para $-CO_2H$ groups on the bipyridine ligand to remove electron density from the nitrogen the dcbpy ligand is more easily reduced thus shifting ^{1}MLCT band to lower energy when compared
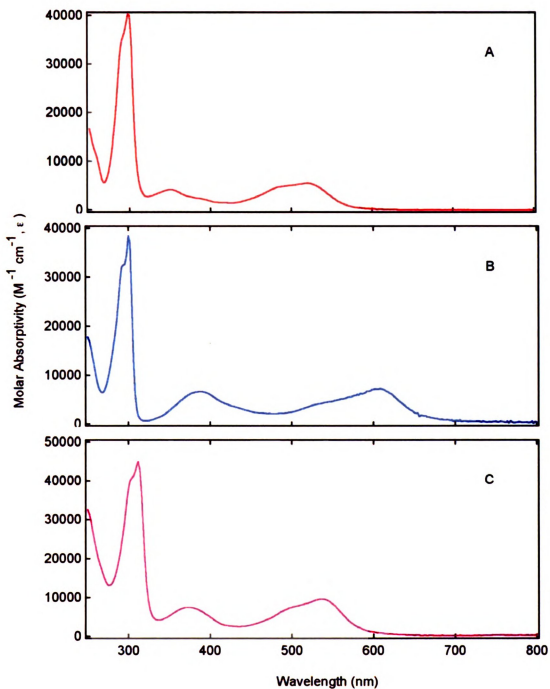
Figure 5-1. Molar absorptivities of $[Fe(bpy)_3]^{2+}$, $[Fe(dcbpy)_3]^{4-}$ and $Fe(bpy)_2(CN)_2$
A) $[Fe(bpy)_3]^{2+}$ in acetonitrile; B) $[Fe(dcbpy)_3]^{4-}$ in methanol; C) $Fe(bpy)_2(CN)_2$ in acetonitrile.
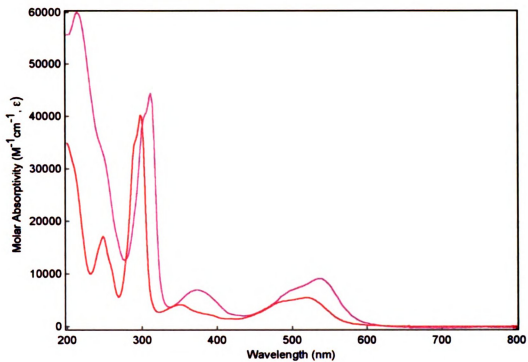
Figure 5-2. Molar absorptivities of $[Fe(bpy)_3]^{2+}$ and $[Fe(dcbpy)_3]^{4-}$. $[Fe(bpy)_3]^{2+}$ in acetonitrile (red, —); $[Fe(dcbpy)_3]^{4-}$ in methanol (magenta, —).
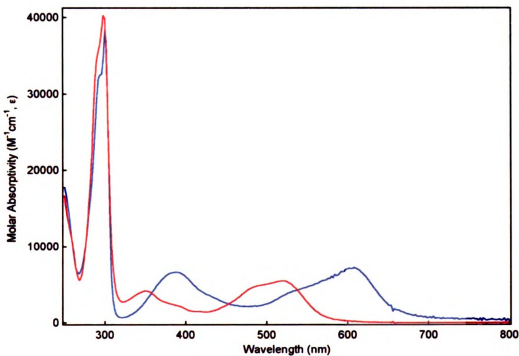

Figure 5-3. Molar absorptivities of $[Fe(bpy)_3]^{2+}$ and $Fe(bpy)_2(CN)_2$ in acetonitrile. $[Fe(bpy)_3]^{2+}$ in acetonitrile (red, —); $Fe(bpy)_2(CN)_2$ in acetonitrile (blue, —).

126

to the unsubstituted bipyridyl complex **1**.

Figure 5-3 shows the absorption spectra of complexes **1** and **3** both in acetonitrile. Both complexes have the characteristic MLCT band in the visible. The shift of the ^{1}MLCT band from complex **1** to complex **3** is characteristic of the shift seen between homoleptic and mixed ligand ruthenium(II) complexes. The red shift is consistent with the change in the symmetry from D_3 to C_{2v} decreasing the energy needed to reach the π^* orbitals of the ligand.

Combining the red shift of the MLCT band when bipyridine was substituted with the more easily reduced H_2dcbpy ligand and the impact of changing the symmetry of the molecule from D_3 to C_{2v}: the MLCT band in complex **4** should readily extend into the visible-red region of the spectrum. In terms of a sensitizer for TiO_2 based solar cells, shifting the absorption features of the sensitizer to the red is beneficial. In this regard, the report of photocurrent generation with **4** bound to TiO_2, from Gregg and Ferrere, was not surprising; however, the small amplitude of the current is curious.[4]

Ferrere and Gregg also report incident-photon-to-current efficiencies (IPCE) to be higher when the photons energy corresponds to the higher energy charge transfer band.[4] Ideally the IPCE curve should match the absorption spectrum of the sensitizer. In the case of **4** bound to TiO_2 the IPCE curve traces the first CT band and drops significantly when the photon wavelength is tuned to the lower energy MLCT band. The origin of this discrepancy is the main interest of this vein of research. Is the deviation of the IPCE curve from the absorption spectrum due to the inability of the lower energy MLCT band to inject? Or is it a manifestation of the ultrafast lifetimes of charge transfer states in iron(II) polypyridyl complexes which has been recently discussed by McCusker and coworkers?[7]

5.3.3 Time-resolved Transient Absorption Spectroscopy

Establishing a strong fundamental understanding of the intrinsic excited state dynamics of these iron(II) sensitizer was imperative. To do that we would like to establish a protocol to systematically examine the excited state dynamics of proposed TiO_2 sensitizers.

This approach entails complete characterization of solution phase dynamics followed by determination of any perturbations of the observed solution phase dynamics upon binding the sensitizer to an injection inert substrate such as ZrO_2 or Al_2O_3. Once the intrinsic dynamics of the sensitizers have been identified subsequent information obtained with the sensitizer bound to TiO_2 would be able to be more accurately interpreted to yield information on the injection dynamics of the sensitizer. Solution phase results for complexes 2 and 3 are presented below along with preliminary work with complexes 3 and 4 bound to TiO_2.

5.3.4 Solution Phase Dynamics of $Na_4[Fe(dcbpy)_3]$ in Water

Synthesis and subsequent time-resolved characterization of complex 2 provides an important link in the comparison of iron(II) based sensitizers to ruthenium(II) based. The sensitizer used by Grätzel and coworkers when they initially reported the successful generation of a photocurrent with sensitized TiO_2 was a tris(H_2dcbpy)ruthenium(II) complex.[1, 16] Complex 2 provides us with a direct comparison of an iron(II) sensitizer that should emulate the ruthenium sensitizer in binding to the TiO_2 enabling us to exclude variations in the binding mode of the sensitizer to TiO_2. The binding mode of the sensitizer has been shown to impact the overall efficiency of the cell[17]; however, it has yet to be determined if there is a direct impact on the injection process.[18]

Due to solubility issues with tris(dcbpy) type complexes the measurement of complex 2 was done in distilled water. Excitation of complex 2 at 540 nm with an optical density of the sample being ~0.8 at the excitation wavelength yielded the following results.

Table 5-1. Lifetimes of $[Fe(bpy)_3]^{2+}$, $[Fe(dcbpy)_3]^{4-}$ and $Fe(bpy)_2(CN)_2$.

	$[Fe(bpy)_3](PF_6)_2$	$Na_4[Fe(dcbpy)_3]$	$Fe(bpy)_2(CN)_2$
τ_1	70 ± 30 fs	70 ± 30 fs	70 ± 30 fs
τ_2	200 ± 10 fs	200 ± 10 fs	100 ± 10 fs
τ_{gs}	800 ps [a]	550 ± 50 ps [b]	530 ± 50 ps [b]

[a] Reported from reference

[b] May differ significantly from other reports due to temporal limitation of the spectroscopic system.

As expected for an iron(II) polypyridyl complex the ground state recovery time was on the order of hundreds of picoseconds as reported in Table 5-1. Ground state recovery is indicated by the uniform amplitude decay shown in Figure 5-4. This long-lived state that exhibits ground state recovery is ligand field in nature and most likely the $^5T_2$ state, as reported by McCusker and coworkers for a series of iron(II) polypyridyl complexes[7].
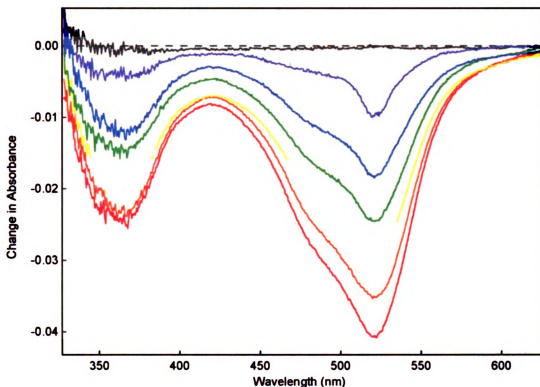
Figure 5-4. Ground state recovery of $[Fe(dcbpy)_3]^{4-}$ in water.
The ground state recovery of $[Fe(dcbpy)_3]^{4-}$ in water after 540 nm excitation is shown with delays of 1 ps(—), 90 ps(—), 200 ps( ), 500 ps(—), 800 ps(—) and 1 ns (—).

Due to the metal centered nature of the ligand field long-lived excited state of complex **4** it is not expected for injection to occur from the long-lived excited state of this complex. It is essential that the electron is present on the ligand to inject and electron into the conduction band of TiO_2, therefore probing the dynamics associated with the initially populated charge transfer state is essential. Figure 5-5 shows the excited state decay of the initially populated ^1MLCT state to the long-lived $^5T_2$ ligand field state. The rapid deactivation

129
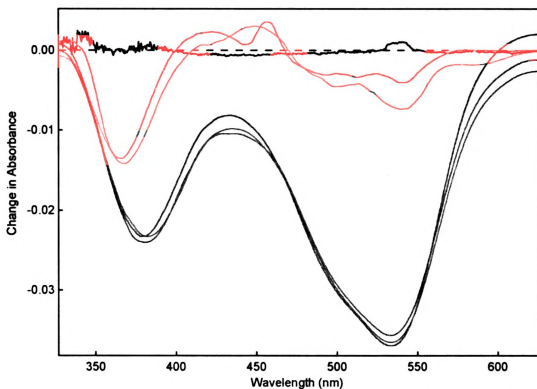
Figure 5-5. Chirp-corrected early time transient absorption spectra of $[Fe(dcbpy)_3]^{4-}$ in water. Early time dynamics of $[Fe(dcbpy)_3]^{4-}$ in water after 540 nm excitation are shown with delays of 0 ps(—), 0.1 ps( ), 0.2 ps( ), 0.3 ps(—), 0.5 ps(—) and 1 ps (—).

of this ^{1}MLCT state is typical of iron(II) polypyridyl complexes.[7] Single wavelength kinetic traces better illustrate the ultrafast deactivation of the initially formed state to the long-lived state and data collected at 420 and 650 nm probe are shown in Figure 5-6. These kinetic data show the characteristic spectroscopic handle of the ^{1}MLCT deactivation, in that a positive signal decays to a long-lived negative signal, which has been reported previously.[6, 7] Deconvolution of the kinetic trace at 420 nm gives a lifetime of the ^{1}MLCT state of 70 ± 30 fs, which is also reported in Table 5-1. Solvent responses at $\Delta t=0$ prohibits deconvolution fitting of the 650 nm trace; however, the signature positive amplitude of the ^{1}MLCT state is observed indicating that the ^{1}MLCT state is formed. Excitation in to the charge transfer band at ~400 nm would enable collection of kinetic traces at 650 nm with a small amount of solvent interference; however this would entail excitation into a charge transfer band that; 1) is not readily modeled by spectroelectrochemical measurements, 2)
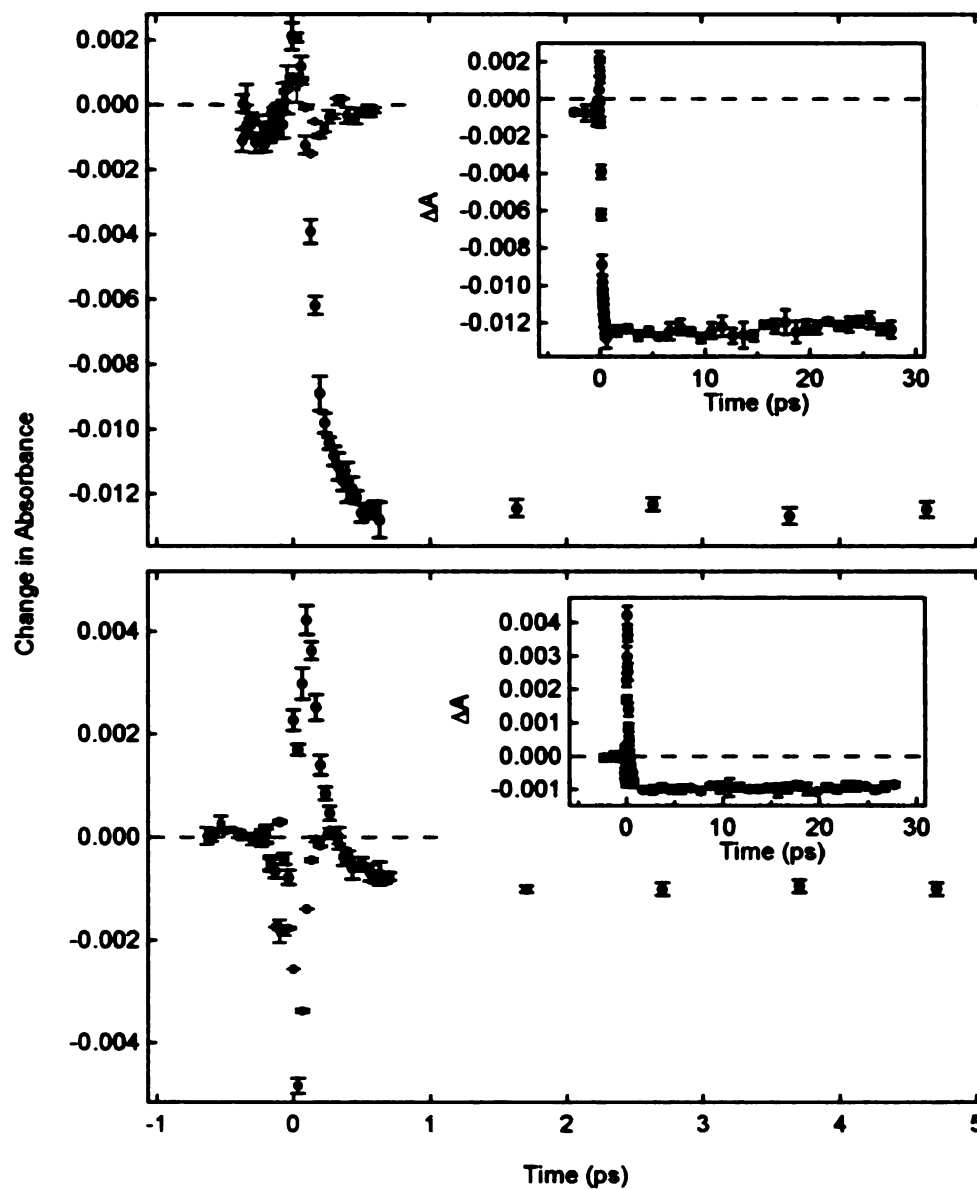
Figure 5-6. Single wavelength kinetic traces of $[Fe(dcbpy)_3]^{4-}$ in water.
Single wavelength traces after excitation at 540 nm Top: 420 nm probe Bottom: 650 nm probe. Solvent traces are shown in red for each probe wavelength.

has intraligand transitions close in energy, thus preventing clean excitation into a MLCT transition, and 3) when probing the complex bound to TiO_2 would increase the probability of directly exciting the band gap of TiO_2.

5.3.5 Solution Phase Dynamics of $Fe(bpy)_2(CN)_2$ in Acetonitrile

In 1993, Grätzel and coworkers published the successful synthesis of a ruthenium(II)

mixed ligand complex that became the standard for dye sensitized solar cells, N3 or bis(2,2'-bipyridine-4,4'-dicarboxylate)bis(thiocyanato)ruthenium(II).[19] Working from the foundation of Grätzel's research Ferrere and Gregg incorporated an iron(II) analogue into a dye sensitized solar cell and were the first to report photo current generation with an iron(II) sensitizer.[4] Since the synthesis of complex **4**, the sensitizer used in the 1998 report by Ferrere and Gregg, proved to be more difficult than expected complex **3** was used to begin characterization of iron(II) mixed ligand complexes.

Ground state recovery dynamics of complex **3** in acetonitrile are shown in Figure 5-7. Again uniform decay of the amplitude of the entire spectrum was indicative of ground state recovery. Table 5-1 contains the lifetime of the long-lived excited state obtained from fitting a kinetic trace that exceeded the temporal window of the above instrumentation. Similar to complex **2** the long-lived excited state of complex **3** is ligand field in nature. The
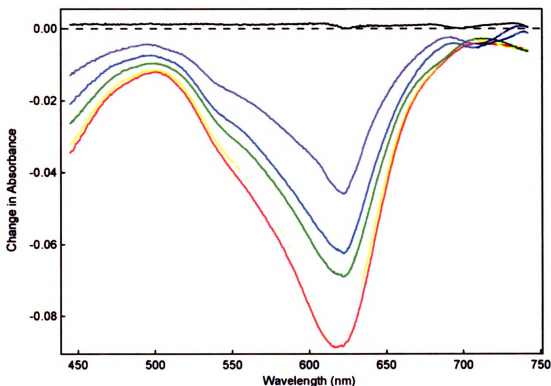
Figure 5-7. Ground state recovery of Fe(bpy)$_2$(CN)$_2$ in acetonitrile.
The ground state recovery of Fe(bpy)$_2$(CN)$_2$ in acetonitriel after 600 nm excitation is shown with delays of 1 ps(—), 90 ps(—), 200 ps(   ), 500 ps(—), 800 ps(—) and 1 ns (—).

exact assignment of the state is difficult to determine due to the difference in symmetry of complex **3** from complex **1** or **2**. A triplety degenerate state such at the $^5T_2$ state is not supported in C_{2v} symmetry and so the state must split. At this point employing the Tanaube-Sugano diagram to identify the long-lived state was not practical. Subsequent identification of which state is lower in energy upon decomposing to lower symmetry is decidedly difficult. Therefore, further characterization the long-lived state beyond being ligand-field in nature was left to other experiments and calculations.

Despite the ambiguity of the long-lived excited state the initially excited state was still ^{1}MLCT in nature and could thus be studied in a similar manner as complex **2**. Time-resolved full spectral analysis of the first picosecond after excitation is presented in Figure 5-8. The jagged features present in the $\Delta t=0$ ps spectrum are due to the chirp correction process, which was discussed in detail in reference 15. Figure 5-9 shows the rapid
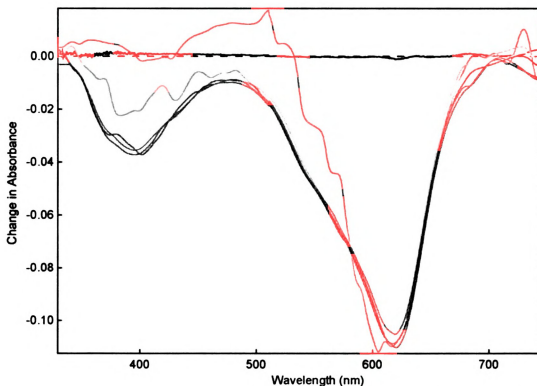
Figure 5-8 Chirp-corrected early-time transient absorption spectra of Fe(bpy)$_2$(CN)$_2$ in acetonitrile. Early-time dynamics of Fe(bpy)$_2$(CN)$_2$ in acetonitrile after 600 nm excitation are shown with delays of 0 ps(—), 0.1 ps (—), 0.2 ps(   ), 0.3 ps(—), 0.5 ps(—) and 1 ps (—).
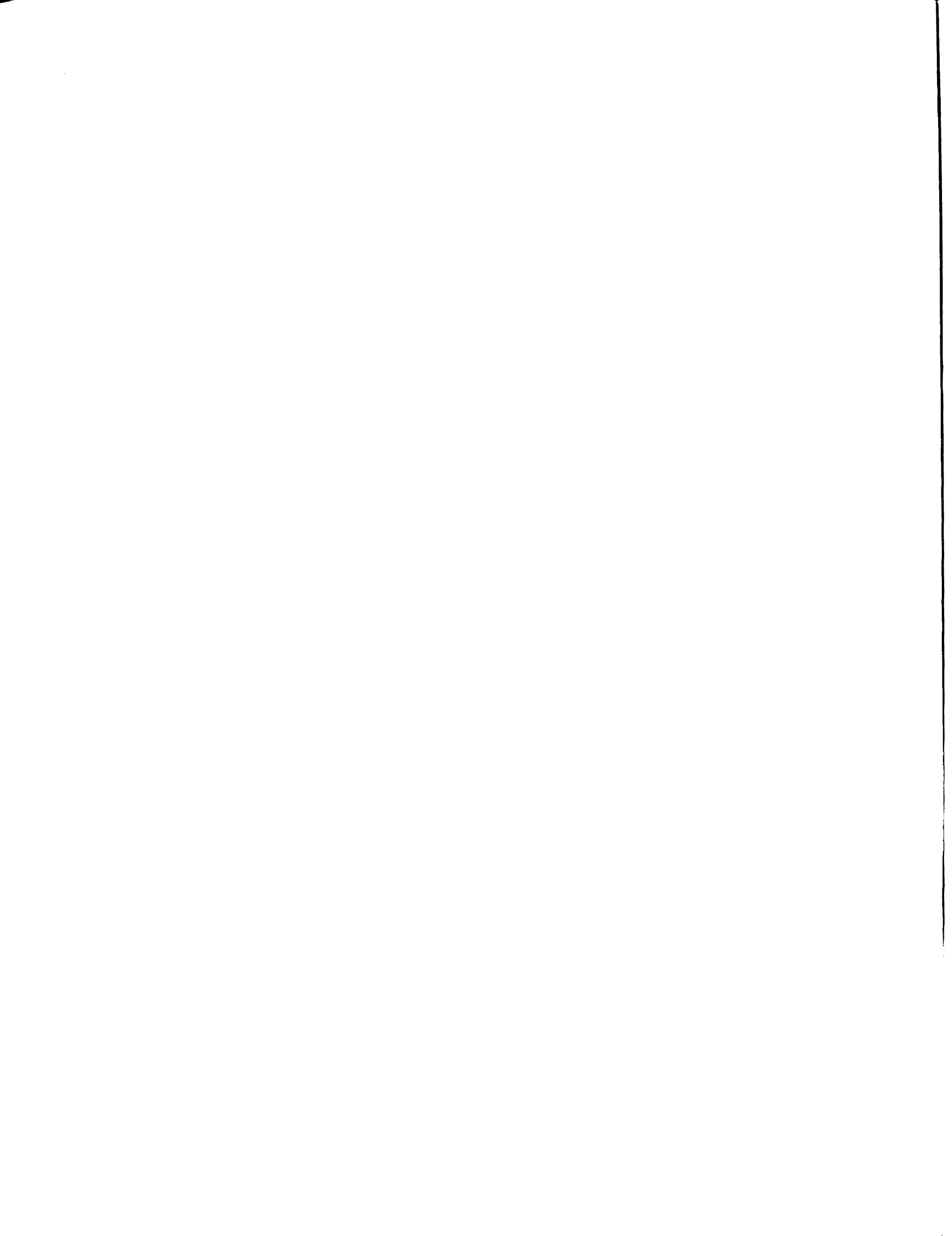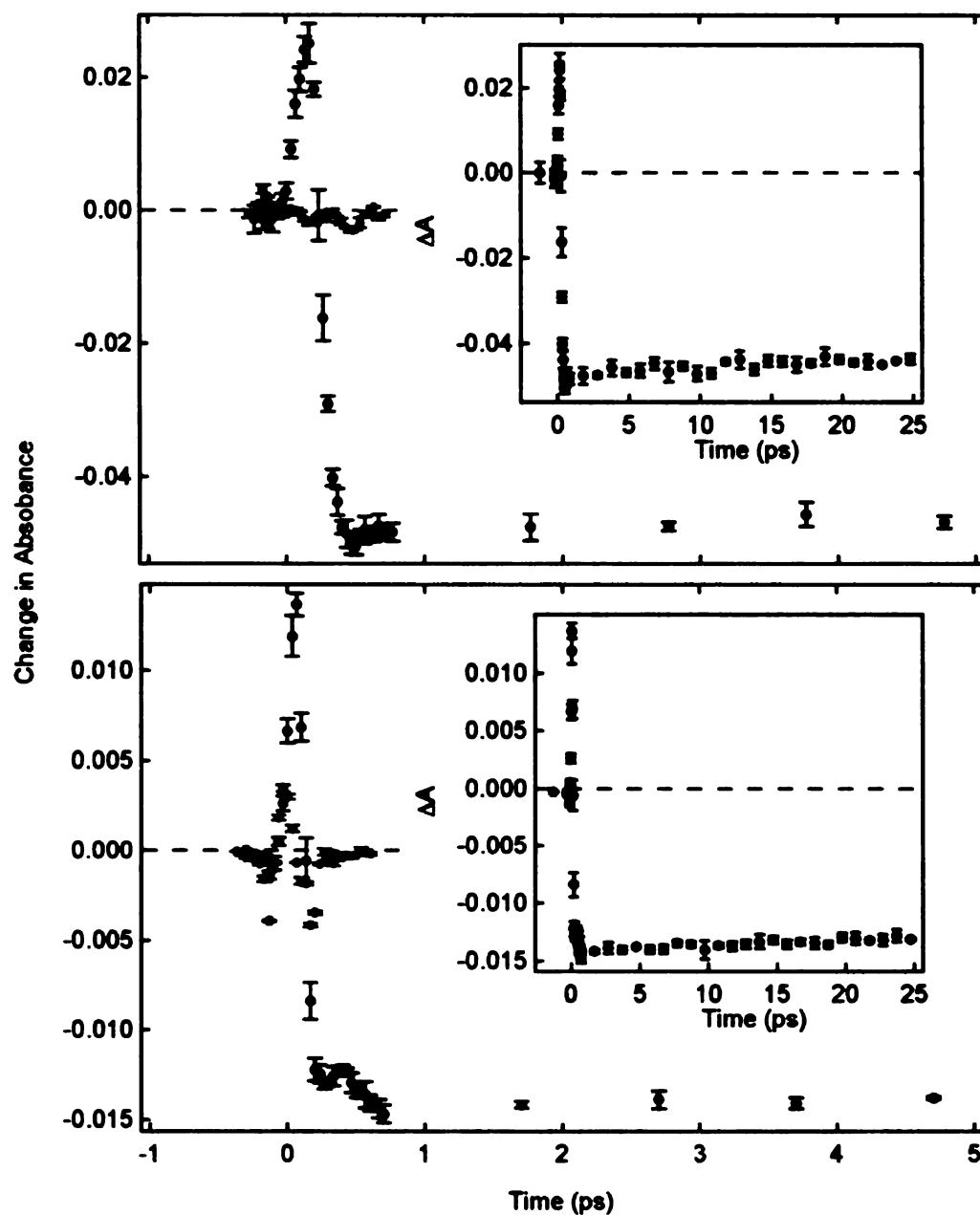
Figure 5-9. Single wavelength kinetic traces of $Fe(bpy)_2(CN)_2$ in acetonitrile.
Single wavelength traces after excitation at 600 nm Top: 350 nm probe Bottom: 460 nm probe. Solvent traces are shown in red for each probe wavelength.

deactivation of the ^{1}MLCT state of complex **3**, single wavelength kinetic data at 350 nm and 460 nm probe showed the characteristic spectroscopic handle of the ^{1}MLCT deactivation mentioned above. Fitting these kinetic traces with the deconvolution software yields a ^{1}MLCT lifetime of 70 ± 30 fs. The fact that the mixed ligand complex $Fe(dcbpy)_2(CN)_2$ has an ultrafast ^{1}MLCT lifetime indicates that deactivation from charge transfer state may be directly competing with electron injection when the analogue, complex **4** is bound to

TiO_2. An upper limit on the rate of electron transfer for ruthenium(II) based sensitizer has been determined from measurements of the electron in the conduction band and the report of the lifetime of the ^{1}MLCT state of $[Ru(bpy)_3]^{2+}$ as approximately 50 fs.[20] If this injection rate was independent of the sensitizer, then the deactivation of the lone MLCT state of the iron(II) based sensitizers would be directly competing with electron injection.

5.3.6 Preliminary Results on the Dynamics of $Na_4[Fe(dcbpy)_3]$ Bound to TiO_2

Attempting to bind complex 2 to TiO_2 from a water solution did not produce a film. Binding the sensitizer from a methanol solution did produce a film; however, the optical density of the film at the absorption maximum of the sensitizer was only 0.3. Optimal conditions for adsorption of the iron(II) sensitizers are still being developed. Several groups have reported on other iron(II) sensitziers and their steady state/photoelectrochemical properties.[12, 21, 22]

From previously reported spectroelectrochemical measurements on complex 1 we expected the oxidized species, being $[Fe(dcbpy)_3]^{3-}$, to absorb red of 600 nm.[7] Therefore, if electron injection did occur we would be able to monitor the formation of the oxidation product $[Fe^{3+}(dcbpy)_3]/TiO_2$ from 600-800 nm and the electron in the conduction band red of 700 nm.

Despite the small absorption cross-section an attempt was made to collect ultrafast transient absorption data with complex 3 bound to TiO_2. A sandwich cell configuration was used with a 0.5 M LiI acetonitrile solution as the supporting electrolyte in order to increase the driving force for electron injection into TiO_2.[23] Chapter 2 provides further discussion as to the importance of the presence of small cations on the process of electron injection into TiO_2. Figure 5-10 shows single wavelength kinetic traces of 3 bound to TiO_2 at 690 and 750 nm probe. Both traces show a slight positive y-offsets, this positive off set indicates that there was a species present that was absorbing more than the ground state at the given probe wavelength. Since solution phase data of complex 3 showed a slight negative feature at 690 nm the trace shown in Figure 5-10 was most likely indicative of the persistence
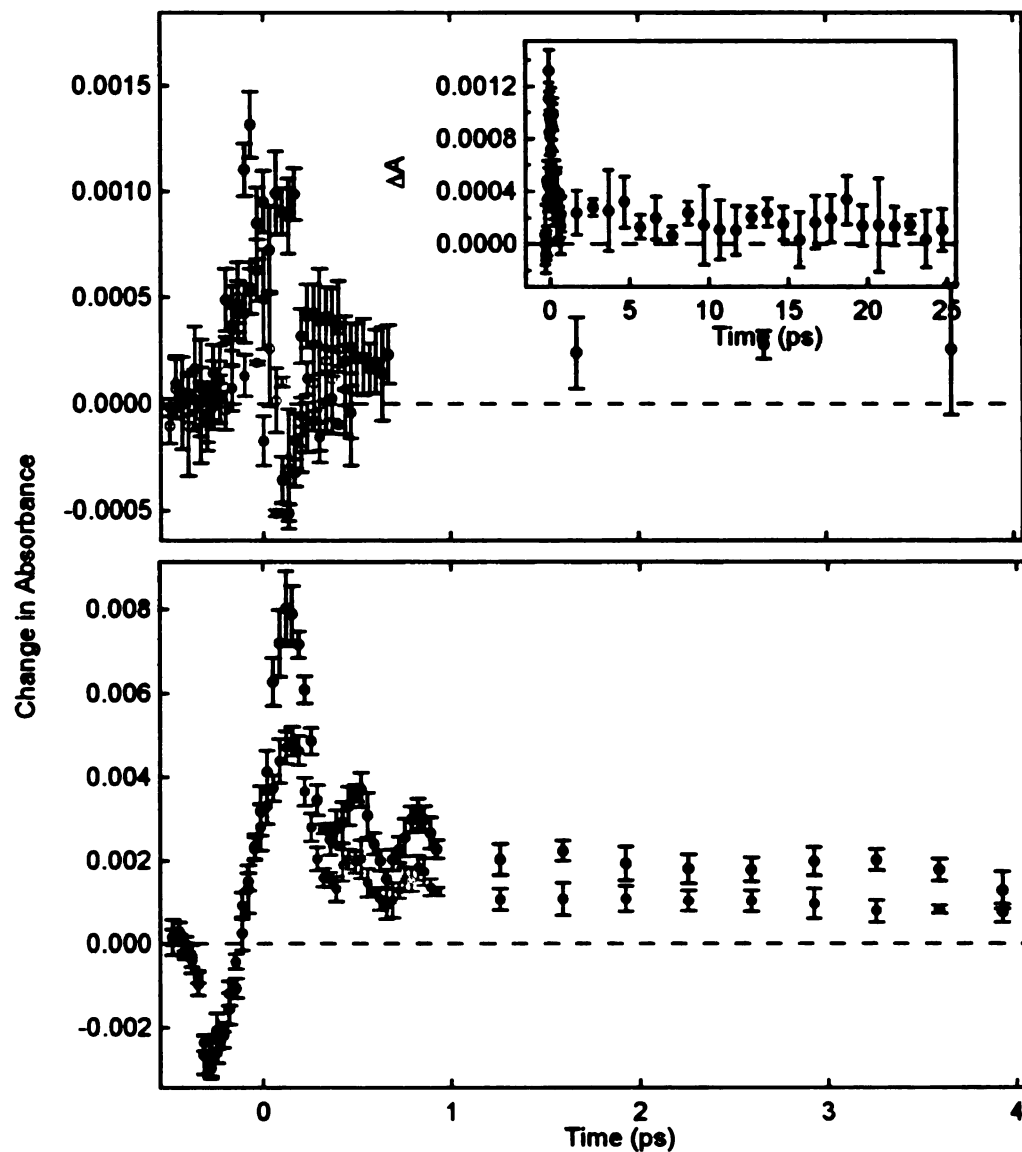
Figure 5-10. Single wavelength kinetic traces of [Fe(dcbpy)$_3$] bound to TiO$_2$.
Single wavelength traces after excitation at 540 nm Top: 690 nm probe. Bottom: 750 nm probe. Background traces of blank TiO$_2$ in the presence of the electrolyte are shown in red for each probe wavelength.

of the oxidized sensitizer on this time scale. At 750 nm probe, both the oxidized feature

and the electron in the conduction band would manifest at a positive off set, so this trace

was more ambiguous. Early time dynamics that resembled the decay of the excited state.

The strong signal associated with the excited state adds a layer of complication to these

measurements. To be able to assign a time constant to the injection process establishing a

clean probe wavelength was necessary, to provide a means to monitor one species at a time.

Lian and coworkers have shown that probing at 2000 cm⁻¹ is an ideal place to monitor the electron in the conduction band of TiO_2 because the broad absorption features of the oxidized sensitizer do not extend as far into the infrared as the absorptions of the electron in the conduction band.[24]

5.3.7 Preliminary Results on the Dynamics of $Fe(H_2dcbpy)_2(CN)_2$ Bound to TiO_2

In 2001, Lian and coworkers published a single kinetic trace obtained at 2000 cm⁻¹ of complex **4** bound to TiO_2.[24] The excitation wavelength chosen in the 2001 experiment was 400 nm, at this excitation wavelength it is possible that electrons are being directly excited into the conduction band of TiO_2. The argument for using such a high-energy excitation wavelength was that the blue MLCT state of the iron complex yields a much larger IPCE value than the lower energy MLCT band as seen in the 1998 report by Ferrere and Gregg.[12, 24]

Due to synthetic complications associated with isolating analytically pure complex **4** complete characterization has not been done. Preliminary results of **4** bound to TiO_2 are shown in Figure 5-11. There seems to be little difference between the early time dynamics of a methanol solution of **4**, **4** bound to ZrO_2 and **4** bound to TiO_2 at 480 nm probe. The long time data seems to be more revealing. The normalization of the data at $\Delta t=0$ shows an offset between the methanol solution and both the TiO_2 and ZrO_2 sensitized films. While additional data was needed this offset was most likely due the formation of oxidized sensitizer.

5.4 Conclusions

The lifetime of the initially excited ¹MLCT state of the iron(II) polypyridyl complexes of interest in this study were ultrafast, consistent with previous reports on a series of iron(II) polypyridyl complexes.[7] Considering the requirements for electron injection from a sensitizer into the conduction band of TiO_2 the only state that possess the ideal electronic coupling and energetics for electron injection[3] in an iron(II) based sensitizer
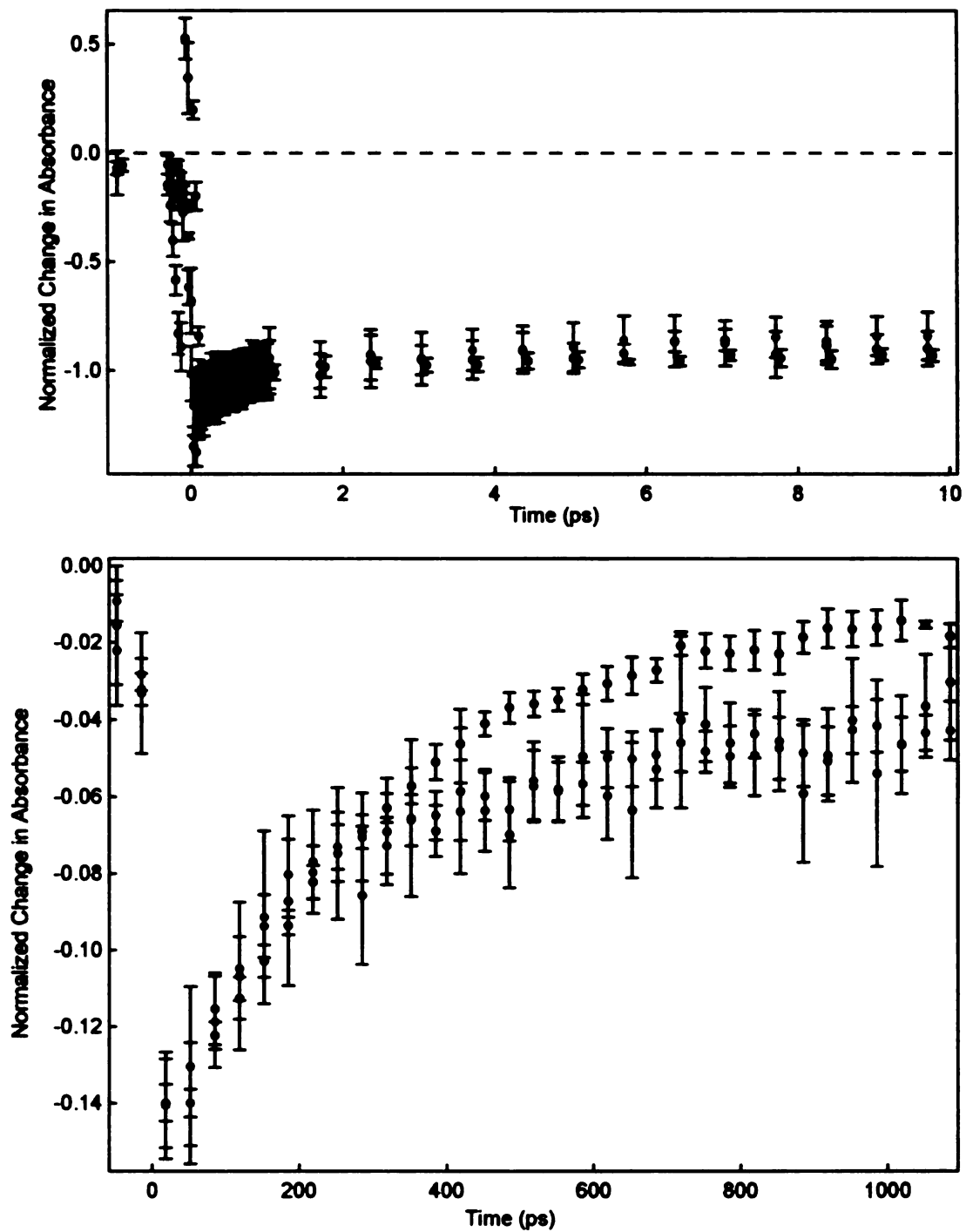
Figure 5-11. Single wavelength kinetic traces of $Fe(dcbpy)_2(CN)_2$ at 480 nm probe after 590 nm excitation.

The single wavelength traces at 480 nm probe show Top: early-time dynamics normalized at 1 ps and Bottom: long time delays of $Fe(dcbpy)_2(CN)_2$ in methanol (black, •), bound to TiO_2 (blue, •), and bound to ZrO_2 (red, •).

was the initially formed ^{1}MLCT state. Given the lower limit as to how rapidly electron injection occurs, for TiO$_2$ based solar cells, is approximately 50 fs[20,25] it was reasonable to conclude that the deactivation of the ^{1}MLCT state is in direct competition with the injection process in the case of iron(II) polypyridyl sensitizers.

Additional studies with infrared probe wavelengths are key in determining the timescale for injection with iron(II) based sensitizers. Studies that tune the excitation energies across the absorption spectrum of the sensitizer will also prove useful in establishing a correlation between the IPCE results and injection processes. Currently, research is underway to achieve these goals and will be reported later.

For iron(II) based sensitizers to become viable alternatives to ruthenium(II) sensitizers the lifetime of the ^{1}MLCT state needs to increase. Fortunately, coordination compounds such as iron(II) polypyridyl complexes are ideal candidates for a molecular engineering approach to systematic manipulation of the electronic and physical structure of a complex to determine the best way to increase the lifetime of the ^{1}MLCT state.

5.5 References

1. Desilvestro, J.; Grätzel, M.; Kavan, L.; Moser, J.; Augustynski, J. *J. Am. Chem. Soc.* **1985**, *107*, 2988-2990.

2. Grätzel, M. *Inorg. Chem.* **2005**, *44*, 6841-6851.

3. Kalyanasundaram, K.; Grätzel, M. *Coord. Chem. Rev.* **1998**, *77*, 347-414.

4. Gregg, B.; Ferrere, S. *J. Am. Chem. Soc.* **1998**.

5. Creutz, C.; Chou, M.; Netzel, T. L.; Okumura, M.; Sutin, N. *J. Am. Chem. Soc.* **1980**, *102*, 1309-19.

6. Monat, J. E.; McCusker, J. K. *J. Am. Chem. Soc.* **2000**.

7. Smeigh, A. L.; Brown, A. M.; McCusker, J. K. *J. Phys. Chem.* **2007**, *Submitted for publication.*

8. Chang, H.-R.; McCusker, J. K.; Toftlund, H.; Wilson, S. R.; Trautwein, A. X.; Winkler, H.; Hendrickson, D. N. *J. Am. Chem. Soc.* **1990**, *112*, 6814-6827.

9. Sprintschnik, G.; Sprintschnik, H. W.; Kirsch, P. P.; Whitten, D. G. *J. Am. Chem. Soc.* **1977**, *99*, 4947-4954.

10. Cooper, G. H.; Rickard, R. L. *Synthesis* **1971**, 31.

11. Schilt, A. A. *J. Am. Chem. Soc.* **1960**, *82*, 3000-3005.

12. Ferrere, S. *Inorg. Chimi. Acta* **2002**, *329*, 79-92.

13. Katz, J. E.; Lewis, N. S. *PhD Dissertation California Institue of Technology* **2007**.

14. Juban, E. A.; McCusker, J. K. *J. Am. Chem. Soc.* **2005**, *127*, 6857-6865.

15. Juban, E. A. *Doctoral Thesis* **2006**, *University of Califonia, Berkeley,* 31.

16. Vlachopoulos, N.; Liska, P.; Augustynski, J.; Grätzel, M. *J. Am. Chem. Soc.* **1988**, *110*, 1216-1220.

17. Kilsä, K.; Mayo, E. I.; Brunschwig, B. S.; Gray, H. B.; Lewis, N. S.; Winkler, J. R. *J. Phys. Chem. B* **2004**, *108*, 15640-15651.

18. Smeigh, A. L. *On going research* **2007**.

19. Nazeeruddin, M. K.; Kay, A.; Rodicio, I.; Humphry-Baker, R.; Müller, E.; Liska, P.; Vlachopoulos, N.; Grätzel, M. *J. Am. Chem. Soc.* **1993**, *115*, 6382-6390.

20. Bhasikuttan, A. C.; Suzuki, M.; Nakashima, S.; Okada, T. *J. Am. Chem. Soc.* **2002**, *124*, 8398-8405.

21. Yang, M.; Thompson, D. W.; Meyer, G. J. *Inorg. Chem.* **2000**, *39*, 3738-3739.

22. Yang, M.; Thompson, D. W.; Meyer, G. J. *Inorg. Chem.* **2002**, *41*, 1254-1262.

23. Redmond, G.; Fitzmaurice, D. *J. Phys. Chem.* **1993**, *97*, 1426-1430.

24. Asbury, J. B.; Wang, Y.-Q.; Hao, E.; Ghosh, H. N.; Lian, T. *Res. Chem. Int.* **2001**, *27*, 393-406.

25. Hannappel, T.; Burfeindt, B.; Storck, W.; Willig, F. *J. Phys. Chem. B* **1997**, *101*, 6799-6802.

Chapter 6. Concluding Comments and Future Directions.

6.1 Concluding comments

All the research presented in this dissertation has been driven by the desire to understand the fundamental dynamics associated with Group 8 transition metal based complexes and how those dynamics could impact the performance of TiO_2-based solar cells that might be sensitized with one of the studied transition metal complex. The majority of the information present deals with iron(II) polypyridyl complexes and their solution phase dynamics because it is imperative to understand the intrinsic dynamics of a complex before introducing complicating factors such as electron injection.

A small section of this work probed the impact the composition of the electrolyte had on the injection dynamics of a well characterized sensitizer, N3. The results indicate that injection from N3 can be significantly quenched in the presence of TBAI based electrolyte compared to the standard electrolyte consisting of LiI. We believe it is a combination of a less positive conduction band potential due to the TBA^+ and a deleterious interaction of the I^- with the excited state of the N3. When electrolytes composed of $TBAClO_4$ and $LiClO_4$ were used in place of the TBAI and LiI electrolytes there was no significant difference between the TBA^+ and Li^+ electrolytes, which indicates that I^- plays a significant role in the reduction of the injection dynamics. Comparing all four electrolyte solutions allowed us to observe the drastic differences between $-I^-$ based electrolytes and $-ClO_4^-$-based electrolytes, where we determined that it is essential to use electrolytes that contain the redox active species, $-I^-$, to best model the dynamics occurring in the complete cell. These finding calls into question a significant portion of the injection dynamics reported in the absence of a redox active species. While the main goal of this section was to identify if the injection was quenched in the presence of TBA^+ we gained so much more from the experiment. We now know that to best model the injection dynamics that occur in the complete cell we must incorporate electrolytes that have the redox active I^- species and to increase the

amount of injection ensuring that the electrolyte has a high concentration of small cations such as Li^+ or H^-.

From the above work we have identified some optimal parameters for monitoring injection dynamics on a functional cell; however, with that data we have not made an advance in increasing the overall efficiency of TiO_2-based solar cells. In terms of the injection efficiencies the ruthenium(II)-based sensitizers can not be matched; however, the overall efficiency of these TiO_2 based cells is not a simple reflection of the sensitizers injection efficiency but a complicated mix of injection, recombination, regeneration, and collection efficiency. In the case of ruthenium(II)-based sensitizers the overall efficiency is a balance between the rate of recombination of the injected electron with the sensitizers and the rate of regeneration of the oxidized sensitizer. To increase the overall efficiency of these TiO_2-based cells it would be beneficial to move away from the optically dense and possibly quenching I^-/I_3^- redox couple; however, slight perturbations to the reduction potential of the redox couple causes significant decreases in the overall efficiency of the cell. Due to the delicate balance between the rates of recombination and regeneration changing the redox couple to increase the output power, shifting it more positive, decreases the rate of regeneration and thus allows for possible short-circuiting of the cell. Our thought on circumventing this problem is to move from ruthenium(II)-based sensitizers to iron(II)-based sensitizers. This would take advantage of the fact that first row transition metals have intrinsically fast reaction rates than second row transition metals, in hopes that a redox couple with a more positive potential could be substituted for the I^-/I_3^- redox couple yet the regeneration rate would not change significantly.

Initial reports of iron(II) sensitized TiO_2 report small photocurrent yields; which little to no characterization of the injection process itself. Without this vital piece of information optimization of the iron(II) sensitized cells is near impossible. The goal of the majority of the work presented here involves characterizing the intrinsic dynamics associated with iron(II) complexes in an attempt to better understand the injection dynamics of iron(II)-

based sensitizers. Initial characterization of the intrinsic dynamics of iron(II) polypyridyl complexes began with a low-spin model complex, meaning all of the d-electrons reside in the t_{2g} orbitals. This model complex is unique in that slight modifications of the ligand set enable the synthesis of an analogous high-spin complex where both the e_g and t_{2g} orbitals are populated. The high-spin analogue possesses a ground state configuration that is identical to that of the long-lived excited state of the low-spin complex, this similarity enable us to use the high-spin analogue as a model for the long-lived excited state of the low-spin complex. Through this unique relationship we were able to calculate the difference spectrum of the low-spin complex and identify spectroscopic signatures that are associated with the long-lived $^5T_2$ state. Similarly, we were able to use spectroeletrochemical data to identify spectroscopic handles for the lowest energy metal-to-ligand charge transfer (MLCT) state. With these two spectroscopic tags were able to identify the MLCT to ligand field (LF) conversion and extract a time constant associated with the deactivation of the MLCT excited state. It was found that the MLCT lifetime is approximately 70 ± 30 fs and vibrational cooling on the $^5T_2$ surface is complete in less than 50 ps. The ultrafast nature of the excited state evolution is present across the entire spectrum, indicating that no matter where the complex is excited or probed the MLCT state rapidly deactivates to the $^5T_2$ state.

In terms of iron(II)-based sensitizers, assignment of the MLCT lifetime to less than 100 fs implies that the MLCT excited state of this iron(II) complex is not populated long enough to inject an electron. If this ultra short lived MLCT excited state is characteristic of low-spin iron(II) complexes, then the low photocurrent densities observed for iron(II) sensitized TiO_2 might be due to the low injection yield of the sensitizer. Additional measurement were done on a series of iron(II) polypyridyl complexes to determine if the MLCT excited state of iron(II) polypyridyl complexes is inherently short lived. The findings indicate that the lifetime of the MLCT excited state of a series of iron(II) complexes is on the order of 100 fs. Knowing this we can begin to explain the small photocurrents observed

with iron(II)-based sensitizers.

Since efficient electron injection occurs with the excited state localizing the electron on the ligand, the injecting state needs to be MLCT in nature. In the case of iron(II)-based sensitizers this MLCT excited state is deactivated by intramolecular relaxation pathways in less than 100 fs, which competes directly with the injection of the electron. Once the iron(II)-based sensitizer is in the long-lived excited state the electron density is localized on the metal center, further prohibiting any electron injection. Despite the short lived MLCT state a photocurrent is observed with iron(II)-based sensitizers, indicating that some considerable amount of injection is occurring from this state. This is promising in two respects: 1) since injection is occurring with such a short lived MLCT state any successful engineering of the sensitizer to extend the MLCT lifetime will only improve the injection yield and 2) if this injection yield can be increase then it is reasonable to start testing different redox couples to determine if we can gain output power by taking advantage of the faster reaction rates of first row transition metal complexes.

6.2 Future directions

As indicated in Chapter 5 the majority of work needs to focus on probing for injection events in the infrared region of the spectrum. In this region we should be able to successfully monitor the population of the conduction band without complicating signals due to the excited state of the sensitizer. The complexes to start with are $[Fe(dcbpy)_3]^{4+}$ and $Fe(dcbpy)_2(CN)_2$, both in solution and bound to TiO_2 and ZrO_2 (or Al_2O_3). Full characterization of these complexes both in solution and bound to a material will provide a significant amount of information on the timescale of injection with iron(II)-based sensitizers. It will be imperative to monitor the injection dynamics in the presence of electrolyte, to bias the probability for injection.

Additionally, maintaining the collaborative efforts with the Schoenlein, Mathies and Miller groups will be beneficial. The developments in ultrafast X-ray pulses, Raman, and electron pulses are moving us closer to achieving a structural picture of the MLCT to

145

LF conversion. Once we understand what mode are coupled to this ultrafast conversion process we can begin to systematically engineer ligand sets that might extend the lifetime of the MLCT excited state by inhibiting the structural mode associated with the deactivation pathway. This would allow us to increase the lifetime of the MLCT excited state of iron(II)-based sensitizers and possibly open the door to other first row transition metal sensitizers. As mentioned above if we can begin to incorporate first row transition metal based sensitizers into TiO_2 based solar cells then we might be able to start employing redox couples that possess more positive reduction potential thus increasing the photovoltage obtain with these cells.

The decrease in cost associated with moving from second row sensitizers like ruthenium to first row sensitizers like iron is significant. Just think of making a solar cell out of paint chips and rust, what a novel idea.